U. S. DEPARTMENT OF COMMERCE
Charles Sawyer, Secretary
NATIONAL BUREAU OF STANDARDS
E. U. Condon, Director

FEBRUARY 1950
VOLUME • 44
NUMBER 2

JOURNAL OF RESEARCH

of the

NATIONAL BUREAU OF STANDARDS

Contents

RP		Page
2062	Influence of the ground on the calibration and use of VHF field-intensity meters. Frank M. Greene. (Price 5 cents)	123
2063	Determination of curvature by an osculometer. Harvey L. Curtis. (Price 5 cents)	131
2064	A multicolumn countercurrent molecular still. Samuel L. Madorsky. (Price 5 cents)	135
2065	Hydrocarbons in the 108° to 116° C fraction of petroleum. Augustus R. Glasgow, Jr., Charles B. Willingham, and Frederick D. Rossini. (Price 10 cents)	141
2066	Concrete as a protective barrier for gamma rays from cobalt-60. Robert J. Kennedy, Harold O. Wyckoff, and William A. Snyder. (Price 5 cents)	157
2067	Pulse packing in magnetic recording wire. Irvin L. Cooter. (Price 10 cents)	163
2068	Note on the stabilization of acetylglycosyl halides and sugar acetates. Horace S. Isbell and Harriet L. Frush. (Price 5 cents)	173
2069	Phase-equilibrium studies of the high-lime portion of the quinary system Na_2O-CaO-Al_2O_3-Fe_2O_3-SiO_2. William R. Eubank. (Price 15 cents)	175
2070	The field generated by an arbitrary current distribution within a waveguide. J. J. Freeman. (Price 5 cents)	193
2071	Back-scatter observations by the Central Radio Propagation Laboratory—August 1947 to March 1948. W. L. Hartsfield, S. M. Ostrow, and R. Silberstein. (Price 10 cents)	199

For sale by the Superintendent of Documents, U. S. Government Printing Office, Washington 25, D. C. • Price 50 cents
$4.50 per year on subscription

UNITED STATES GOVERNMENT PRINTING OFFICE, WASHINGTON : 1950

U. S. Department of Commerce
National Bureau of Standards

Research Paper RP2006
Volume 44, February 1950

Part of the Journal of Research of the National Bureau of Standards

Influence of the Ground on the Calibration and Use of VHF Field-Intensity Meters

By Frank M. Greene

One type of error known to be present in VHF field-intensity meters (30 to 300 Mc) is caused by the influence of the ground on the value of the antenna voltage-transfer ratio. This is a result of fluctuation of the receiving-antenna input impedance with height and changing ground conditions. An approximate method is presented for calculating the input impedance of horizontal dipole antennas over earth having finite values of dielectric constant and conductivity. The effect of both changes in ground conditions and antenna terminating impedance on the above error is calculated as a function of the antenna height. Measured values are presented in support of the above method, and the results are discussed.

I. Introduction

As is known, VHF field-intensity measurements will be generally in error if made at antenna heights other than that for which the antenna constant was determined when the field-intensity meter was calibrated. An error will likewise exist if the ground constants at the site chosen to make measurements are appreciably different from those existing at the time or place of calibration.

At present most VHF field-intensity meters use a doublet receiving antenna, which is usually terminated at its center terminals in an impedance roughly equal in value to its free-space input impedance. The error referred to exists because of the change of the antenna-input impedance with height above ground or with changing ground conditions[1]. This results in a corresponding fluctuation in the *proportion* of the induced voltage that appears across the terminals at the center of the antenna. Consequently the value of the antenna constant determined at the time of the calibration is in general not the same if the height or ground conditions are altered.

An approximate expression for the input impedance at various heights above a finitely conducting ground may be easily obtained for the case of a horizontal antenna. The ground is assumed to be plane, homogeneous, and with finite values of the relative dielectric constant ϵ_r, and conductivity σ. Once the antenna-input impedance is known, the effect of the earth on the antenna constant may be determined.

Although the solution attempted here is not rigorous, it can be shown to yield the limiting value of the input impedance of a horizontal antenna if its height above ground is increased sufficiently. The results, however, are useful in obtaining approximate values of the input impedance corresponding to antenna heights of a fraction of a wavelength.

Theoretical values of the measurement error are reasonably well supported by measurement at one particular site for antenna heights down to one-tenth wavelength at 100 Mc. The effect both of changes in ground conditions and of the value of the antenna terminating impedance upon this error are determined. Practical rationalized mks units are used throughout.

II. Theory

In formulating the following solution, the usual system will be considered, comprising a transmitting and receiving antenna at heights h_1 and h_2, respectively, above ground. The ground is assumed to be plane, homogeneous, and of infinite extent, having finite values of relative dielectric constant ϵ_r and conductivity σ. Although the

[1] It is assumed here that the field-intensity meter is calibrated and used at such locations that the distances to the nearest reflecting objects such as trees or buildings are very much greater than the heights of the receiving antenna above the ground.

method is applicable to horizontal antennas of any length, the results will be evaluated only for the case of parallel horizontal half-wave dipoles. Their locations and the geometry involved are shown in figure 1.

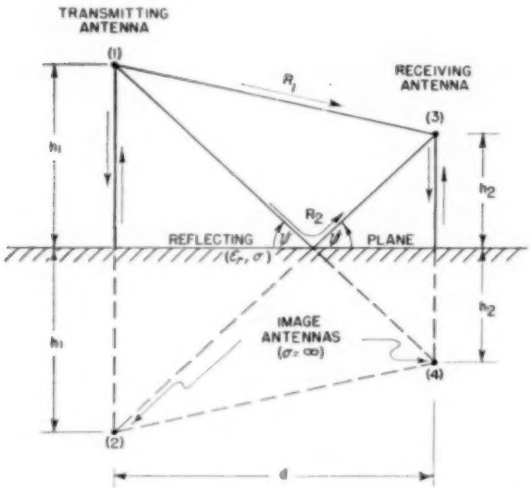

FIGURE 1. *Ray-path diagram showing: direct ray along R_1; ground-reflected ray along R_2; rays from both horizontal transmitting and receiving antennas reflected at normal incidence from the ground back to the antenna.*

Heights of the transmitting and receiving antennas are h_1 and h_2 respectively, and d is the horizontal distance of separation.

In addition to the direct and ground-reflected rays along R_1 and R_2, respectively, a ray will be considered that leaves each antenna and is reflected at normal incidence from the ground back to the antenna.

1. Perfectly Conducting Ground

Perfectly conducting ground will be considered first. Its effect may be simulated in the usual manner by postulating the image antennas (2) and (4), each located at a distance below the perfect reflecting plane equal to the height of the actual antenna. The two antennas and their images may be treated as four coupled antennas. The resulting voltage-current relationship will have exactly the same form as would exist in a linear four-mesh network. For this case [2] the resulting four equations reduce to the following two:

$$\left.\begin{aligned} V &= I_1(Z_{11}-Z_{12})+I_3(Z_{13}-Z_{14}),\\ O &= I_1(Z_{31}-Z_{32})+I_3(Z_{33}-Z_{34}),\end{aligned}\right\} \quad (1)$$

where V is the impressed emf at the center of the transmitting antenna, and I_1, and I_3, are the respective currents at the centers of the transmitting and receiving antennas. The terms Z_{11} and Z_{33} are the free-space self impedances, respectively, of the transmitting and receiving antennas referred to the center terminals. Also

$$Z_{mn}=Z_{nm}=-\frac{V_{mn}}{I_n}, \quad (2)$$

where Z_{mn} is the mutual impedance between antennas m and n, and V_{mn} is the emf induced in antenna m (referred to the center terminals) by the current, I_n, at the center of antenna n.

2. Finitely Conducting Ground

In considering the case involving a finite earth, the equations for meshes (2) and (4) of the previous system become meaningless. However, by benefit of analogy with eq 1 and with the aid of experimental evidence, one may write a similar set of equations involving antennas (1) and (3) and the ground, which under certain conditions describe this transmission system to a first approximation at least. The equations are:

$$\left.\begin{aligned} V &= I_1(Z_{11}+\Gamma_1 Z_{12})+I_3(Z_{13}+\Gamma_2 Z_{14}),\\ O &= I_1(Z_{31}+\Gamma_2 Z_{32})+I_3(Z_{33}+\Gamma_1 Z_{34}),\end{aligned}\right\} \quad (3)$$

where $\Gamma_1 \equiv \rho_1 e^{-j\theta_1}$ = complex plane-wave reflection coefficient for vertical incidence; $\Gamma_2 \equiv \rho_2 e^{-j\theta_2}$ = complex plane-wave reflection coefficient (horizontal polarization) for the angle $\psi = \tan^{-1}(h_1+h_2)/d$ made with the earth by the principal ground-reflected ray (along R_2).

The reflection coefficient, Γ_2, may be expressed in terms of the angle ψ and a complex dielectric constant ϵ_0 as follows [3] (for horizontal polarization):

$$\Gamma_2 = \frac{\sin\psi - \sqrt{\epsilon_0 - \cos^2\psi}}{\sin\psi + \sqrt{\epsilon_0 - \cos^2\psi}} \quad (4)$$

where $\epsilon_0 = \epsilon_r\left(1 - j\frac{\sigma}{\epsilon\omega}\right)$,

$= \epsilon_r - j\,60\,\lambda\sigma$,

[2] P. R. Karr, The influence of the ground upon the voltage induced in a receiving antenna, Report OD-2-348R (NBS) (July 23, 1947).

[3] J. A. Stratton, Electromagnetic theory, p. 493 (McGraw-Hill Book Co., Inc., New York, N. Y., 1941).

ϵ_r = relative dielectric constant of the ground (referred to free-space as unity),

$\epsilon = \epsilon_0 \epsilon_r$, where ϵ_r is the permittivity of evaluated free-space,

$\epsilon_0 \cong \frac{1}{36\pi} \times 10^{-9}$ farads/meter,

σ = ground conductivity is mhos/meter,

$\omega = 2\pi f$,

λ = wave length in meters,

$j = \sqrt{-1}$.

Equations 3 will reduce to eq 1 if the ground conductivity σ is allowed to increase without limit, since in this case $\Gamma_1 = \Gamma_2 = -1$ for all angles of incidence, as can be seen from eq 4.

3. Evaluating the Self and Mutual Impedances

Before practical use can be made of eq 3, the various self and mutual impedances must be evaluated. Schelkunoff [4] has determined the free-space input impedance of cylindrical antennas in general. Values may be obtained graphically from figs. 11.21 and 11.22 of this reference for antennas of several length-to-diameter ratios. A value of $73.2 + j\,42.5$ (ohms) may be used if desired, corresponding to a thin $\lambda/2$ dipole in free-space, without substantially affecting the resulting value of the measurement error. Carter [5] has evaluated the mutual impedance between antennas of various configurations. For the case of parallel half-wave dipoles in free-space the mutual impedance in ohms is:

$$Z = 30\{2\mathrm{Ei}(-jkR) - \mathrm{Ei}[-jk(\sqrt{R^2+l^2}+l)] - \mathrm{Ei}[-jk(\sqrt{R^2+l^2}-l)]\}, \quad (5)$$

where l = antenna length in meters,

R = distance between antennas in meters,

$\mathrm{Ei}(-jx) \equiv \mathrm{Ci}(x) - j\mathrm{Si}(x)$,

$\mathrm{Ci}(x) \equiv -\int_x^\infty \frac{\cos t}{t}\,dt$,

$\mathrm{Si}(x) \equiv \int_0^x \frac{\sin t}{t}\,dt$,

$k \equiv 2\pi/\lambda$.

Values of eq 5 are shown plotted in figures 11 and 12 of the reference given in footnote 5 for spacings from 0 to 7.5 wavelengths.

It is possible to derive a more simple expression than eq 5, valid for distances of separation in excess of about 2λ. At this distance from an antenna, only the radiation component of the electric field-intensity usually need be considered. For a half-wave transmitting dipole in free-space, oriented normal to a line from its center to the point of observation, the field intensity is (in volts/meter)

$$E \cong -j\frac{60I}{R} e^{\frac{-j2\pi R}{\lambda}}, \quad (6)$$

where R = distance in meters,

I = current in amperes at the center of the antenna.

The voltage (referred to the center terminals) induced in a half-wave dipole placed in the field given by eq 6 and oriented parallel to the transmitting antenna is (in volts)

$$V \cong El_H \cong -j\frac{60\lambda I}{\pi R} e^{\frac{-j2\pi R}{\lambda}}, \quad (7)$$

where l_H = effective length of the dipole in meters,

$l_H = \lambda/\pi$ meters for a half-wave dipole assuming sinusoidal current distribution.

From eq 7 and 2 the mutual impedance between the two parallel half-wave dipole antennas is (in ohms)

$$Z = -\frac{V}{I} \cong j\frac{60\lambda}{\pi R} e^{\frac{-j2\pi R}{\lambda}}. \quad (8)$$

It can be shown that eq 8 is the limiting value of eq 5 for sufficiently large values of the distance of separation, R. In fact, for separations in excess of about 2λ, the value of mutual impedance given by eq 8 is sufficiently accurate for many purposes [6] and will cause less than 0.1-percent error in the final results in which we are interested here. For smaller values of separations between the antennas than 2λ, eq 5, or figures 11 and 12 of the reference given in footnote 5 must be used to evaluate the mutual impedance.

[4] S. A. Schelkunoff, Electromagnetic waves, pp. 441 to 479 (D. Van Nostrand Co., New York, N. Y., 1943).

[5] P. S. Carter, Circuit relations in radiating systems and applications to antenna problems, Proc. IRE **20**, pp. 1004 to 1041 (June 1932).

[6] Kosmo J. Affanasiev, Simplifications in the consideration of mutual effects between half wave dipoles, Proc. IRE **34**, pp. 635 to 638 (Sept. 1946).

III. Relations Existing in the Receiving Antenna

1. Antenna Current

Equations 3 may now be solved for the current I_3 at the center of the receiving antenna. The problem will be simplified if it is assumed that the distance between transmitting and receiving antennas is sufficiently large that the presence of the receiving antenna does not measurably affect the current flowing in the transmitting antenna. This is usually the case in practice, and the assumption is certainly justified if the spacing is at least several wavelengths. In this case the current in the receiving antenna terminated at its center in a load impedance Z_L is, from eq 3:

$$I_3 = -\frac{(Z_{31}+\Gamma_2 Z_{32})I_1}{Z_L+Z_{33}+\Gamma_1 Z_{34}}. \tag{9}$$

2. Input Impedance

The numerator of eq 9 is the induced emf in the receiving antenna, and the denominator is the input impedance (in the presence of the ground) plus the terminating impedance Z_L connected at the center, the input impedance being

$$Z_i \equiv Z_{33}+\Gamma_1 Z_{34}. \tag{10}$$

The effect of the ground in the immediate vicinity of the receiving antenna is accounted for by the second term on the right of eq 10, $\Gamma_1 Z_{34}$. Z_{34} is the mutual impedance that would exist between the receiving antenna and its image if the ground were perfectly conducting, and is given by eq 5 or eq. 8 upon substituting $R=2h_2$. Γ_1 is of course the actual reflection coefficient of the ground for normal incidence obtained from eq. 4 by placing $\psi=\pi/2$, which gives

$$\Gamma_1 = \frac{1-\sqrt{\epsilon_r\left(1-j\,\frac{\sigma}{\epsilon\omega}\right)}}{1+\sqrt{\epsilon_r\left(1-j\,\frac{\sigma}{\epsilon\omega}\right)}} \tag{11}$$

Values of the magnitude of eq. 11, ρ_1, are shown plotted vs ϵ_r in figure 2 for low-loss dielectrics, $(\sigma/\epsilon\omega<<1)$. Many types of ground may be treated as low-loss dielectrics over a large portion of the VHF band as far as their reflecting properties are concerned. This is particularly true at the higher frequencies above 50 or 75 Mc. Under these conditions the phase shift on reflection, ϕ, is very nearly 180°, so that $\Gamma_1 \cong -\rho_1$.

3. Voltage Relations

The terminal voltage of the receiving antenna terminated in an impedance Z_L is, from eq. 9

$$V_L = -\frac{(Z_{31}+\Gamma_2 Z_{32})Z_L I_1}{(Z_L+Z_{33}+\Gamma_1 Z_{34})}, \tag{12}$$

and the open-circuit voltage is, letting $Z_L \to \infty$,

$$V_{oc} = -(Z_{31}+\Gamma_2 Z_{32})I_1. \tag{13}$$

If the receiving antenna is sufficiently high above the ground, Z_{34} may be considered negligible compared to (Z_L+Z_{33}), in which case the terminal voltage will be, from eq 12,

$$V_L = -\frac{(Z_{31}+\Gamma_2 Z_{32})Z_L I_1}{Z_L+Z_{33}}. \tag{14}$$

The true value of the electric component of field intensity at any antenna height, h_2, above the ground is, from eq 7 and 13:

$$E_t = \frac{V_{oc}}{l_H} = -\frac{(Z_{31}+\Gamma_2 Z_{32})I_1}{l_H}. \tag{15}$$

The value of field intensity that would be indicated by a field-intensity meter previously calibrated in the presence of the ground is, from eq 12

$$E_i = KV_L = -\frac{K(Z_{31}+\Gamma_2 Z_{32})Z_L I_1}{(Z_L+Z_{33}+\Gamma_1 Z_{34})}. \tag{16}$$

K may be defined as the antenna constant and may be evaluated at any desired height of the receiving antenna. If a height h_2 is chosen such that $Z_{34} \ll (Z_L+Z_{33})$, K might then be termed the free-space antenna constant and in such a case its value would be

$$K \cong \frac{1}{l_H}\left(\frac{Z_L+Z_{33}}{Z_L}\right), \tag{17}$$

since $E_t \cong E_i$ at this height. The antenna constant is seen to be the reciprocal of the product of the effective length, l_H, and the voltage-transfer ratio, $V_L/V_{oc}=Z_L/(Z_L+Z_{33})$.

The assumption is made here that the *relative* current distribution and hence the effective length of the half-wave receiving dipole is not (to a

first approximation) a function of either the terminating impedance, Z_L, or the height of the antenna above ground. Although a complete solution to the general problem of the receiving antenna has unfortunately not yet been achieved, this assumption is supported by a number of our measurements.[7]

IV. Evaluation of the Measurement Error

The difference between the true value of field intensity existing at some antenna height h_2, and that indicated by a field-intensity meter with a previously determined antenna constant is (in percent)

$$\delta=\left(\left|\frac{E_i}{E_t}\right|-1\right)\times 100. \tag{18}$$

For the case in which the antenna constant, K, was determined at a sufficient antenna height that it may be considered to have a free-space value, the above difference, or measurement error, may be obtained by substituting eq 15, 16, and 17 in eq 18, giving (in percent)

$$\delta=\left(\left|\frac{Z_L+Z_{33}}{Z_L+Z_{33}+\Gamma_1 Z_{24}}\right|-1\right)\times 100. \tag{19}$$

Z_L = load impedance connected to the center terminals of the receiving antenna.

Z_{33} = input impedance (in free space) of the receiving antenna. Z_{33} may be evaluated from figures 11.21 and 11.22 of the reference given in footnote 4 or if desired may be taken as $73.2+j42.5$ (ohms) corresponding to a thin $\lambda/2$ dipole in free-space, without substantially affecting the resulting value of the measurement error.

Z_{24} may be evaluated from eq 5, or from figures 11 and 12 of the reference given in footnote 5. For heights of the receiving antenna $h_2 \geqq \lambda$, Z_{24} may be evaluated from eq 8, placing $R=2h_2$. This gives (in ohms)

$$Z_{24}=j\frac{30\lambda}{\pi h_2}e^{-j\frac{4\pi h_2}{\lambda}}. \tag{20}$$

Γ_1 = plane-wave reflection coefficient for normal incidence. Γ_1 may be evaluated from eq 11, or in the case of low-loss dielectrics, from figure 2, since $\Gamma_1 \cong -\rho_1$.

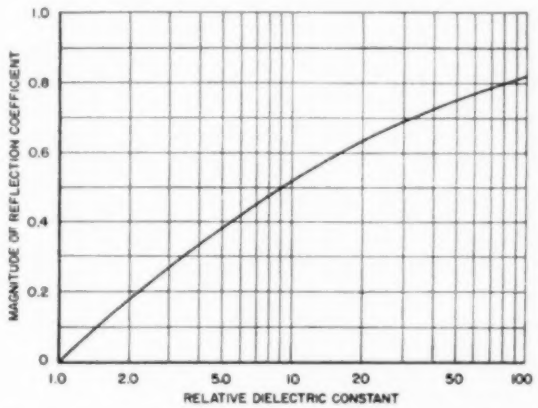

FIGURE 2. *Magnitude of the plane-wave reflection coefficient, ρ_1 (at normal incidence) vs the relative dielectric constant, ϵ_r.*

Low-loss dielectrics are assumed ($\sigma/\epsilon\omega \ll 1$). $\Gamma_1 = -\rho_1$.

V. Discussion of Results

The measurement error to be discussed is that existing in a field-intensity meter whose antenna constant was determined under free-space conditions. This error or difference (as calculated) is given by eq 19 and is shown in figures 3 and 4 vs h_2/λ for various values of the parameters Γ_1 and Z_L. Measured values of the error determined at one particular site as well as the corresponding calculated values ($f=100.0$ Mc) are shown in figure 5.

Figure 3 shows the effect of changes in the ground constants on the measurement error calculated for an antenna terminated in an impedance $Z_L=73+j0$ ohms. The self-impedance of the antenna was assumed to be $73.2+j\,42.5$ ohms. Curves are shown for (A) $\sigma=\infty$, (B) $\epsilon_r=30$, (C) $\epsilon_r=15$, and (D) $\epsilon_r=9$. Low-loss dielectrics were assumed in the last three cases.

The high and low values of the relative dielectric constant chosen represent the approximate extremes measured at one particular site ($f=100.0$ Mc) during the summer of 1948 (see footnote 7). The value, $\epsilon_r=15$, is usually assigned to average ground, along with a value of conductivity $\sigma=5\times10^{-3}$ mhos/meter. Values of conductivity of this order of magnitude can be ignored, at least for frequencies above 50 Mc as far as the

[7] Further details are contained in a forthcoming Bureau paper entitled "Development of VHF field-intensity standards", by F. M. Greene and M. Solow.

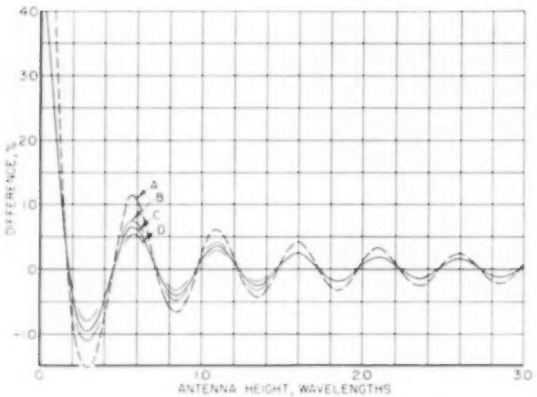

FIGURE 3.—*Calculated percentage difference* $(|E_i/E_t|-1)\times 100$ *vs receiving antenna height,* h_2/λ, *in wavelengths.*

E_t is the true value of field intensity, and E_i is the value indicated by a field-intensity meter with a previously determined free space value of antenna constant (horizontal polarization). Curves are shown for four values of ground constants: (A) $\sigma=\infty$; (B) $\epsilon_r=30$; (C) $\epsilon_r=15$; and (D) $\epsilon_r=9$ (for low-loss dielectrics $\sigma/\epsilon\omega<<1$). Antenna length $l=\lambda/2$. The free-space antenna input impedance is taken as $Z_{21}=73.2+j42.5$, and the terminating impedance $Z_L=73+j0$ ohms.

effect on the reflection coefficient ($\psi=\pi/2$) is concerned.

Apparently the usual changes in the ground constants experienced (due to changing moisture content) have but little effect upon the measurement error as presented here. The total variation from average ground conditions ($\epsilon_r=15$) does not exceed 1.5 percent, except for values of h_2/λ <0.15.

As shown by figure 3, a field-intensity meter

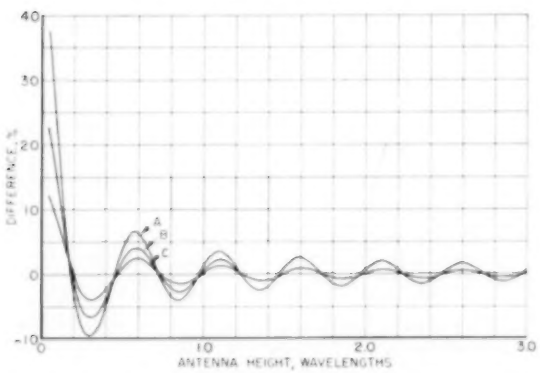

FIGURE 4. *Calculated percentage difference in field intensity (horizontal polarization)* $(|E_i/E_t|-1)\times 100$ *vs receiving antenna height,* h_2/λ, *in wavelengths for three values of antenna terminating impedance.*

(A) $Z_L=73$; (B) 150, and (C) 300 ohms, over average ground $\epsilon_r=15$, $\sigma/\omega<<1$, $l=\lambda/2$, $Z_{21}=73.2+j42.5$

($Z_L=73\Omega$) calibrated under free-space conditions may indicate values of field intensity that are in error by as much as 10 percent for values of h_2/λ near 0.3, and 7.5 percent for values of h_2/λ near 0.6. If this error is to be held to values less than 5 percent, antenna heights greater than about 0.65 wavelength should be used for field-intensity measurements under these conditions.

It is somewhat doubtful at the present state of the art just what maximum values of measurement error of this type should be permitted. One method of reducing the error, obviously, is to increase the value of the antenna terminating impedance, Z_L.

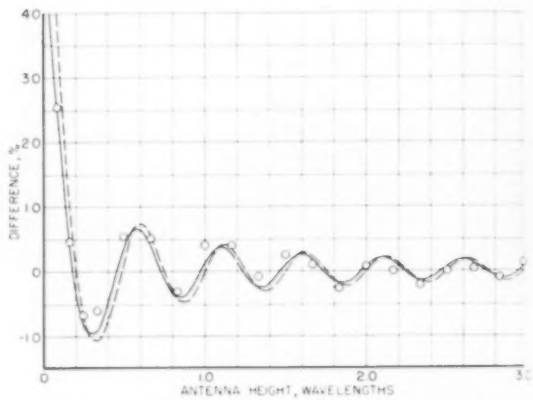

FIGURE 5.—*Calculated percentage difference in field intensity (horizontal polarization)* $(|E_i/E_t|-1)\times 100$ *vs receiving antenna height,* h_2/λ, *in wavelengths over average ground,* $\epsilon_r=15$, $\sigma/\epsilon\omega<<1$, *for both a half-wavelength dipole and a self-resonant dipole* ($l\cong\lambda/2$).

The measured points were determined at 100.0 Mc and were obtained from the data presented in figure 7. ——— , self-resonant dipole; ———— , $\lambda/2$ dipole; ○, observed for self-resonant dipole.

Figure 4 shows the calculated measurement error vs h_2/λ for values of $Z_L=73$, 150, and 300 ohms for average ground, $\epsilon_r=15$, ($\sigma=0$). For the case of $Z_L=73$ ohms, the error does not exceed 10 percent for heights of the receiving antenna in excess of 0.15 wavelength. If Z_L is increased to 150, and 300 ohms, this error is reduced to 7 and 4 percent, respectively, and approaches zero as Z_L approaches infinity.

Figure 5 shows the computed measurement error for both a $\lambda/2$ dipole and a self-resonant dipole, as well as measured values for the latter case ($f=$ 100 Mc). In the case of the $\lambda/2$ dipole, $Z_{21}=73.2$ $+j$ 42.5 ohms, and $Z_L=73+j$ 0 ohms. For the

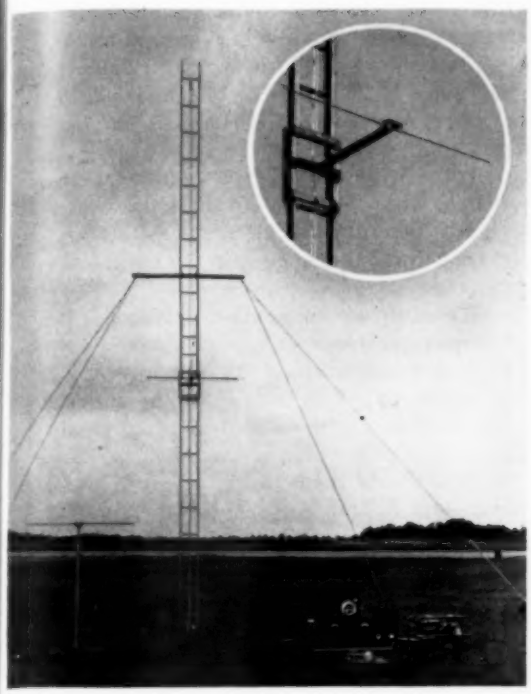

FIGURE 6. *View of the various pieces of transmitting and receiving equipment used in obtaining the measured data of figure 7.*

In the background is shown the ladder-mast and carriage for the receiving dipole. The location is the Beltsville, Md., airport.

self-resonant dipole, $Z_{33}=65+j\ 0$ ohms, and $Z_L=62+j\ 0$ ohms.

The latter values were chosen as representing the approximate impedances of the self-resonant antenna actually used for obtaining the measured points of figure 5. The terminating impedance, $Z_L=62+j\ 0$ ohms, was the closest value to 65 ohms available at the time the measurements were made. As might be expected, there is no substantial difference between the calculated values of the measurement error for the full $\lambda/2$ dipole and for the self-resonant dipole. The measured points support the theory reasonably well. The difference does not exceed 3 percent for antenna heights above 0.1 wavelength. Various pieces of the transmitting and receiving equipment used in making these measurements are shown in figure 6.

The measured values of figure 5 were obtained from the data presented in figure 7. In the latter, the receiving antenna terminal voltage (horizontal polarization) is shown vs height, h_2, in meters over ground having a measured relative dielectric constant $\epsilon_r \cong 15$, $(\sigma/\epsilon\omega << 1)$ for: (A) antenna "open-circuited"; and (B) antenna terminated in $Z_L=62+j\ 0$ ohms. The measured percentage difference shown in the upper curve of figure 7 was determined from the data with the aid of eq 18 which, upon substituting eq 15 and 16, gives (in percent)

$$\delta=\left(Kl_H\left|\frac{V_L}{V_{oc}}\right|-1\right)\times 100. \qquad (21)$$

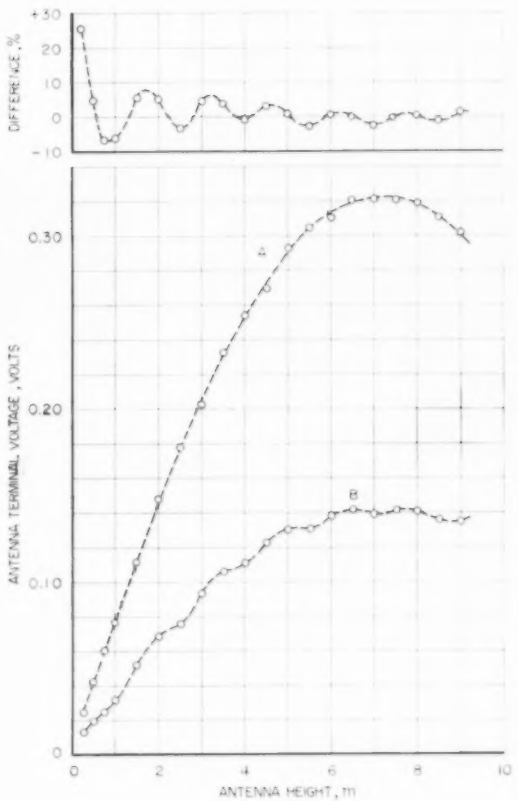

FIGURE 7.—*Measured values of receiving antenna terminal-voltage (horizontal polarization) vs height in meters over ground having a measured relative dielectric constant* $\epsilon_r=15$, $(\sigma/\epsilon\omega << 1)$ *for: (A) antenna "open-circuited"; and (B) antenna terminated in* $Z_L=62+j\ 0$ ohms

The measured percentage difference was determined with the aid of eq 21, $\delta=(Kl_H V_L/V_{oc}-1)\times 100$. The free space value of the factor $Kl_H=(Z_L+Z_{11})/Z_L=V_{oc}/V_L$ (see eq 17) was estimated from the data, and is the reciprocal of the voltage-transfer ratio. $f=100.0$ Mc, $d=30.5$ m, $h_1=3.05$ m, $I=0.100$ amp.

The free-space value of the factor, $KI_H=(Z_L+Z_{33})/Z_L=V_{oc}/V_L$, used, was estimated from the data, and is the reciprocal of the voltage-transfer ratio previously mentioned.

For the open-circuited condition referred to above, the receiving antenna was actually terminated in a special balanced voltmeter of the silicon crystal-rectifier type. This crystal rectifier, together with the balanced RC network used to take off the direct-current output voltage, presented a resistance of approximately 4,000 ohms in shunt with 0.75 $\mu\mu$f across the gap at the center of the antenna. This accounts for the slight oscillation of the points around the averaging curve, but introduced an error of less than 1 percent in the final results, as the shunting was present during both the open-circuited and terminated runs.

VI. Conclusions

An approximate method has been presented for determining the effect of finitely conducting ground beneath a horizontal receiving dipole on the value of the antenna constant as used for measuring VHF field intensity. Three variables are mainly involved in this effect: (a) the antenna height, in wavelengths, h_2/λ, (b) the ground constants ϵ_r and σ; (c) the antenna terminating impedance Z_L.

Changes in antenna height probably have the greatest effect on the antenna constant, as can be seen from figure 3, and are of primary concern here. Normal variations in the ground constants encountered in practice apparently have only a minor effect. Under most conditions and to within the probable accuracy of this method, these variations can probably be neglected.

This error[8] in measurement caused by the ground may be reduced by increasing the value of Z_L. The error vs height is shown in figure 4 for three values of Z_L, viz, 73, 150, and 300 ohms. The error approaches zero as Z_L approaches infinity.

In figure 5, measured values of the error are compared with theoretical values calculated as previously described. The agreement is reasonably good for antenna heights above 0.1 wavelength.

In view of the approximations involved it is felt that the curves shown in figures 3, 4, and 5 probably should not be used for actually applying corrections to field-intensity measurements. Rather they might be used to estimate the maximum probable error (due to ground effect) existing in measurements made below a given antenna height.

Figure 3 shows the variations in the error with antenna height occurring over perfectly conducting ground.[9] The error is appreciably larger in this case than for finitely conducting ground. This would seem to indicate the inadvisability of using or calibrating a VHF field-intensity meter over a perfectly conducting plane unless the antenna heights were carefully chosen so as to result in a low value of error.

[8] The error, as previously defined, is the percentage-difference between the true value of field intensity existing at a given antenna height, in wavelengths, h_2/λ and that indicated by a field-intensity meter whose antenna constant was determined under free-space conditions.

[9] Perfectly conducting ground and a solid metallic ground plane would have essentially the same reflecting properties for the present purpose.

Washington, October 18, 1949.

U. S. Department of Commerce
National Bureau of Standards

Research Paper RP2063
Volume 44, February 1950

Part of the Journal of Research of the National Bureau of Standards

Determination of Curvature by an Osculometer

By Harvey L. Curtis

The experimental determination of the curvature at a point of a plotted curve can be made by means of an osculometer, which is a series of arcs of known curvature. One use of such information is in the computation of the acceleration of a body for which a displacement-time curve has been constructed. By this method the acceleration can be obtained with the same accuracy as by double differentiation without the necessity of plotting the velocity time curve.

I. Introduction

The curvature of a curve at any point is defined as the reciprocal of the radius of the osculating circle at that point. If the equation of the curve is known, the curvature can be determined by analytical methods. However, the equations of most experimental curves are not known, so that a graphical method of determining the curvature is sometimes useful. The osculometer is a device for graphically determining the curvature at a given point on a curve by comparison with a series of arcs of known curvature. Its greatest usefulness is when the data are so plotted that the radius of curvature at points to be measured is more than 10×10^{-3} reciprocal centimeters.

II. Types of Osculometers

Two types of osculometers have been developed, the single-line osculometer and the double-line osculometer. The single-line osculometer shown in figure 1 consists of a series of arcs of circles, which are uniformly distributed along the axis of the osculometer and which have uniformly increasing curvatures. The centers of the circles of which the arcs are a part all lie in the axis. For general use, the simple osculometer consists of black lines on the lower surface of a rectangular sheet of transparent material. For convenience in use, the axis of the osculometer is midway between the long sides of the rectangle. The paper on which is drawn the curve to be studied is laid on a flat surface and a point on the curve selected at which the curvature is to be determined.

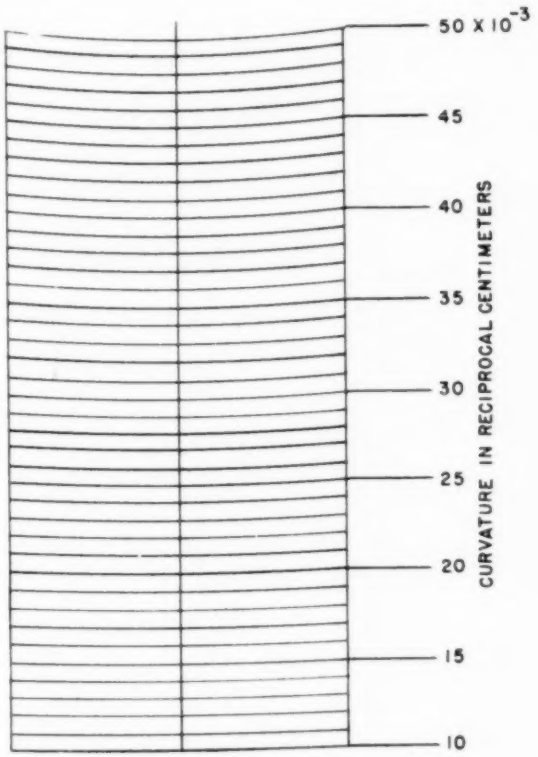

FIGURE 1. *Single-line osculometer, solid arc.*

The osculometer is placed over the curve with its axis normal to the curve at the selected point. It is then moved axially until there is found an arc that fits the curve at that point. The curvature is then read from the scale of the osculometer.

The instrument as described has the disadvantage that, when the arc is fitted, it may obscure the curve being studied. Two methods of avoiding this difficulty while using a single line osculometer have been used. In the first, the arcs were made as clear lines on an opaque or semi-opaque surface. The curve to be studied was then drawn on translucent paper and the comparison made on a diffusing surface that was illuminated from underneath. Another way of overcoming the difficulty was to make each arc as a series of dashes. The curve then was seen between the dashes. This scheme may be advantageous with either the dark line or the bright line instrument. Other modifications can readily be devised.

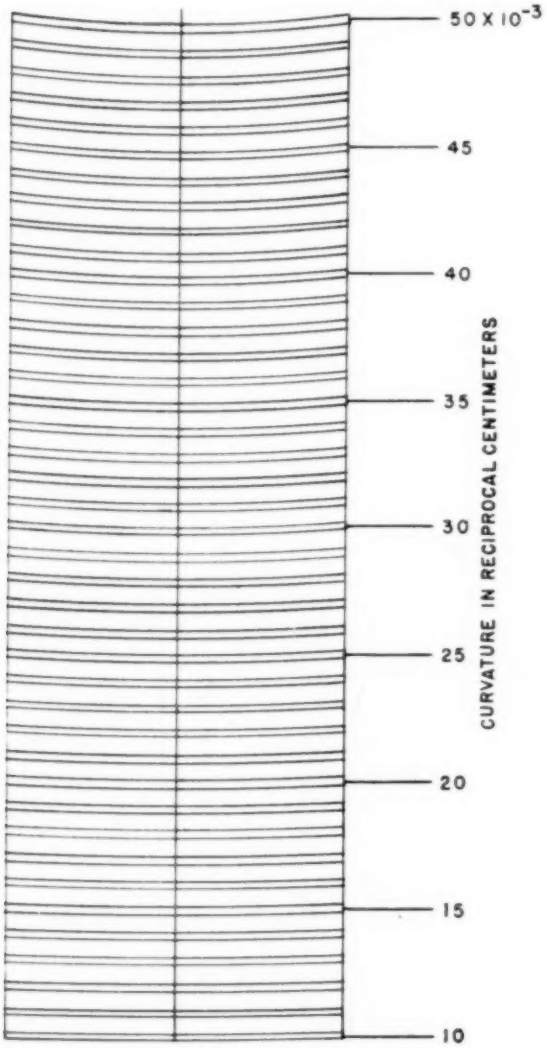

FIGURE 2. *Double-line osculometer.*

The double-line osculometer shown in figure 2 was developed so that the observed curve would at all times be visible. Two arcs of the same curvature are drawn, the distance between them being about 1 mm. The distance between successive members of the series is 3 or 4 mm, so that the different members stand out distinctly from the individual pairs. In use, the curve to be studied is made to lie between the two curves having the same curvature as shown in figure 2. With such an instrument, the curvature at a point can usually be determined to 1×10^{-3} reciprocal centimeters, provided the curvature is approximately constant for a distance of 2 cm on both sides of the point that was selected. Some operators find the double-line osculometer easier to use than the single-line instrument. Any difference in accuracy has not been demonstrated.

In constructing either type of instrument the lines are first ruled on a transparent sheet of plastic, such as Plexiglass. The rulings are then transferred to a photographic plate by contact printing. This gives an accelerometer with black lines on a clear surface. A print of this accelerometer gives clear lines on a black surface.

III. Use of the Osculometer in Determining Acceleration

By using an osculometer, the acceleration of a body at any time or position can be obtained directly from its displacement-time curve, which is the plot of time as abscissae with displacements as ordinates. A point on this curve is selected at which a value of the acceleration is desired. An osculometer is selected that has an arc that will fit the curve at the selected point. When an arc has been fitted to the curve at that point, the curvature, C, is read directly from the osculometer and the slope, tangent θ, is determined from a measurement with a protractor of the angle that the base of the osculometer makes with the x-axis.

The acceleration, α, is equal to $\frac{d^2s}{dt^2}$, and hence is proportional to $\frac{d^2y}{dx^2}$, so that the equation for computing it can be derived from the expression for

the radius of curvature, ρ, given in all texts on differential calculus, viz.:

$$\rho=\frac{\left[1+\left(\frac{dy}{dx}\right)^2\right]^{3/2}}{\frac{d^2y}{dx^2}}.$$

In this equation ρ, x and y are all expressed in the same units. It follows since since $\frac{dy}{dx}=\tan\theta$ that $\frac{d^2y}{dx^2}=[1/\rho]\ [1+\tan^2\theta]^{3/2}=C\sec^3\theta$, where the curvature, C, is defined as $1/\rho$. Applying this to a displacement-time curve, in which the measured displacements are designated as s and the measured times as t: $y=rs$, and $x=rV_0t$, where r is the constant by which a unit displacement is multiplied to give a plotting unit, and V_0 is the velocity by which a unit of time is multiplied to give unit measured length. Then

$$\frac{ds}{dt}=V_0\frac{dy}{dx}.$$

and

$$\frac{d^2s}{dt^2}=rV_0^2\frac{d^2y}{dx^2},$$

and therefore

$$\alpha=\frac{d^2s}{dt^2}=rV_0^2C\sec^3\theta,$$

where C is the curvature in the reciprocal of the length unit of the coordinate system. If the osculometer is calibrated in a unit different from the unit of the coordinate paper, the observed curvature must be multiplied by that conversion factor, which changes a length from the osculometer units to the coordinate units. Thus, if the osculometer is graduated in reciprocal centimeters and the coordinate unit is inches, the observed curvature, C_0, must be multiplied by 2.54 to obtain the curvature, C, in the coordinate system.

IV. Accuracy Attainable in Measuring Acceleration

The accuracy attainable depends both on the accuracy of measuring the slope and on the accuracy of determining the curvature. By taking the logarithmic derivative of the equation:

$$\alpha=rV_0^2C\sec^3\theta,$$

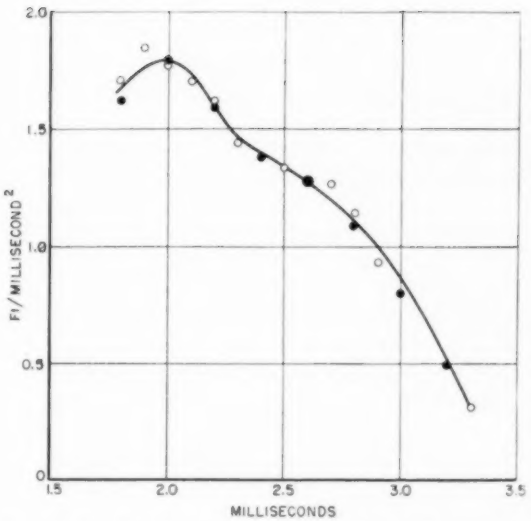

FIGURE 3. *Comparison of results obtained on the same displacement time curve by the osculometer method and by double graphical differentiation.*

○, Acceleration by osculometer; ●, acceleration by double differentiation..

we obtain

$$\frac{d\alpha}{\alpha}=\frac{dC}{C}+3\tan\theta d\theta.$$

This equation gives the error in the acceleration as the sum of accidental errors in the curvature and slope.

For small angles, $\tan\theta$ is small, so that an error, $d\theta$, in measuring the slope may produce negligible effect in the acceleration. Then the relative error dC/C in obtaining the curvature produces the same relative error in the acceleration. Thus if the displacement-time curve has a maximum or minimum, the accuracy at these points depends solely on the accuracy of the curvature determination. In general, the error in the slope measurement does not predominate until θ is more than 45°, but becomes excessive as θ approaches 90°. Hence for determination of the acceleration by an osculometer, the displacement-time curve should be plotted to such a scale that at no point does the slope exceed 45°. On the other hand, the plotting should not be such that the curvature is so small that it cannot be determined with reasonable accuracy. In some cases it may be desirable to plot different parts to different scales. For example, if a body starts its motion from rest and

continually accelerates at an increasing rate, the most precise values of acceleration can be obtained by plotting the early part of the motion with a more condensed time scale than is used during the latter part of the motion.

An experimental determination of the accuracy obtained in measuring acceleration by means of an osculometer was obtained by comparing the results from an observed displacement time curve with the results obtained from the same data by the conventional method of using double differentiation. In the conventional method, the velocity of the accelerating body is obtained at a large number of points from the measurement at each point of the angle which a tangent to the displacement-time curve makes with the X-axis. Then a velocity-time curve is plotted, from which the acceleration is obtained at any point by a measurement of the angle that a tangent to the curve makes with the X-axis. The results by the two methods for a particular set of observations are shown in figure 3. The curve was drawn to approximate the mean of all the points. The results by double differentiation lie, on the average, somewhat nearer the curve. If only acceleration is required, the added labor of constructing the velocity curve will seldom be justified.

WASHINGTON, August 18, 1949.

U. S. Department of Commerce
National Bureau of Standards

Research Paper RP2064
Volume 44, February 1950

Part of the Journal of Research of the National Bureau of Standards

A Multicolumn Countercurrent Molecular Still

By Samuel L. Madorsky

A 10-column countercurrent molecular still, based on refluxing by gravity feeds and circulation of the liquid by means of magnetic pumps, is described. Each column consists of a concentric evaporator having a surface of 300 square centimeters, surrounded by a water-cooled condenser. The still is provided with an overflow cup at the top, a reservoir at the lower end and a pump for raising the liquid from the reservoir to the overflow cup. All the condensates move by gravity from column to column in one direction, and all the residues move similarly in the opposite direction, thus producing countercurrent refluxing of the liquid. The still is designed to operate at such a rate of evaporation that the amount of distillate from each column is slightly greater than the amount of residue from the same column. Operating on a binary mixture, the still gives a separation of the two constituents equivalent to 13 theoretical plates.

I. Introduction

Countercurrent molecular stills in which recombination of fractions is accomplished automatically by means of gravity feeds, have been described previously.[1,2] Each of these stills consists of a long column placed at a small angle to the horizontal and divided into small cells with an evaporating surface of a few square centimeters for each cell. The openings between the cells in these columns are quite large, so that mixing of the vapor between the cells takes place. Under these conditions, each cell represents merely a subdivision of the column and not an actual plate.

The multicolumn countercurrent molecular still described in this paper was designed with these objects in view:

1. To obtain a large evaporating surface so that it could be used commercially for the concentration of individual components in mixtures of liquids different in their molecular weights or vapor pressures, but having similar properties otherwise.

2. To spread the evaporating liquid in a thin film so as to reduce the hold-up.

3. To impart to the thin film a continuous motion over a rough granular surface to cause mixing and thus to prevent depletion in the light constituents.

4. To increase the efficiency of the distillation process by eliminating mixing of the vapor between cells or plates.

II. Multicolumn System

The multicolumn molecular still is a combination of refluxing by gravity feeds and of circulating the liquid by means of pumps. The still described here consists of 10 columns, but any number of columns can be used. The entire apparatus was constructed of Pyrex glass and is shown in figures 1 (diagrammatically) and 2. A single column is shown in detail in figure 3. The column consists of a central tube 2.5-cm outside diameter and 45 cm long. This tube serves as the evaporator and has a surface of 300 cm^2. The evaporator is surrounded by a condenser tube with an inside diameter of 4.1 cm, so that the distance between the evaporating and condensing surfaces across the annular space is 0.8 cm. A short ring partition at the lower end of the annular space forms two concentric annular troughs with a separate outlet from each trough. These troughs and outlets serve to separate the residue from the condensate as they flow down the evaporator and condenser, respectively. At

[1] A. K. Brewer and S. L. Madorsky, J. Research NBS **38**, 129 (1946) RP1764.
[2] S. L. Madorsky, Paul Bradt, and Sidney Straus, J. Research NBS **41**, 205 (1948) RP1918.

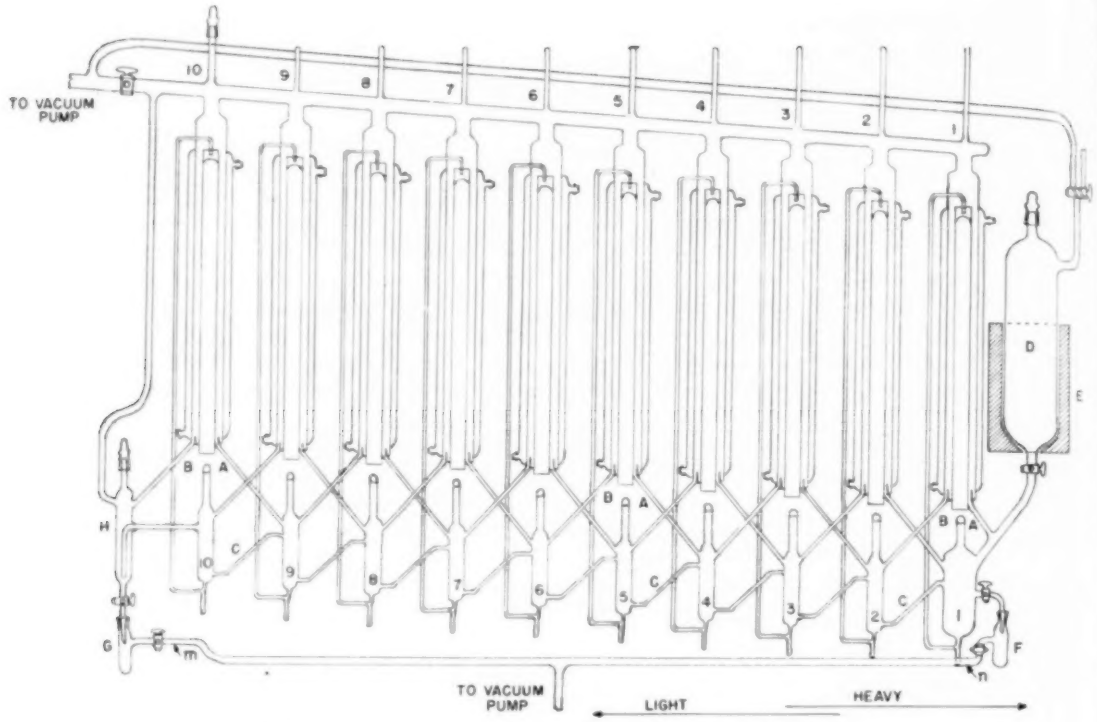

FIGURE 1. *General arrangement of the 10-column molecular still.*

A, Residue outlet; B, condensate outlet; C, overflow; D, degassing reservoir; E, heater; F, heavy fraction sample cup; G, light fraction sample cup.

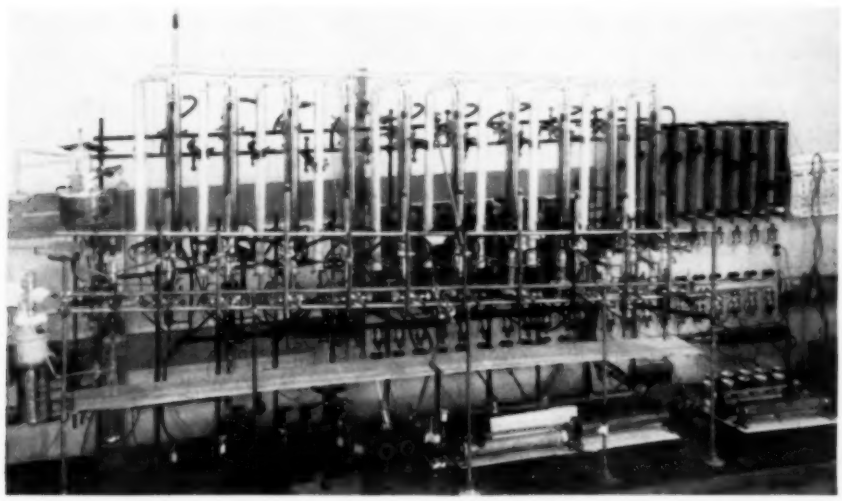

FIGURE 2. *The 10-column molecular still.*

After this photograph was taken, the degassing reservoir was transferred to the right end of the apparatus, as shown in figure 1.

the top of the evaporator is a distributing crown, or cup, provided with several notches half way down the wall of the cup. The evaporating surface is covered with a thin layer of sintered powdered glass of about 40 mesh to facilitate uniform distribution and mixing of the liquid layer.

Each column is provided at its lower end with a combination of magnetic pump and reservoir.

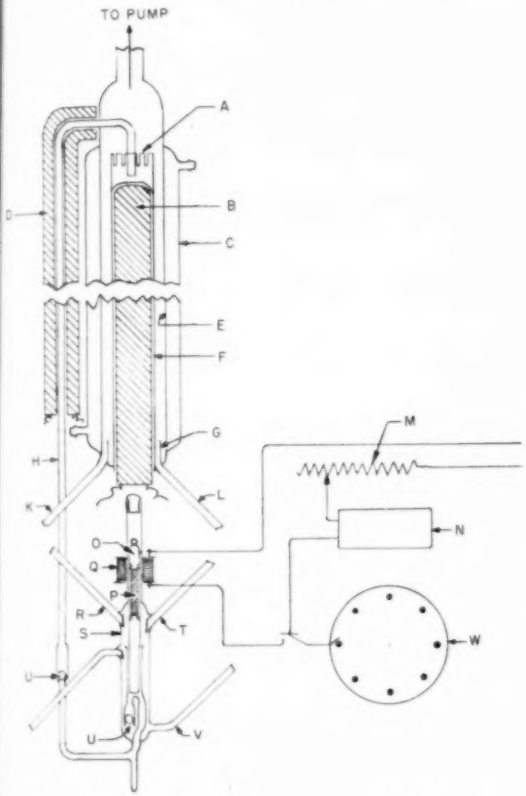

FIGURE 3. *Details of column, reservoir, and pump.*

A, Distributing crown; B, heater; C, condenser; D, preheater; E, condensing surface; F, evaporating surface; G, ring partition; H, feed line; K, condensate outlet; L, residue outlet; M, resistance; N, relay; O, piston; P, iron core; Q, solenoid; R, residue inlet; S, reservoir and pump; T, condensate inlet; U, U, check values; V, overflow; W, intermittent switch.

The liquid is pumped from the reservoir through a feed line into the distributing crown, and from there it distributes itself over the evaporator in a thin layer. In passing through the feed line, the liquid is preheated to a temperature near that of the evaporator. The evaporator is heated by a Nichrome heater fitting snugly inside of it, and the feed line is heated by another Nichrome heater surrounding it, as shown in figure 3. Both heaters are provided with slide resistances in series for the control of temperature and with thermocouples between the heaters and glass tubes. Each heater or preheater has a capacity of about 100 watts.

The columns are arranged from 1 to 10 as shown in figures 1 and 2, in an ascending order from right to left. In this arrangement the residue from each column, except the first, flows through the outlet *A* (fig. 1) into the reservoir of the adjacent lower column to the right. The residue from the first column flows back into its own reservoir. The condensate from each column, except the tenth, flows through the outlet *B* into the reservoir of the adjacent higher column to the left. The condensate from the tenth column flows into a light fraction receiver, *H* (fig. 1) and from there into the reservoir of the tenth column. In this manner, the residues or heavy fractions flow from column to column in the downward direction from left to right, whereas the condensates or light fractions flow from right to left in an upward direction.

In order to keep the system in balance, it is necessary, in the first place, to have the same pumping rate for all columns and, in the second place, to evaporate exactly half of the liquid pumped into the crown of each column. The slightest deviation from one or both of these conditions will cause a gradual accumulation of the liquid in some reservoirs and a depletion in the others. This difficulty can be overcome to some extent by constructing the pumps as uniformly as possible and by equalizing the amplitudes of the pistons in the magnetic pumps. The number of strokes per minute is the same for all the pumps, as the solenoids are operated by the same intermittent switch, *W* (fig. 3).

The evaporating rate is more difficult to control. At any rate, it would be practically impossible to control pumping and evaporating rates to a point where there would be an exact balance between the liquid streams moving in opposite directions. In order to blanket any deviation from conditions of balance, the evaporating rates in the columns were adjusted to a little over 50 percent of the amount of liquid pumped into the crown for each column. The fractions of condensates in excess of residues are allowed to flow by gravity from reservoir to reservoir in the direction from the

light end (reservoir, *H*, fig. 1) to the heavy end (reservoir 1) through overflow tubes, *C*. This is made possible by staggering the reservoirs as well as the columns at an angle of a few degrees to the horizontal, sloping from reservoir, *H*, down to column and reservoir 1. This arrangement serves also the purpose of refluxing the light fractions from reservoir *H* down the series of reservoirs toward the first one.

A large reservoir, *D* (fig. 1), surrounded by a Nichrome heater, *E*, serves to degas the liquid before it is introduced into the still. This reservoir is connected to the same vacuum system as the still, but can be isolated from it by means of stopcocks, when filling it with fresh liquid. The system is evacuated by means of an oil pump backed up by a mercury diffusion pump. Sampling of the liquid can be carried out at the extreme ends of the still into cups *F* and *G* (fig. 1) without interrupting the operation of the still.

III. Magnetic Pump and Reservoir

Details of the magnetic pump [3] and reservoir are shown in figure 4. The pump consists of a piston, *A*, containing an iron core *F*, in its upper end. The core rests on asbestos wool, *K*, and is held in place by means of a sealed-in glass rod. Some mercury is placed in the piston above the iron core to give the piston sufficient weight during its fall to raise a column of liquid to the top of the distillation column. A Nichrome spring, *M*, at the neck of the piston-guide, *P*, serves to cushion the fall of the piston. The solenoid current is controlled by means of an intermittent switch, *W*, shown in figure 3. When the current in the solenoid is on, the piston moves up and draws liquid from the reservoir through check-valve, *Q* (fig. 4), into the piston-guide, *P*. When the current is off, the piston drops by gravity, closing check-valve, *Q*, and forcing the liquid through tube, *S*, and check-valve, *N*, into the delivery tube, *H*.

This type of pump is well adapted to operation in a vacuum. The glass magnetic pump described by Hickman and Hecker [4] has the shortcoming that it is almost impossible to eliminate air or any other gas once it is trapped under the piston. Another shortcoming of the Hickman-Hecker pump is that if anything goes wrong with the piston, the whole pump has to be removed for repairs by breaking. In the present pump any gas trapped in the reservoir or under the piston is easily eliminated in the operation; also, in case the piston jams or breaks, it can be corrected or replaced through a removable waxed-in cap at the top of the pump.

The reservoirs are attached to the columns by means of residue inlets, *E* (fig. 4), distillate inlets, *G*, and delivery tubes, *S-H*, also, to each other by means of overflow tubes *O*, *R*. The ends of the inlet tubes as well as the upper ends of the overflow tubes project into the inside of the re-

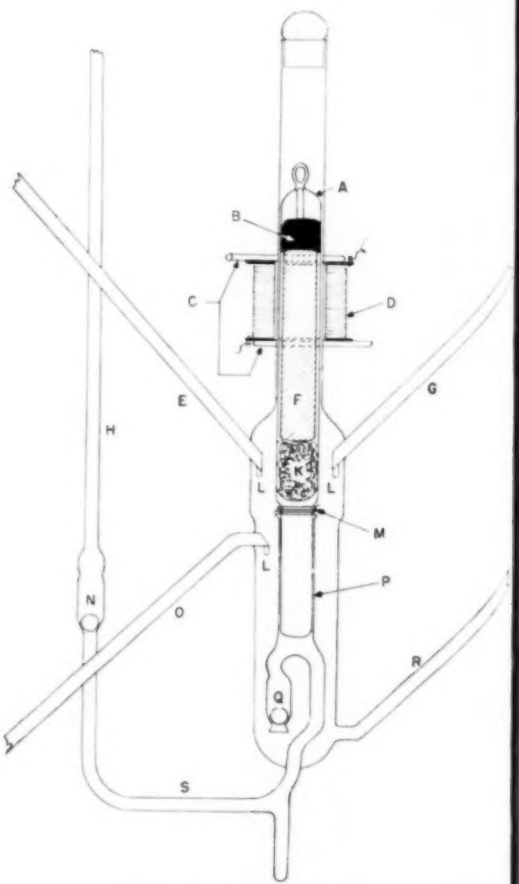

FIGURE 4. *Details of reservoir and magnetic pump*

A, Piston; B, mercury; C, cooling coil; D, solenoid; E, residue inlet; F, ... core, G, distillate inlet; S-H, delivery tube; K, asbestos wool; L, L, ... rods with ground flat ends; M, metal spring; N, Q, check valves; O, R, ... flow tubes; P, piston guide.

[3] S. L. Madorsky, U. S. Patent 2,481,320 (Sept. 1949).
[4] K. C. D. Hickman and J. C. Hecker, U. S. Patent 2,126,467.

ervoir. Short glass rods, *L*, of uniform size and ground flat at the ends, are attached to these projections. Rates of drops of liquid falling from these rods into the reservoir serve as an indication of rates of pumping, evaporation, and overflow for each column.

In experimental tests with a binary mixture operating at a vapor pressure of 0.01 to 0.02 mm Hg, the 10-column molecular still gave at equilibrium a separation of the two constituents equivalent to 13 theoretical plates. The operation was continuous, lasting several weeks at a time and requiring very little attention. The only work involved consisted in counting the drop-rates from points *L*, *L* (fig. 4), checking heating currents and temperatures in heaters and preheaters, and making proper adjustments; also, in breaking off and sealing on again, at intervals, the sample cups, *F* and *G*, at points *m* and *n*, respectively (fig. 1), for analysis of the samples.

WASHINGTON, AUGUST 29, 1949.

U. S. Department of Commerce
National Bureau of Standards

Research Paper RP2065
Volume 44, February 1950

Part of the Journal of Research of the National Bureau of Standards

Hydrocarbons in the 108° to 116° C Fraction of Petroleum[1]

By Augustus R. Glasgow, Jr., Charles B. Willingham, and Frederick D. Rossini

This report describes the analysis of the hydrocarbons in the 108° to 116° C aromatic-free fraction of petroleum, which is shown to be composed of eleven hydrocarbon compounds, of which three are present only in very small amount. For these eleven compounds, the normal boiling points (of high purity samples not from the present investigation) and the estimated amounts by volume in the original Ponca, Okla., crude petroleum are as follows: 2,5-dimethylhexane, 109.11° C, 0.055 percent; 1,*trans*-2,*cis*-4-trimethylcyclopentane, 109.28° C, 0.22 percent; 2,4-dimethylhexane, 109.43° C, 0.055 percent; 2,2,3-trimethylpentane, 109.84° C, 0.004 percent; 1, *trans*-2,*cis*-3-trimethylcyclopentane, 110.4° C, 0.26 percent; 3,3-dimethylhexane, 111.97° C, 0.03 percent; 2,3,4-trimethylpentane, 113.47° C, 0.005 percent; 1,1,2-trimethylcyclopentane, 113.72° C, 0.06 percent; 2,3,3-trimethylpentane, 114.76° C, 0.006 percent; 2,3-dimethylhexane, 115.61° C, 0.06 percent; and 2-methyl-3-ethylpentane 115.65° C, 0.04 percent.

I. Introduction

As part of the work of the American Petroleum Institute Research Project 6 at the National Bureau of Standards on the fractionation and analysis of hydrocarbons in petroleum [1, 2][2] the program has been completed on that part of petroleum normally boiling between 108° and 116° C. In addition to toluene, the separation of which was previously reported [12], this fraction of petroleum is shown to be composed of eleven hydrocarbon compounds, of which three are present only in very small amount. This report describes the foregoing work and gives the detailed results.

II. Material Analyzed

The American Petroleum Institute Research Project 6 at the National Bureau of Standards has had under investigation since 1928 a large quantity of a representative petroleum taken from a well at Ponca, Okla. [2, 10]. The material analyzed in the present investigation constituted that part of this original petroleum normally boiling between the 108° and 116° C, from which toluene had been removed [12]. The status of this material prior to the present investigation is described in reference [5]. The material was made aromatic-free by filtration through silica gel [16].

[1] This investigation was performed as part of the work of the American Petroleum Institute Research Project 6 at the National Bureau of Standards on the "Analysis, Purification, and Properties of Hydrocarbons".

[2] Figures in brackets indicate the literature references at the end of this paper.

III. Method of Analysis and Results

The aromatic-free material of the original petroleum remaining after the previous treatment [4, 5, 11, 12] was "lined-up" by appropriate preliminary distillation and blending in order to obtain in one lot all of the remaining original petroleum normally boiling between 108° and 116° C. The results of this distillation are shown in figure 1. Further separation of this distillate into its constituents is described with respect to the components normally boiling within the ranges 108° to 111° C, 111° to 114° C, and 114° to 116° C, where more or less abrupt changes in the boiling point of the material occurred. The details of the distillations performed in this investigation are given in table 1. Reference [6] gives a description of the distilling columns used.

1. Material normally boiling from 108° to 111° C

The material normally boiling from 108° to 111° was separated by distillation and found to be composed of five compounds, 2,5-dimethylhexane at 109.11°C, 1,*trans*-2,*cis*-4-trimethylcyclopen-

TABLE 1. *Information on the distillation for the analysis and separation of 11 hydrocarbons (3 trimethylcyclopentanes and 8 branched-chain-octanes) from the 108° to 116° C (aromatic-free) fraction of petroleum*

Material	Distillation								
	Distilling [a] column number	Number of equivalent theoretical plates at total reflux (approximately)	Reflux ratio (approximately)	Rate of collection of distillate	Kind of distillation	Azeotrope-forming substance, if used, and its volume	Volume of hydrocarbon charged	Volume of each fraction of distillate	Results plotted in figure
				ml/hr			*ml*	*ml*	
108° to 116° C (aromatic-free) fraction of petroleum (showing lower- and higher-boiling material).	2	100	125/1	2.4	Regular		3,880	7.4	1
108° to 111° C (aromatic-free) portion (part *A*, fig. 1).	11A	200	170/1	4.2	Azeotropic	Ethanol, 6,000 ml	1,950	17.6	2
1,*trans*-2,*cis*-3-Trimethylcyclopentane concentrate (part *B*, fig. 1).	1A	150	135/1	2.2	Regular		460	9.7	3
1,*trans*-2,*cis*-4-Trimethylcyclopentane concentrate (derived from part *A*, fig. 1).	1A	150	300/1	1.0	Azeotropic	Ethanol, 300 ml	138	9.8	4
2,5-Dimethylhexane concentrate (derived from part *A*, fig. 1).	1A	150	335/1	.9	do	Ethanol, 230 ml	110	9.9	5
2,4-Dimethylhexane concentrate (derived from part *A*, fig. 1).	1A	150	335/1	.9	do	Ethanol, 150 ml	58	5.2	6
108° to 110° C (aromatic-free) portion (part *A*, figs. 2 and 3).	1A	150	150/1	2.0	do	Methyl Cellosolve, 750 ml	850	14.3	8
3,3-dimethylhexane concentrate (part *B*, fig. 1).	1A	150	135/1	2.2	do	Methyl Cellosolve, 304 ml	177	17.9	9
1,1,2-Trimethylcyclopentane concentrate (part *C*, fig. 1; part *B*, fig. 9).	1A	150	115/1	2.6	Regular		305	10.1	10
1,1,2-Trimethylcyclopentane concentrate (part *A*, figs. 9 and 10).	4	200	400/1	1.8	Azeotropic	Methyl Cellosolve, 300 ml	84	11.7	11
2,3-Dimethylhexane and 2-methyl-3-ethylpentane concentrate (part *D*, fig. 1).	1A	150	165/1	1.8	Regular		515	11.5	12
2,3-Dimethylhexane and 2-methyl-3-ethylpentane concentrate (part *A*, fig. 12).	1A	150	175/1	1.7	Azeotropic	Methanol, 600 ml	112	11.8	13
2,3-Dimethylhexane and 2-methyl-3-ethylpentane concentrate (part *B*, fig. 12).	1A	150	175/1	1.7	do	Methyl Cellosolve, 400 ml	217	10.7	14

[a] For further details see reference [6].

tane [3] at 109.28° C, 2,4-dimethylhexane at 109.43° C, 2,2,3-trimethylpentane at 109.84° C, and 1,*trans*-2-*cis*-3-trimethylcyclopentane at 110.4° C.

Following the processing shown in figure 1, 1,*trans*-2,*cis*-3-trimethylcyclopentane was separated using azeotropic distillation with ethanol followed by a regular distillation. The results are shown in figures 2 and 3. In the azeotropic distillation, the ethanol which comprised about 53 percent by volume of the distillate, was extracted from the hydrocarbon portion of the distillate by three cold water extractions in a separatory funnel. A similar procedure was used for the removal of methyl Cellosolve, which comprised about 24 percent by volume of the distillate. The "best lot" of 1,*trans*-2,*cis*-3-trimethylcyclopentane selected from the final distillate (shown in fig. 3) had the following properties: boiling point at 760 mm Hg, 110.4 ±0.1 deg C; refractive index, n_D at 25° C, 1.4112; freezing point in air at 1 atmosphere, −113.08 ±0.02 deg C; amount of the main component, 98.60 ±0.15 mole percent.[4] The best lots of the hydrocarbons reported throughout this investigation were selected on the basis of the refractive index and the boiling point.

Following the distillations shown in figures 2 and 3, the part marked *A* in the figures was reprocessed by four azeotropic distillations, three with methyl Cellosolve (ethylene glycol mono-

[3] See reference [15] for nomenclature of substituted cycloparaffins.

[4] Determined by N. C. Krouskop as described in reference [17], using the cryoscopic constants given in reference [18].

ethyl ether) and one with ethanol to fractionate the material into concentrates of: (a) 2,5- and 2,4-dimethylhexane; (b) 1,*trans*-2,*cis*-4-trimethylcyclopentane; and (c) 1,*trans*-2,*cis*-3-trimethylcyclopentane. The first two concentrates were processed further by azeotropic distillation with ethanol to produce higher concentrations of 1,*trans*-2,*cis*-4-trimethylcyclopentane, 2,5-dimethylhexane, and 2,4-dimethylhexane. The results of these distillations are shown in figures 5, and 6. The concentration of 2,5-dimethylhexane, 2,4-dimethylhexane, 2,2,3-trimethylpentane, and 1,*trans*-2,*cis*-4-trimethylcyclopentane in selected fractions of the distillate was determined by spectrographic infrared absorption measurements made by the Socony-Vacuum Laboratories, Paulsboro, N. J. The results are given in table 2. The fractions containing the highest concentration had the following amounts of the named component in mole percent: 2,5-dimethylhexane, 55 ±5; 2,4-dimethylhexane, 41 ±4; 2,2,3-trimethylpentane, 1.0 ±0.5; 1,*trans*-2,*cis*-4-trimethylcyclopentane, 84 ±5.

The following conclusions may be drawn from the results of the processing of the material normally boiling in the range 108° to 111° C: (a) The first azeotropic distillation (fig. 2) following the regular distillation (part *A* of fig. 1) produced an appreciable enhancement in the separation, as shown in figure 7; (b) ethanol was more effective than methyl Cellosolve in separating azeotropically the two dimethylhexanes from 1,*trans*-2,*cis*-4-trimethylcyclopentane, as shown in figure 8; whereas methyl Cellosolve was more effective than ethanol in separating the two trimethylcyclopentanes, one from the other, as shown in figure 8; (c) 1,*trans*-2,*cis*-3-trimethylcyclopentane is readily separated from the mixture of the five hydrocarbons by a combination of regular and azeotropic distillation, whereas 1,*trans*-2,*cis*-4-trimethylcyclopentane is much less readily separated by the same processes, requiring more distillation; (d) the two dimethylhexanes are only partially separated from each other and from 1,*trans*-2,*cis*-4-trimethylcyclopentane by regular and azeotropic distillation.

2. Material Normally Boiling from 111° to 114° C

The material normally boiling from 111° to 114° C was separated by distillation and found

TABLE 2. *Results of the spectrographic infrared absorption measurements,[a] of selected samples from the 108° to 116° C aromatic-free fraction of Ponca, Okla., petroleum*

Identification of Sample	2,2-Dimethylhexane	2,5-Dimethylhexane	1, *trans*-2, *cis*-4-Trimethylcyclopentane	2,4-Dimethylhexane	2,2,3-Trimethylpentane	1, *trans*-2,*cis*-3-Trimethylcyclopentane	3,3-Dimethylhexane	2,3,4-Trimethylpentane	1,1,2-Trimethylcyclopentane	2,3,3-Trimethylpentane	2,3-Dimethylhexane	2-Methyl-3-ethylpentane	Unknown
	PERCENTAGE BY WEIGHT IN THE SAMPLE												
Part *C*; figure 2	21 ±2	35 ±3	28 ±5	16 ±2	.....	.....							
1,*trans*-2, *cis*-4-Trimethylcyclopentane; figure 4.	.....	1 ±0.5	84 ±5	6 ±2	0.5 ±0.3	6 ±2							2.5 ±1.0
2,5-Dimethylhexane; figure 5.	2 ±1	55 ±5	21 ±2	22 ±2	.....	.....							.....
Part *A*; figure 5	.....	20 ±2	47 ±5	32 ±3	1.0 ±0.5	.....							.....
Part *A*; figure 6	.....	18 ±2	40 ±4	41 ±4	1.0 ±.5	.....							.....
Part *B*; figure 6	.....	29 ±3	35 ±4	35 ±4	1.0 ±.5	.....							.....
3,4-Dimethylhexane; figure 9.	.....	.....	.....	.....	.....	10 ±2	86 ±5	.....	1.0 ±0.5	.....	.....	.....	3 ±1
Part *C*; figure 9	.....	.....	.....	.....	.....	11 ±2	79 ±5	.....	2 ±1	.....	.....	.....	8 ±2
Part *A*; figure 11	.....	.....	.....	.....	.....	.....	31 ±3	17 ±2	52 ±4	.....	--	.....	.....
Part *B*; figure 11	.....	.....	.....	.....	.....	.....	16 ±2	17 ±2	67 ±5	.....	.....	.....	.....
Part *A*; figure 13	.....	.....	.....	.....	.....	.....	.....	5 ±2	63 ±5	10 ±2	12 ±2	10 ±2	.....
Part *B*; figure 13	.....	.....	.....	.....	.....	.....	.....	.....	19 ±2	4 ±2	47 ±5	30 ±3	.....
Part *D*; figure 13	.....	.....	.....	.....	.....	.....	.....	.....	.....	.....	66 ±5	34 ±3	.....
Part *B*; figure 14	.....	.....	.....	.....	.....	.....	.....	.....	.....	.....	60 ±5	40 ±5	.....
Original of experiment No. 4; figure 15.	.....	.....	.....	.....	.....	.....	.....	.....	.....	.....	54.5 ±5.0	45.5 ±5.0	.....
Part *B* of experiment No. 4; figure 15.	.....	.....	.....	.....	.....	.....	.....	.....	4 ±2	3 ±1	48 ±5	45 ±5	.....

[a] Made by the Socony-Vacuum Laboratories, Paulsboro, N. J. A description of the apparatus is given in reference [3].

to be composed of three compounds, 3,3-dimethylhexane at 111.97° C, 2,3,4-trimethylpentane at 113.47° C, and 1,1,2-trimethylcyclopentane at 113.72° C.

Following the distillation shown in figure 1, the parts marked *B* and *C* in that figure were processed to separate 3,3-dimethylhexane and 1,1,2-trimethylcyclopentane. 3,3-Dimethylhexane was separated by azeotropic distillation with methyl Cellosolve as shown in figure 9, and 1,1,2-trimethylcyclopentane was separated by regular distillation followed by azeotropic distillation with methyl Cellosolve as shown in figures 10 and 11, respectively. The concentration of 3,3-dimethylhexane and 2,3,4-trimethylpentane in selected fractions of the distillate was determined by spectrographic infrared absorption measurements made by the Socony-Vacuum Laboratories. The results are given in table 2. The fractions containing the highest concentration had the following amounts of the named component in mole percent: 3,3-dimethylhexane, 86 ±5; 2,3,4-trimethylpentane, 17 ±2. The "best lot" of 1,1,2-trimethylcyclopentane selected from the final distillate shown in figure 11 had the following properties: Boiling point at 760 mm Hg, 113.7 ±0.1° C; refractive index, n_D, at 25° C, 1.4192; freezing point in air at 1 atmosphere, −30.21 ±0.05° C; amount of the main component, 97.50 ±0.06 mole percent (see footnote 4).

From the results of the processing of the material normally boiling in the range 111° to 114° C, it can be concluded that 3,3-dimethylhexane and 1,1,2-trimethylcyclopentane are both readily separable from this fraction of the Ponca, Okla., petroleum by high efficiency distillation.

3. Material Normally Boiling from 114° to 116° C

The material normally boiling from 114° to 116° C was processed by distillation, supplemented by adsorption, and was found to be composed of three compounds, 2,3,3-trimethylpentane at 114.76° C, 2,3-dimethylhexane at 115.61° C, and 2-methyl-3-ethylpentane at 115.65° C.

Following the distillation shown in figure 1, the portion of this distillate (part *D*) containing the concentrate of the above three hydrocarbons was distilled regularly, followed by azeotropic distillation with methanol and methyl Cellosolve as shown in figures 12, 13, and 14, respectively. Distillate from the above azeotropic distillations, containing mainly a mixture of 2,3-dimethylhexane and 2-methyl-3-ethylpentane, was processed further by adsorption [5] [16, 19] through glass columns (790 cm in length and 1 cm in diameter) with silica gel [6] as the adsorbent and ethanol as the desorbing liquid. The results of the separation of 2-methyl-3-ethylpentane from 2,3-dimethylhexane by adsorption are given in figure 15. The charges for these separations by adsorption were as follows: 1, part *A* of figure 14; 2, part *B* of 1 above; 3, part *C* of figure 13 and part B of figure 14; and 4, part *A* from 1, part *A* from 2, and part *B* from 3 above. The "best lot" from petroleum of the two paraffins was selected from the adsorption separations shown in figure 15 as follows: 2-methyl-3-ethylpentane, part *B* from experiment 4; 2,3-dimethylhexane, parts *C*, *C*, and *D* from experiments 1, 2, and 3, respectively.

The concentration of 2,3,3-trimethylpentane, 2,3-dimethylhexane, and 2-methyl-3-ethylpentane in selected fractions of the distillate and the filtrate from the adsorptions was determined by spectrographic infrared absorption measurements made by the Socony-Vacuum Laboratories. The results are given in table 2. The fractions containing the highest concentration had the following amounts of the named component in mole percent: 2,3,3-trimethylpentane, 10 ±2; 2,3-dimethylhexane, 66 ±5; 2-methyl-3-ethylpentane, 45 ±5.

The following conclusions may be drawn from the results of the processing of the material normally boiling in the range 114° to 116° C: (a) Regular and azeotropic distillation produced essentially a binary mixture of the two close-boiling paraffins, 2,3-dimethylhexane and 2-methyl-3-ethylpentane; (b) fractionation by adsorption resulted in a further slight separation of these two paraffins and a further separation of the small amount of 1,1,2-trimethylcyclopentane associated with them.

IV. Amounts of the Components in Petroleum

The calculation of the amounts by volume of the 11 compounds in the aromatic-free fraction of petroleum normally boiling between 108° and 116° C was made by appropriate reduction, as

[5] Performed under the supervision of B. J. Mair, in charge of Fractionation and Analysis, Section on Thermochemistry and Hydrocarbons.

[6] Silica gel No. 22-08, Davison Chemical Company, Baltimore, Md.

scribed in reference [13], of the data on boiling oint and refractive index as a function of the olume of distillate, as shown in figure 1, supple-ented by the results of the spectrographic in-ared absorption measurements on selected frac-ons as listed in table 2. The spectrographic ata served to establish the relative amounts of ,5-dimethylhexane and 2,4-dimethylhexane, of ,3-dimethylhexane and 2-methyl-3-ethylpentane, nd of the three trimethylpentanes. The data on oiling point and refractive index as a function of he volume of distillate were utilized to the fullest xtent of their precision by plotting the data on xpanded scales of temperature, refractive index, nd volume.

The relative amounts by volume in the aro-atic-free fraction 108° to 116° C of the Ponca, kla., petroleum was translated into amounts ased on the original crude petroleum using un-ublished data (percentage of total crude this raction comprised) obtained in the investigation f the American Petroleum Institute Research roject 6 on the gasoline fraction of seven repre-entative crudes, which includes the Ponca, Okla., etroleum [8, 9, 14]. Table 3 gives these amounts, ogether with the amount of toluene [9], in the riginal crude petroleum.

TABLE 3. *Amounts of the 12 hydrocarbons constituting the 108° to 116° C fraction of the petroleum*

Component	Boiling point at 1 atm[a]	Relative amount by volume in the aromatic-free portion	Amount in the original crude petroleum[b]
	°C		*Percentage by volume*
2,5-Dimethylhexane	109.11	7.	0.055
1,*trans*-2,*cis*-4-Trimethylcyclopentane	109.28	28.	.22
2,4-Dimethylhexane	109.43	7	.055
2,2,3-Trimethylpentane	109.84	0.5	.004
1,*trans*-2,*cis*-3-Trimethylcyclopentane	110.4	33.	.26
Toluene	110.62		[c] .51
3,3-Dimethylhexane	111.97	3	.03
2,3,4-Trimethylpentane	113.47	0.6	.005
1,1,2-Trimethylcyclopentane	113.72	7.	.06
2,2,3-Trimethylpentane	114.76	0.8	.006
2,3-Dimethylhexane	115.61	8.	.06
2-Methyl-3-ethylpentane	115.65	5.	.04
Total		100.	1.30

[a] From reference [7].
[b] For each component, the percentage by volume of the gasoline fraction, 0° to 180° C, is about 3 times the value in this column.
[c] From reference [9].

From the data given in table 3, the following points may be made regarding the composition with respect to volume of the 108° to 116° C fraction of petroleum:

(a) The material is comprised entirely of three types of hydrocarbons with the following relative amounts: isoparaffins, 20; cyclopentanes, 41; and an alkyl benzene, 39.

(b) The isoparaffins with dialkyl and trialkyl substituents are present in the relative amounts of 15 and 1, respectively.

(c) The relative amounts of the isoparaffins and the alkyl cyclopentanes are approximately 1 and 2, respectively.

(d) The alkyl benzene, toluene, constitutes about two-fifths of the entire fraction 108° to 116° C.

(e) Two of the alkyl cyclopentanes (1,*trans*-2, *cis*-4-trimethylcyclopentane and 1,*trans*-2, *cis*-3-trimethylcyclopentane) together constitute about 60 percent of the aromatic-free fraction 108° to 116° C.

Acknowledgment is made to F. P. Hochgesang, Socony-Vacuum Laboratories, Paulsboro, N. J., for the spectrographic infrared absorption measurements reported in table 2 of this paper.

V. References

[1] F. D. Rossini, Petroleum Engr. **14,** 223 (1943).
[2] F. D. Rossini, Anal. Chem. **20,** 110 (1948).
[3] American Petroleum Institute Research Project 44, National Bureau of Standards. Catalog of selected infrared spectral data. Description of infrared spectrographs No. 5, contributed by the Socony Vacuum Laboratories.
[4] A. R. Glasgow, Jr., C. B. Willingham, and F. D. Rossini, J. Research NBS **38,** 621 (1947) RP1800.
[5] R. T. Leslie, J. Research NBS **22,** 153 (1939) RP1174.
[6] C. B. Willingham and F. D. Rossini, J. Research NBS **37,** 15 (1946) RP1724.
[7] American Petroleum Institute Research Project 44, National Bureau of Standards. Selected Values of Properties of Hydrocarbons. Table No. 3a, 5a, and 15a, tables on boiling point, *dt/dp*, refractive index, density, and freezing points (June 30, 1945, May 31, 1947, and February 28, 1947).
[8] F. D. Rossini, B. J. Mair, A. F. Forziati, A. R. Glasgow, Jr., and C. B. Willingham, Proc. Am. Petroleum Inst. **23,** (III) (1942); Oil Gas J. **41,** 106 (1942); Petroleum Refiner **21,** 73 (1942).
[9] A. F. Forziati, C. B. Willingham, B. J. Mair, and F. D. Rossini, J. Research NBS **32,** 12 (1944), RP1571; Proc. Am. Petroleum Inst. **24,** (III) 34 (1943).

[10] F. D. Rossini, Proc. Am. Petroleum Inst. **18,** (III) 36 (1937); Oil Gas J. **36,** 193 (1937); Refiner Natura Gasoline Mfg. **16,** 545 (1937).

[11] M. M. Hicks-Bruun and J. H. Bruun, BS J. Research **8,** 525 (1932) RP432.

[12] J. H. Bruun, R. T. Leslie, and S. T. Schicktanz, BS J. Research **6,** 363 (1931) RP280.

[13] A. R. Glasgow, Jr., A. J. Streiff, C. B. Willingham, and F. D. Rossini, Proc. Am. Petroleum Inst. **26,** (III) 127 (1946). J. Research NBS **38,** 537 (1947) RP1795.

[14] A. F. Forziati and F. D. Rossini, J. Research NBS **43,** 473 (1949) RP2038

[15] M. B. Epstein and F. D. Rossini, American Petroleum Institute Research Project 44, Natio Bureau of Standards. "Naming of Geome Isomers of Polyalkyl Monocycloalkanes".

[16] B. J. Mair, A. L. Gaboriault, and F. D. Rossini, I Eng. Chem. **39,** 1072 (1947).

[17] A. R. Glasgow, Jr., A. J. Streiff, and F. D. Rossini Research NBS **35,** 355 (1945) RP1676.

[18] A. J. Streiff, E. T. Murphy, J. C. Cahill, H. Flanagan, V. A. Sedlak, C. B. Willingham, a F. D. Rossini, J. Research NBS **38,** 53 (19 RP1760.

[19] B. J. Mair, A. J. Sweetman, and F. D. Rossini, I Eng. Chem. **41,** 2224 (1949).

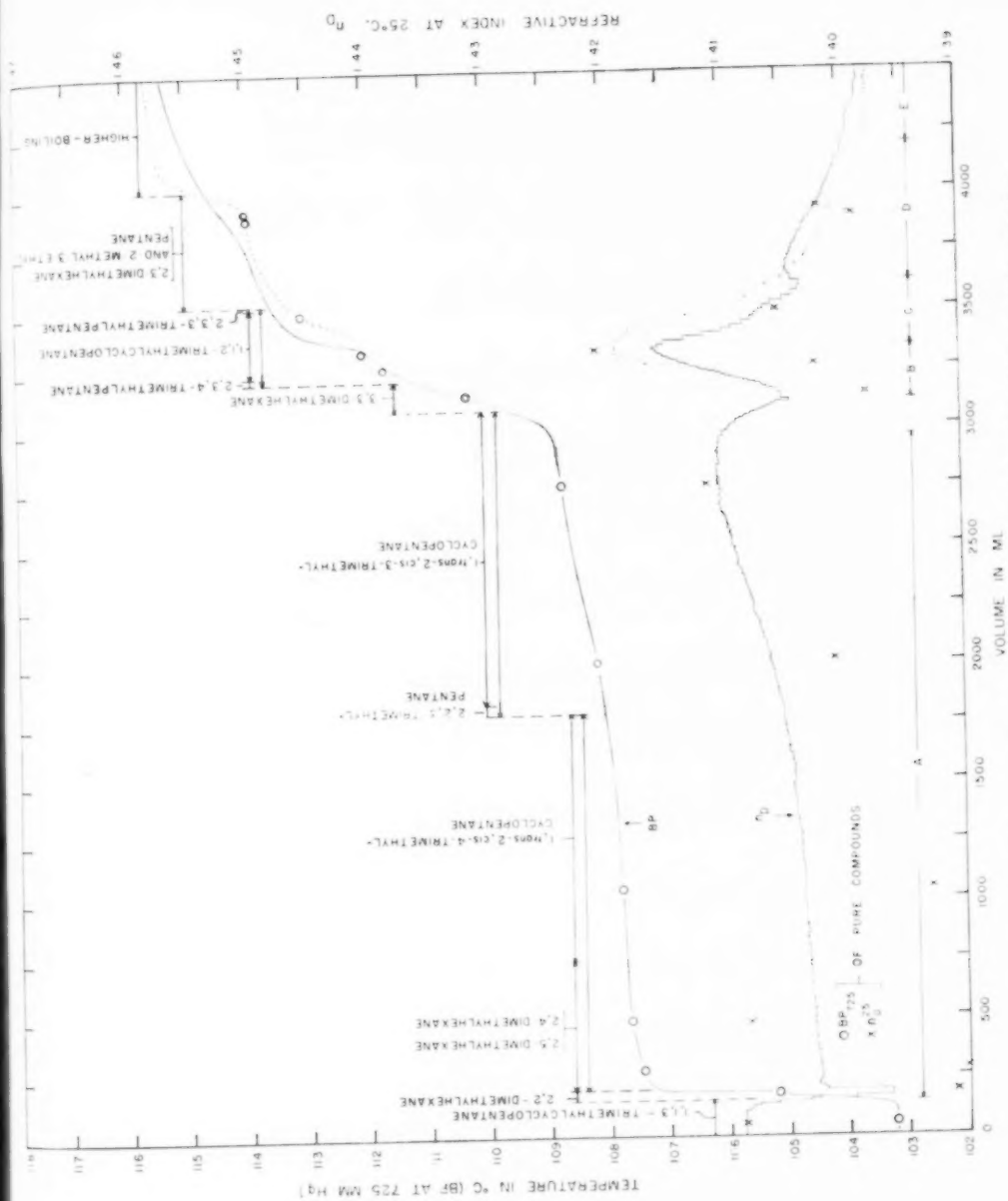

FIGURE 1. *Distillation of the 105° to 116° C (aromatic-free) fraction of Powra, Okla., petroleum.*

The relative amounts by volume of the various components are indicated in the upper portion of the figure. The dashed curves for the boiling point and the refractive index are those obtained after redistillation of this portion of the distillate. The portions A to E, enclosed with arrows, were redistilled.

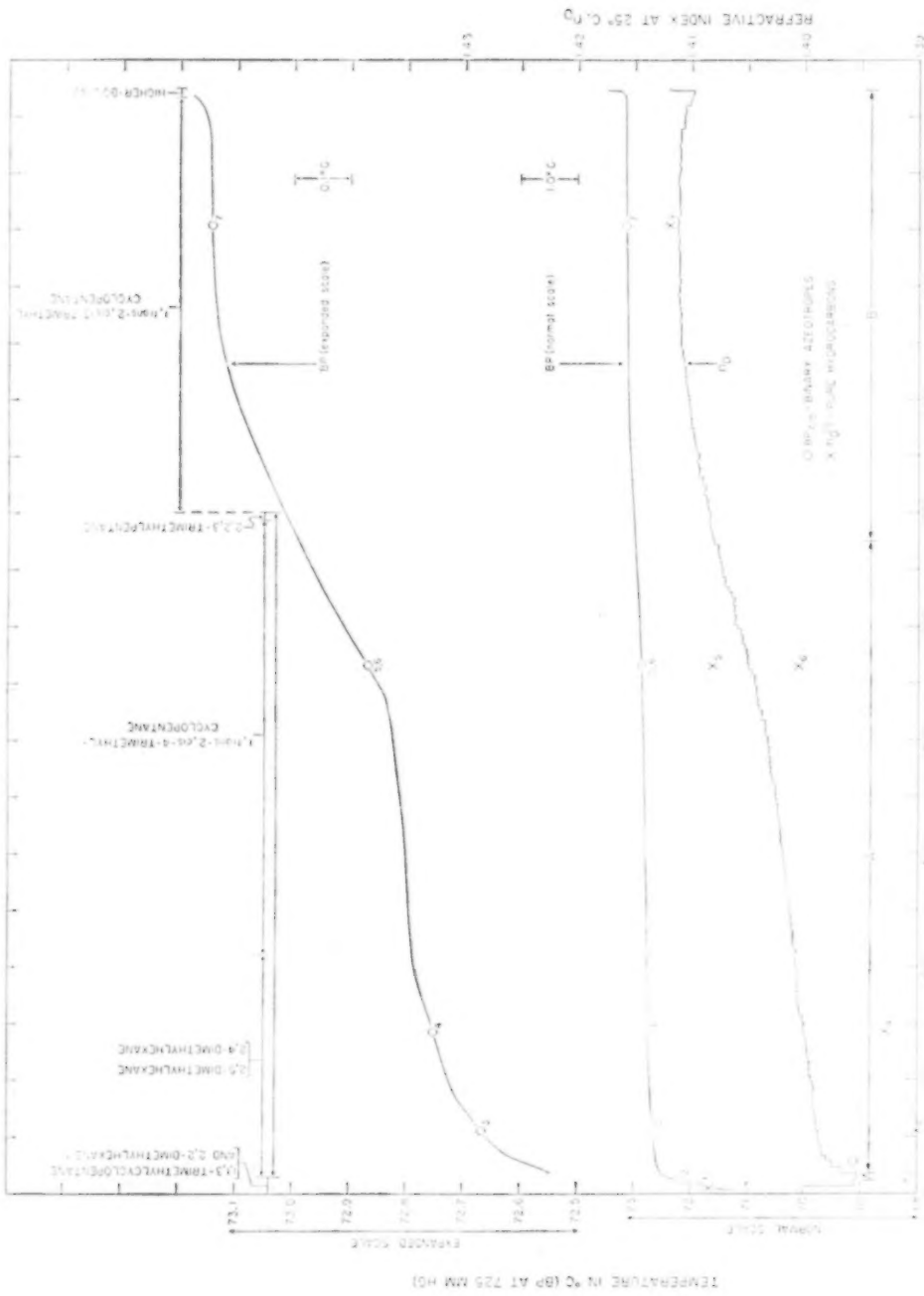

FIGURE 2. *Distillation of the 108° to 111° C (aromatic-free) portion (part A, fig. 1).*

The ordinate scale on the right gives the refractive indices of the hydro carbon portion of the azeotropic distillate. The scale of ordinates on the left gives a normal and an expanded scale of boiling point for the azeotropic distillate. The scale of abscissas gives the volume of the hydrocarbon portion of the distillate. The relative amounts by volume of the various components are indicated in the upper portion of the figure. The portions A and B, enclosed with arrows, were redistilled. The fraction marked C was analyzed by spectrographic infrared-absorption measurements. The numbers accompanying the circles, which indicate the azeotrope boiling point of the pure hydrocarbon with ethanol, refer to the following: (1) to 2,2-dimethylhexane; (2) to 1,1,3-trimethylcyclopentane; (3) to 2,4-dimethylhexane; (4) to 2,3,4-trimethylpentane; (5) to 2,3-dimethylhexane; (6) to 2,5-dimethylhexane; (7) to 2,4-dimethylheptane; (8) to 2,2,3-trimethylpentane; (9) to 2,3,4-trimethylpentane; (10) to 2,3-dimethylheptane; (11) to 4-methyloctane; (12) to 2-methyloctane; (13) to 3-ethyloctane; (14) to 2,6-dimethylheptane; (15) to 2,4,6-trimethylheptane; (16) to 2,2,5-trimethylhexane; (17) to 2,2,4-trimethylhexane; (18) to 2,2,3,3-tetramethylpentane; (19) to 2,2,3,4-tetramethylpentane.

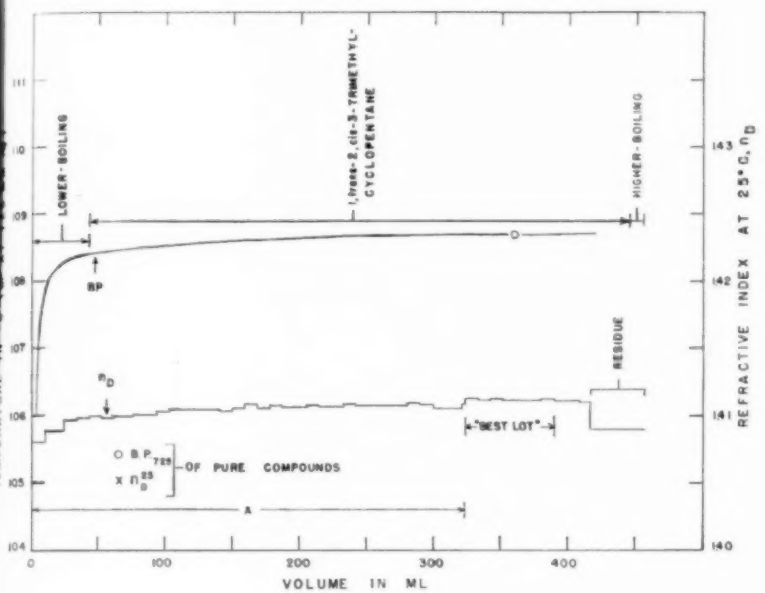

FIGURE 3. *Distillation of the 1,trans-2,cis-3-trimethlylcyclopentane concentrate (part B, fig. 2).*

The relative amounts by volume of the various components are indicated in the upper portion of the figure. The portion A, enclosed with arrows, was redistilled.

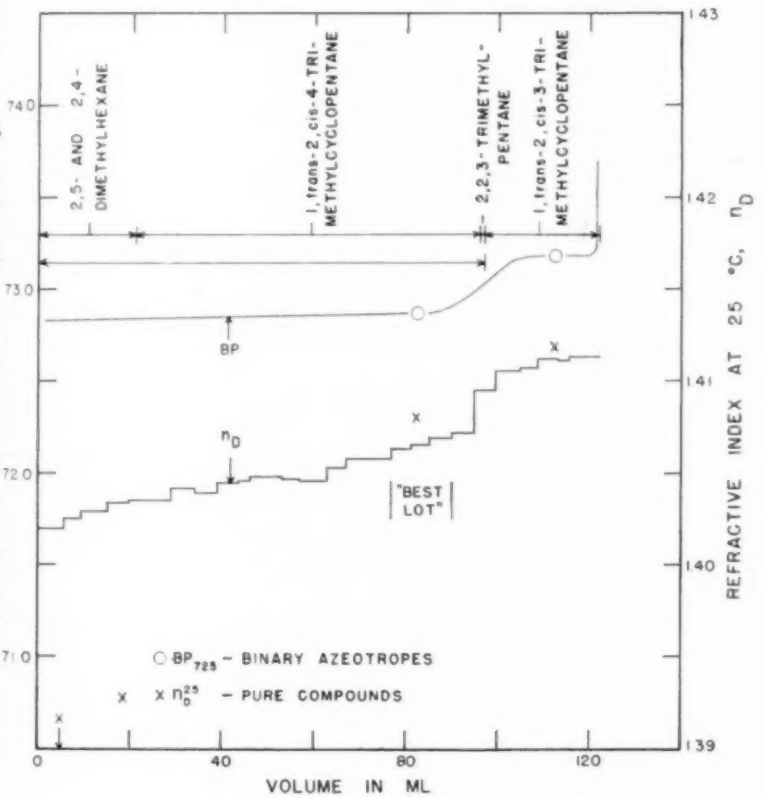

FIGURE 4. *Distillation of the concentrate of 1,trans-2,cis-4-trimethylcyclopentane (derived from part A, fig. 1).*

The ordinate scale on the right gives the refractive indices of the hodrocarbon portion of the azeotropic distillate, and the ordinate scale on the left gives the boiling point of the azeotropic distillate. The scale of abscissas gives the volume of the hydrocarbon portion of the distillate.

The relative amounts by volume of the various components are indicated in the upper portion of the figure. The portion labeled "best lot" was analyzed by spectrographic infrared absorption measurements, the results of which are shown in table 2.

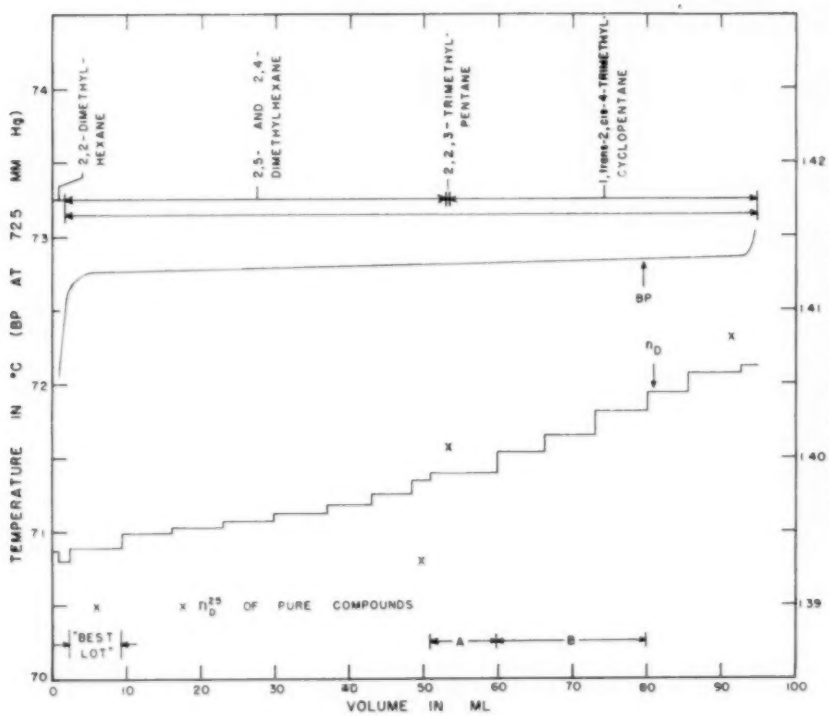

FIGURE 5. *Distillation of the 2,5-dimethylhexane concentrate (derived from part A, fig. 1).*

The ordinate scale on the right gives the refractive indices of the hydrocarbon portion of the azeotropic distillate, and the ordinate scale on the left gives the boiling point of the azeotropic distillate. The scale of abscissas gives the volume of the hydrocarbon portion of the distillate. The relative amounts by volume of the various components are indicated in the upper portion of the figure. The portions A and B, enclosed with arrows, were redistilled. The portion labeled "best lot" was analyzed by spectrographic infrared absorption measurements, the results of which are shown in table 2.

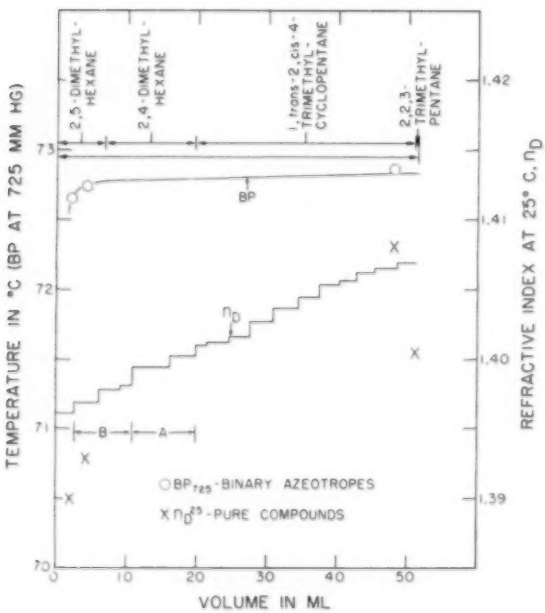

FIGURE 6. *Distillation of the 2,4-dimethylhexane concentrate (derived from part A, fig. 1).*

The ordinate scale on the right gives the refractive indices of the hydrocarbon portion of the azeotropic distillate and the ordinate scale on the left gives the boiling point of the azeotropic distillate. The scale of abscissas gives the volume of the hydrocarbon portion of the distillate. The relative amounts by volume of the various components are indicated in the upper portion of the figure. The portions A and B, enclosed by arrows, were analyzed by spectrographic infrared absorption measurements, the results of which are shown in table 2.

FIGURE 7. *Comparison of separation of 108° to 111° C material by regular and azeotropic distillation with ethanol.*

The outer ordinate scale on the right gives the refractive indices of the hydrocarbon portion of the azeotropic distillate, and the refractive index of the distillate from the regular distillation. The inner ordinate scale on the right gives the boiling point of the distillate from the regular distillation. The scale of abscissas gives the volume of the hydrocarbon portion of the distillate. The numbers accompanying the boiling point and refractive index values shown in the figure refer to the following: (1) to 2,5-dimethylhexane; (2) to 1,*trans*-2,*cis*-4-trimethylcyclopentane; (3) to 2,4-dimethylhexane; (4) to 2,2,3-trimethylpentane; and (5) to 1,*trans*-2,*cis*-3-trimethylcyclopentane. The relative amounts by volume of the various components are indicated in the upper portion of the figure

FIGURE 8. *Comparison of the separation of 108° to 111° C material by azeotropic distillation with ethanol and methyl Cellosolve.*

The outer ordinate scale on the right gives the refractive indices of the hydrocarbon portion of the azeotropic distillate. The scale of abscissas gives the volume of the hydrocarbon portion of the distillate. The numbers accompanying the boiling point and refractive index values shown in the figure refer to the following: (1) to 2,5-dimethylhexane; (2) to 1,*trans*-2,*cis*-4-tri-methylcyclopentane; (3) to 2,4-dimethylhexane; (4) to 2,2,3-trimethylpentane and (5) to 1,*trans*-2,*cis*-3 trimethylcyclopentane. The relative amounts by volume of the various components are indicated in the upper portion of the figure.

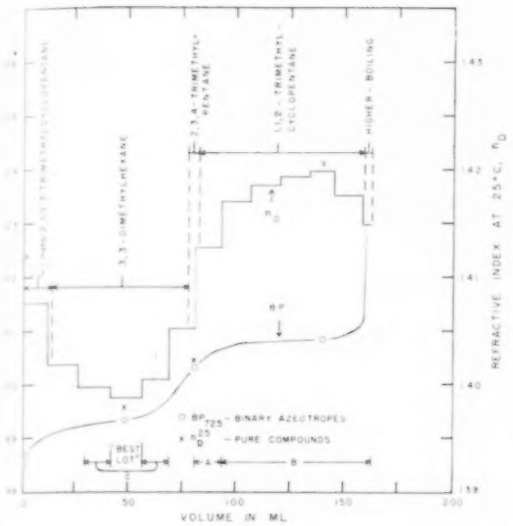

FIGURE 9. *Distillation of the 3,3-dimethylhexane concentrate (part B, fig. 1).*

The ordinate scale on the right gives the refractive indices of the hydrocarbon portion of the azeotropic distillate, and the ordinate scale on the left gives the boiling point of the azeotropic distillate at 725 mm Hg. The scale of abscissas gives the volume of the hydrocarbon portion of the distillate. The relative amounts by volume of the various components are indicated in the upper portion of the figure. The portions A and B, enclosed with arrows, were redistilled. The portions labeled "best lot" and C were analyzed by spectrographic infrared absorption measurements, the results of which are shown in table 2.

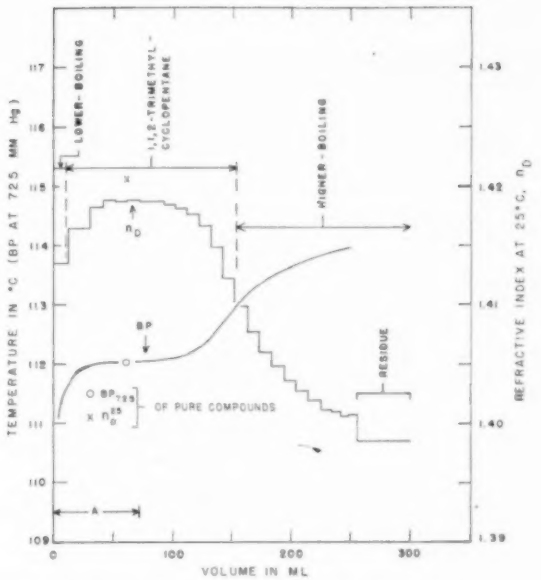

FIGURE 10. *Distillation of the 1,1,2-trimethylcyclopentane concentrate (part C, fig. 1; part B, fig. 9).*

The relative amounts by volume of the various components are indicated in the upper portion of the figure. The portion A, enclosed with arrows, was redistilled.

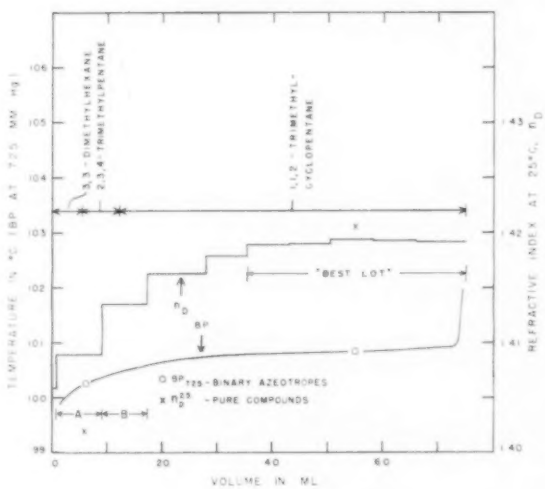

FIGURE 11. *Distillation of the 1,1,2-trimethylcyclopentane concentrate (part A, figs. 9 and 10).*

The ordinate scale on the right gives the refractive indices of the hydro carbon portion of the azeotropic distillate, and the ordinate scale on the left gives the boiling point of the azeotropic distillate. The scale of abscissas gives the volume of the hydrocarbon portion of the distillate. The relative amounts by volume of the various components are indicated in the upper portion of the figure. The lettered fractions A and B were analyzed by spectrographic infrared absorption measurements, the results of which are given in table 2.

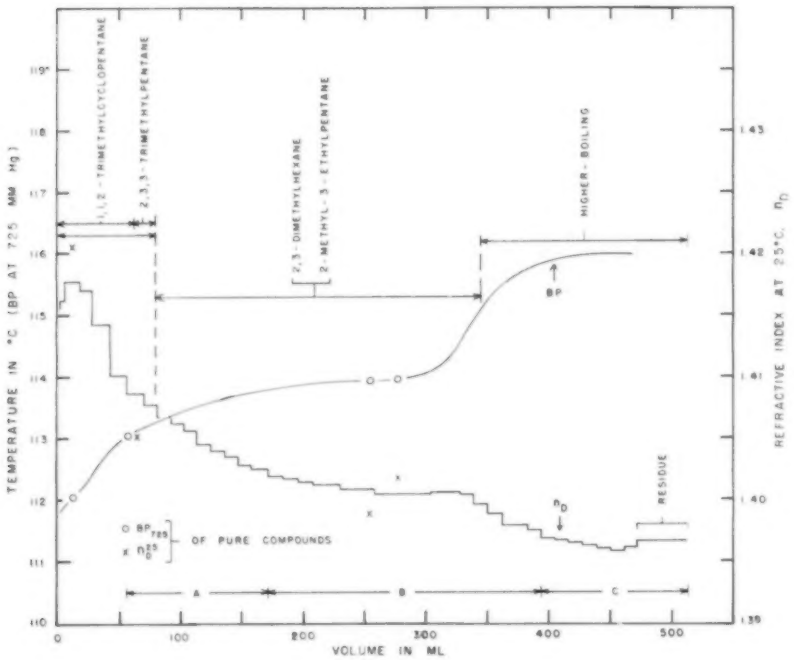

FIGURE 12. *Distillation of the 2,3-dimethylhexane and 2-methyl-3-ethylpentane concentrate (part D, fig. 1).*

The relative amounts by volume of the various components are indicated in the upper portion of the figure. The portions A, B, and C, enclosed with arrows, were redistilled.

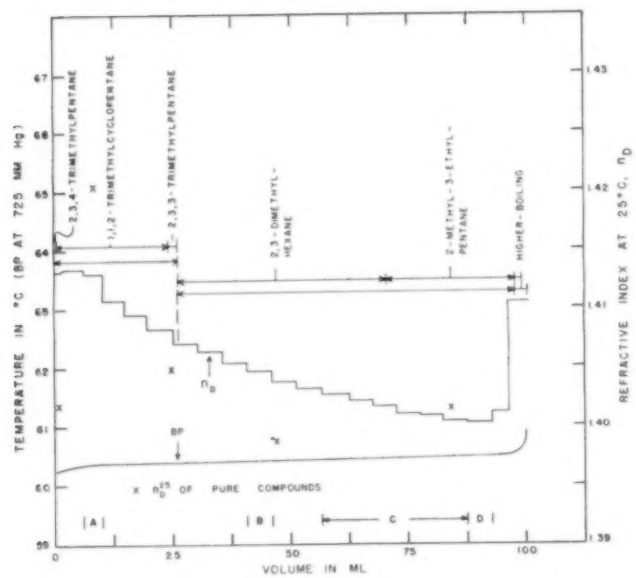

FIGURE 13. *Distillation of the 2,3-dimethylhexane and 2-methyl-3-ethylpentane concentrate (part A, fig. 12).*

The ordinate scale on the right gives the refractive index of the hydrocarbon portion of the azeotropic distillate, and the ordinate scale on the left gives the boiling point of the azeotropic distillate. The scale of abscissas gives the volume of the hydrocarbon portion of the distillate. The relative amounts by volume of the various components are indicated in the upper portion of the figure. The portion C, enclosed with arrows, was reprocessed by adsorption. The lettered fractions A, B, and D were analyzed by spectrographic infrared absorption measurements, the results of which are shown in table 2.

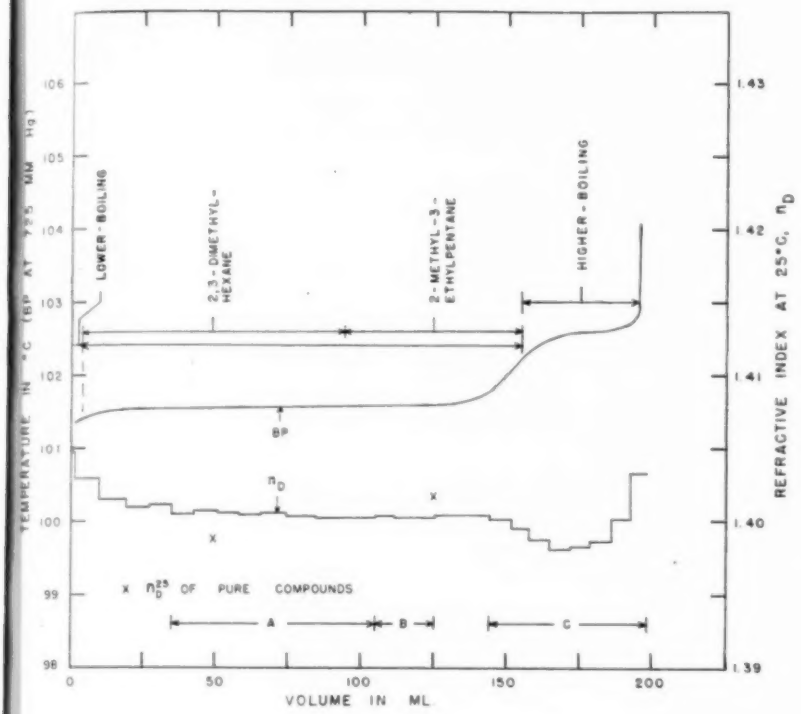

FIGURE 14. *Distillation of the 2,3-dimethylhexane and 2-methyl-3-ethylpentane concentrate (part B, fig. 12).*

The ordinate scale on the right gives the refractive indices of the hydrocarbon portion of the azeotropic distillate, and the ordinate scale on the left gives the boiling point of the azeotropic distillate. The scale of abscissas gives the volume of the hydrocarbon portion of the distillate. The relative amounts by volume of the various components are indicated in the upper portion of the figure. The portions A and B, enclosed with arrows, were processed further by adsorption, the results of which are given in figure 15. Portion A was analyzed by spectrographic infrared absorption measurements the results of which are given in table 2. Portion C was processed with higher-boiling material.

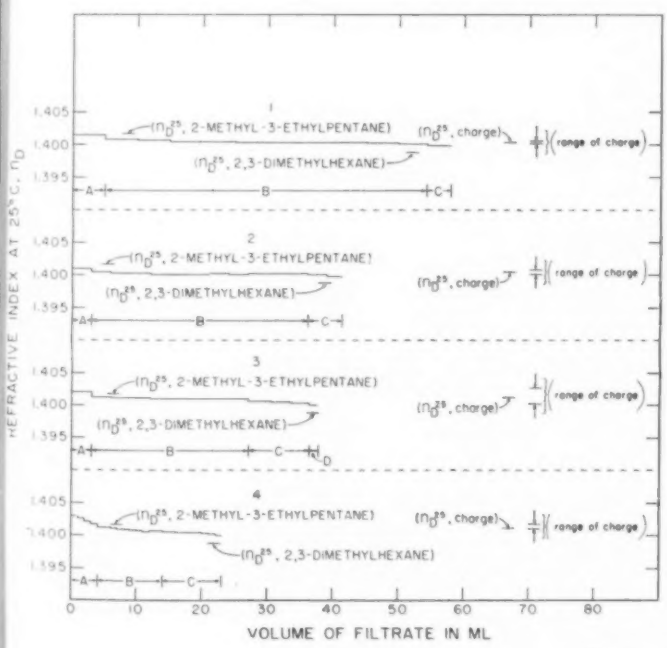

FIGURE 15. *Results of adsorption experiments on 2,3-di-methylhexane and 2-methyl-3-ethylpentane.*

The portions A, B, C, and D, enclosed with arrows, were either reprocessed by adsorption or selected as concentrates of the individual components; see text for further discussion.

WASHINGTON, September 8, 1949.

U. S. Department of Commerce
National Bureau of Standards

Research Paper RP2066
Volume 44, February 1950

Part of the Journal of Research of the National Bureau of Standards

Concrete as a Protective Barrier for Gamma Rays from Cobalt-60

By Robert J. Kennedy, Harold O. Wyckoff, and William A. Snyder

The broad-beam and narrow-beam attenuation of Co^{60} gamma rays has been investigated experimentally, and the data are presented here. In protective barriers the geometry necessarily requires the use of broad-beam attenuation curves to determine the required barrier thickness. This paper presents attenuation curves for lead, concrete, and steel necessary for determining the required protection for any particular cobalt source in storage or transportation. There is also included a table for shielding requirements for Co^{60} sources of 10 millicuries to 2 curies.

I. Introduction[1]

Three distinct processes are effective in the attenuation of gamma rays; photoelectric absorption, Compton absorption and scattering, and pair production. In each of these three modes of interaction of gamma rays with matter, the gamma ray gives up all or part of its initial energy to the atom. Each of these processes gives rise to some secondary photons of energy less than that of the primary photons and in a direction different from that of the primary photon. These secondary radiations are (a) characteristic radiation of photoionization, (b) Compton scattered photons and (c) annihilation radiation in the loss of an electron-positron pair. However, in the energy range under consideration (1.1 and 1.3 Mev) the soft characteristic radiation is readily absorbed, and the annihilation radiation is negligibly small. Therefore, all of the photoelectric, Compton absorption, and pair-production phenomena may be considered as true absorption of photon energy because the probability that secondary electrons will produce "bremsstrahlung" is very small.

As the Compton-scattered photons are always produced during the attenuation of a beam of gamma rays, the geometry of the experimental arrangement for measuring attenuation may be very important. The geometry can be classified as narrow beam,[2] or good geometry; and broad beam (see footnote 2) or bad geometry. The narrow-beam attenuation is obtained under conditions in which only a negligible amount of the scattered radiation is measured by the chamber. Under experimental conditions, this amounts to having the irradiated area of the absorber subtend a small solid angle at the chamber as well as the source. This condition can be verified experimentally by a check on the inverse square law for the radiation received by the chamber. If the inverse square relation is found to hold, the scattered radiation from the barrier is negligible. If, however, the chamber is situated near the emergent side of the absorber and the irradiated area is large compared to the dimensions of the chamber, or if the barrier is very near to the source there will be an appreciable portion of the chamber ionization produced by the secondary radiation from the absorber and a broad-beam condition will exist. For this condition the attenuation curve is unique only for that particular barrier-to-chamber distance and barrier-to-source distance.

The ionization measured by the chamber may be thought of as being due to radiation from two different sources; (A) that part of the radiation that comes directly from the source as primary radiation, (B) the remainder that comes from the entire irradiated volume of the absorber as secondary radiation. Several factors serve to limit the effective volume, which acts as a secondary source. The path length of the incident plus the scattered-photon in the absorber will be greater

[1] The work described here was supported in part by the Atomic Energy Commission.

[2] H. O. Wyckoff, R. J. Kennedy, and W. R. Bradford, J. Research NBS 41, 223 (1948) RP1920.

for oblique rays and, therefore, such photons have a greater probability of being absorbed. In addition the angle between the incident and the scattered photon must be greater for oblique rays and hence the photon energy smaller. This latter factor also increases the probabilityof true absorption of the photon.

The increase in dosage rate of the broad beam over the narrow beam is due to the large amount of scattered radiation in the attenuated broad beam and to the increased spectral sensitivity of the ion chamber for the very low energy scattered radiation. As the absorber thickness is increased from zero, there is at first an over-all increase in the ratio of the number of emergent secondary photons to the emergent primary photons. The secondary photons originate mainly through Compton scattering, and their energy is dependent on the angles through which they have been scattered. Another possible phenomenon that would increase the dosage rate when scattered radiation is measured was recently discussed by Failla.[3] He pointed out that the ionization produced in the chamber is proportional to the photon energy and the absorption coefficient in air, and that the absorption coefficient increases very rapidly as the photon energy is decreased below 70 Kev. The Compton photons having energy below this value may produce a greater effect in the chamber than the primary photon. Such scattered photons would, however, have to be of an energy below 30 Kev in order to produce such an effect for million-volt primary radiation.

These softer scattered secondaries are more readily attenuated by the absorber than the primary radiation, and eventually an absorber thickness is reached at which the production of new secondaries is just balanced by their absorption in the added thickness. This effect is observed as a slight increase in dosage rate for thin absorbers and the divergence of the narrow- and broad-beam attenuation curves. The attenuation curves will be concave downward for small absorber thicknesses and are expected to become parallel to the narrow-beam curves for very large thicknesses of absorber. The range of shielding thicknesses studied here was not sufficient to obtain this equilibrium condition. The above effect is seen to be much less for lead than for lighter materials such as concrete and steel, due to the difference in the photoelectric absorption of the secondary photons in these materials.

[3] G. Failla, Am. J. Roentgenol. Radium Therapy **54**, 553 (1945).

II. Description of Apparatus

Figure 1 shows the experimental arrangement. The measuring device used in this work was a cylindrical ionization chamber with ⅛ in. thick Bakelite walls, approximately 10 cm in diameter

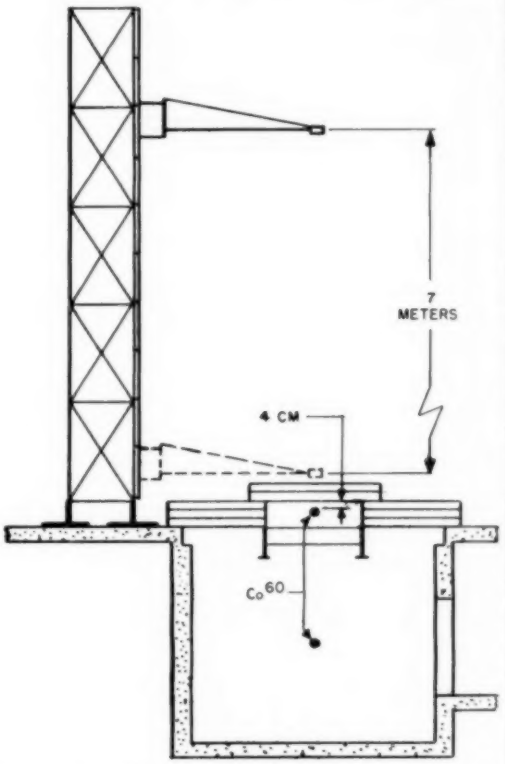

FIGURE 1. *Experimental arrangement for broad-beam attenuation measurements of gamma rays from* Co^{60}.

and 10 cm in length containing 824 ± 2 cc of free air. The collecting potential was 400 v, which was well above that required for saturation. The chamber was attached to one end of a 10-ft duralumin tube, the other end being connected to a brass cylinder housing the split FP–54 electrometer tube and a selection of S. S. White grid resistors ranging from 10^8 to 10^{11} ohms.

The electrometer tube housing was supported on a movable carriage that could travel in elevation through a distance of 7 m. The duralumin

tube could also be rotated about a vertical axis through the carriage through 120°. The elevation and azimuth motions were controlled by remote switching. A pair of selsyns indicated the position of the chamber. As a check on the positioning of the chamber, a cathetometer was used over the first meter of elevation. Its reading showed a consistent repetition of the elevation within 3 or 4 mm of the position indicated by the selsyns.

The source of radiation was a cylinder of solid cobalt-60, 1 cm in diameter and 1½ cm in length

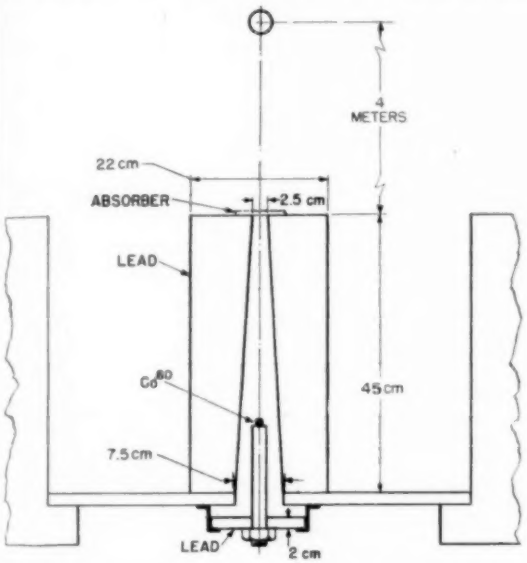

FIGURE 2.—*Experimental arrangement for narrow-beam attenuation measurements.*

with an apparent activity of approximately 1.75 curies. It was enclosed in a capsule of duralumin 1 mm thick for convenience in handling and as a protection against possible contamination of the building. The source was then placed on a supporting rod that could be moved over a range of 4-m elevation in a pit 16 by 16 by 14 ft deep. The pit was covered with 18 in. of concrete except for a center opening 6 by 6 ft. This opening was further reduced to 4 by 4 ft by placing ¼ in. of lead over the outer edge of the pit.

In the narrow-beam attenuation determination, figure 2, a lead shield 22 cm in diameter and 45 cm long, with a conically shaped center hole converging from 7.5 to 2.5 cm in diameter, was used to diaphragm the radiation. This shield was placed vertically in the center of the pit opening so that the absorbers could be placed directly on top of the limiting aperture. The irradiated area of the absorber was 2.5 cm in diameter. The lead, copper, and tin absorbers used here were 15 cm square and 2 to 10 mm thick. The concrete absorbers were 4- and 6-in. diameter cylinders 4 to 8 in. long with a density of 2.35 g/cm^3. The steel absorbers were 30 cm square and 1.27 cm thick.

A separate experiment, based on the inverse square criterion mentioned above, was designed to prove that this arrangement provided narrow-beam attenuation data. The chamber was placed axially 2 m from the absorber, and the distance from the source of the limiting aperture varied within the shield. Moving the source over the range of 10 to 37 cm from the limiting aperture showed no change in the dosage rate at the chamber that could not be accounted for by the inverse square law. The cobalt was then placed at a fixed distance of 26 cm from the limiting aperture, and the chamber-to-source distance was varied through a range of 0.4 to 7 m. Over the range of 1.5 to 7 m, there was no appreciable change in the dosage rate at the chamber other than the inverse square variation. With the chamber fixed at 4 m from the limiting aperture the above results indicated, therefore, that the amount of scattered radiation measured by the chamber was negligible and that the narrow-beam condition existed.

For the broad-beam measurements the source was undiaphragmed and placed at a distance of 4 or 210 cm from the bottom of the absorbers. The concrete absorbers were blocks 8 ft by 8 ft by 6 in. thick weighing approximately 2.5 tons each. The steel absorbers were sheets 8 by 8 ft with thicknesses of ⅛, ⅜, and ½ in. The lead absorbers were 2 ft by 8 ft by ⅛ in. thick and overlapped ¼ in. at the joints. No joint was closer than 10 in. to a line through the center of the source and chamber. The lead, being quite flexible, required additional support, so ¾-in. plyboard was placed over the pit leaving an unsupported area 3 by 3 ft.

The split FP–54 electrometer was used as a null indicating system in a circuit recommended by the manufacturer. The values of the compensating voltage, grid leak resistance, chamber volume, temperature, pressure, and air wall correction [4] served to determine the dosage rate at

[4] G. C. Lawrence, Can. J. Research [A], **15**, 67 (1937).

the chamber. All dosage measurements were referred back to a distance of 1 m from the source. The grid leak resistance values were determined by calibrating a 10^9 ohm resistance and then making frequent intercomparisons. The unknown resistances were then determined from the comparison ratios.

III. Results

An auxiliary experiment was performed to determine the amount and the effect of extraneous scattering from the pit walls and floor. The source was suspended 138 cm below the chamber, so that the chamber-to-source distance was fixed. The source and chamber were moved together in elevation up to a distance of 7 m above the floor. The dosage rate gradually decreased and became constant for elevations above 3 m. Since the source-to-chamber distance was roughly one-fifth the distance to the nearest wall, the wall scattering is considered negligible. This dosage rate corrected by the inverse square law to 1 m, was taken as the number of roentgens per hour at 1 m for this particular source.

TABLE 1. *Experimental narrow-beam attenuation data for gamma rays from cobalt*

Material	Atomic number, Z	Atomic weight, A	Z/A	μ/ρ	$\mu A/\rho Z$*
Concrete	----	----	0.50	0.055	0.111
Steel	26	55.85	.465	.054	.115
Copper	29	63.57	.456	.052	.115
Tin	50	118.7	.422	.050	.119
Lead glass, 65% PbO and 8% BaO	----	----	.433	.059	.136
Lead	82	207	.396	.057	.144

* μ/ρ is the mass absorption coefficient in cm^2 gram; μ is the linear absorption coefficient in centimeters^{-1}; and ρ is the density of the material in gram cm^{-3}.

Measurements taken without absorbers and at various positions of the source showed deviations from the inverse square law. The comparison between the inverse square values and the value determined by the auxiliary experiment indicates that the scattering varies from 2 percent with the source at the top of the pit and the chamber 40 cm above the pit, to 8 percent with the source moved down to 210 cm from the top of the pit. Thus the scattering correction applied to those points determining the attenuation curves reported here was 2 percent. The experimental error is considered to be approximately ± 5 percent.

Figure 3 shows the broad-beam attenuation curves for lead, steel, and concrete. The distance from the chamber to the emergent side of the barrier is 40 cm and the source-to-barrier distance is 4 cm. As a comparison, two points from data previously obtained by Robertson [5] have been included on the broad-beam curve for lead. These data, taken with cylindrical lead shields enclosing the entire source, are expected to be

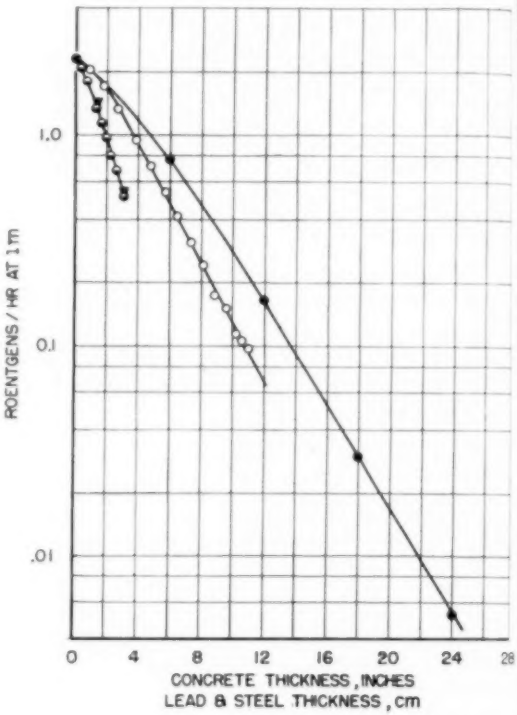

FIGURE 3. *Broad-beam attenuation curves for gamma rays from Co^{60}.*

●, Concrete; ◒, lead, ○; steel; ▼, Robertson's lead curve.

higher due to the side-scatter and back-scatter from the lead shields. It is seen that these points are about 3 percent higher than the data reported here. The narrow-beam data, table 1, indicate that there is little difference in the photoelectric absorption in concrete and steel. On the basis of mass per unit area, the concrete and steel attenuation curves are the same. It is expected that materials of atomic number between steel and concrete would also follow the same attenuation curves. The broad-beam attenuation curves of

[5] K. Z. Morgan, J. App. Phys. **19**, 593 (1948).

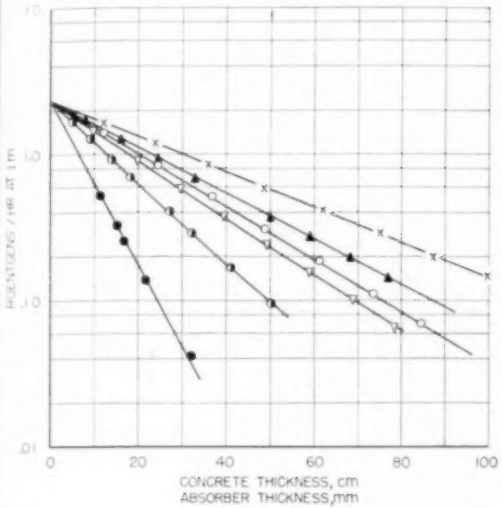

FIGURE 4. *Narrow-beam attenuation curves for gamma rays from Co.*[60]

●, Concrete; ◑, lead; ○, steel; X, lead glass; ▽, copper; ▲, tin.

figure 3 are, therefore, applicable over this range of atomic numbers provided the same mass of barrier is used.

Table 1 gives the experimental absorption coefficients determined from the narrow-beam logarithmic transmission curves of figure 4. The quantity $\mu A/\rho Z$ is proportional to the electronic absorption coefficient. This factor increases with atomic number and illustrates the importance of photoelectric absorption in materials of high atomic number. The absorption coefficients are in good agreement with those reported by Mayneord and Cipriani.[6] As an indication that the scattering measured in the narrow beam was negligible, the dosage rate observed with no absorber agreed with that obtained in the auxiliary experiment described above.

Figure 5 shows the experimental variation in dosage rate with distance between the chamber and barrier for different distances between source and barrier. All data have been computed back to a distance of 1 m from the source by the inverse square relation and also have been corrected for the scattering from the pit walls. The solid curves indicate the dosage rates measured for the two different source positions. For these measurements, 1 ft of the outer edge of the pit opening was covered with ¼ in. of lead to reduce the scattered radiation from the pit walls and 18-in. "concrete covers". The upper curve of group *A* shows that the scattering is mainly from the sides of the pit opening in that the abrupt change in slope occurs at the point where the chamber just falls into the shadow of the lead and no longer "sees" any of the sides of the pit opening. The dotted line at 2.33 roentgens/hr at 1 m is the dosage rate determined by the auxiliary experiment. The increased dosage rate above 2.33 roentgens/hr at 1 m for the source 4 and 210 cm from the top of the pit is due to the extraneous scattering and provides the basis for our scattering correction.

The slight positive slope of the upper curves of groups *B*, *C*, and *D* is due to the apparent change in beam diameter as seen by the chamber and can be explained as follows:

With the source only 4 cm from the barrier, the attenuation in the outer rings of the beam is greater due to the increased path length of the incident plus the scattered photon in the barrier

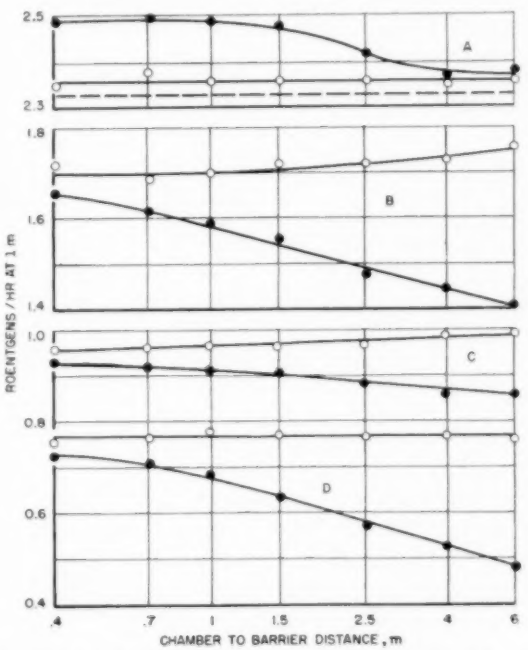

FIGURE 5. *Variation in dosage rate with distance between the chamber and barrier for different source distances.*

The inverse square correction has already been made. A, No absorber; B, 1.68 cm of steel; C, 1.9 cm of lead; D, 6 in. of concrete. Source to barrier distance: ○, 4 cm; ● 210 cm.

[6] W. V. Mayneord and A. J. Cipriani, Can. J. Research [A], **25**, 303 to 314 (1947).

for small chamber-to-barrier distances. As the chamber-to-barrier distance increases, the path length of the incident plus the scattered photon is less so that the apparent beam diameter increases. For the greater chamber distances the angle of scattering is less and the photon energy greater, thus decreasing the apparent attenuation of the radiation.

For the lower curves of groups, *B*, *C*, and *D* with a source-to-barrier distance of 2.1 m., the effective beam diameter is essentially the same for all chamber-to-barrier distances, being controlled by the pit aperture. The predominant factor in the apparent increase in attentuation is that as the chamber moves away from the barrier, less of the scattered radiation is measured by the chamber, and thus a narrow beam condition is being approached. As previously described (see footnote 1), if the barrier-to-chamber distance is made sufficiently large these curves level off at a value corresponding to the narrow-beam data for that absorber thickness.

When the data were reduced to a distance of 1 m from the cobalt source, no attempt was made to correct for the inverse square law for the distance to the apparent barrier source, the barrier being the source of all scattered radiation.

Table 2 gives the shielding required for cobalt-60 sources at various distances. The lead requirements were taken from data obtained by Robertson as cited by Morgan (see footnote 5). The concrete requirements were obtained from the broad-beam attentuation curves figure 3, the dosage rate being reduced to the permissible rate of 300 milliroentgens per 48-hr. work week. All thicknesses are in inches.

TABLE 2. *Primary protective barrier requirements for Co^{60}*

All thickness are in inches. Column headings 1 meter, 2 meters, 3 meters indicate the relative barrier to chamber distances

Number of me	1 meter		2 meters		3 meters	
	Lead	Concrete	Lead	Concrete	Lead	Concrete
1	0	0	0	0	0	0
10	0.70	4.9	0	0	0	0
50	1.92	10.8	0.88	5.9	0.17	1.5
100	2.41	13.3	1.40	8.3	.78	5.3
250	3.05	16.6	2.08	11.6	1.49	8.8
500	3.53	19.1	2.57	14.1	2.00	11.2
1,000	4.03	21.5	3.05	16.6	2.48	13.7
2,000	4.51	24.0	3.53	19.1	2.97	16.2

WASHINGTON, September 7, 1949.

U. S. Department of Commerce
National Bureau of Standards

Research Paper RP2067
Volume 44, February 1950

Part of the Journal of Research of the National Bureau of Standards

Pulse Packing in Magnetic Recording Wire[1]

By Irvin L. Cooter

An oscillographic method is described for determining the relative pulse packing of different types of magnetic recording wire used for pulse storage. Typical curves are presented to show the influence of the amplitude, duration, and repetition rate of the magnetizing pulses on the pulse packing in two types of recording wire.

A powder pattern method is also described for visually observing the length of the magnets produced in the wire by the magnetizing pulses. Photographs are shown of typical patterns. The data obtained by this method verify the pulse packing data obtained by the oscillographic method.

I. Introduction

One of the principal requirements of high-speed electronic digital computers is the rapid interchange of data between their input and output components. It is also of advantage to be able to erase and correct recorded data or to discard a given set of data and use the same storage medium again for another set. The ease with which the magnetization of a wire or tape can be erased has led to the adoption of magnetic recording for this purpose. In this application, information in the form of coded groups of magnetic pulses is stored in a magnetic wire or tape, and after this information has served its purpose it can be erased at will. The magnetizing pulses are brief pulses of current in the magnetizing coil of a specially designed electro-magnet usually referred to as the input or recording head. The localized magnetic field produced by the current pulse magnetizes the recording medium whose properties determine the magnetic strength of the minute magnets produced. Successive current pulses of opposite polarity will produce magnets in the wire whose adjacent poles have the same sign. Likewise successive current pulses of the same polarity will produce magnets whose adjacent poles are unlike. When the magnetized wire is moved across the air gap of an output head similar in construction to the input head, pulses of voltage are generated in the output coil surrounding a lamination. If the magnets are crowded too closely together in the wire, the output voltage pulses will be affected. However, in order to conserve space it is necessary that the maximum number of pulses be recorded in each linear inch of the medium without the output pulses losing distinctness or objectionably blending with the preceding or succeeding pulse. The term "pulse packing" will be used to designate the number of magnets per unit length of the recording medium.

The maximum practicable pulse packing is limited by the interference between successive output pulses and by the signal-to-noise ratio for the output pulses. Since the factors that tend to increase the output voltage at the same time tend to increase the interaction between adjoining magnets, it is necessary to select as small an output voltage as is feasible and then to determine the greatest pulse packing for that voltage and the allowable interference.

Fortunately, in pulse recording as applied to electronic digital computers, distortion in the output pulses is not a critical factor, since the pulses generally operate trigger circuits. Moreover, the peak amplitude of the output pulse can vary considerably since clipping circuits are used between the output heads and the trigger circuits.

Investigations of the magnetizing current, pulse duration, and repetition rate as related to the amplitude and allowable interference of the output pulses on a wire recording medium have been made and are reported in this paper. A technique

[1] This work was partially supported by the Office of the Chief of Ordnance, Department of the Army.

for visually examining the magnetized wire and determining the length of the magnetized section produced in the wire by the current pulses is also described.

II. Input and Output Pulses

Since it was desired to study not only the effects of amplitude and repetition rate of the recording pulses but also the effect of the duration of the peak current on the output pulses, recording pulses having an approximately rectangular shape were chosen for use in the experiments. Furthermore, since sequences of positive and negative current pulses are chosen for coding "words," rectangular pulses of both polarities are required. Each pulse of current in the magnetizing head produces a pair of poles or a minute magnet in the wire. The polarity of the current pulses will determine the direction of the magnet. Successive magnetizing pulses of opposite polarity produce a succession of short cylindrical magnets with adjacent poles of like polarity joined by a ferro-magnetic medium. If the duration of the magnetizing pulses is short compared to the speed of the wire, the elongation of the small magnet on the wire that results from the pulse duration may be neglected. Since the wire speed in these experiments was 12 in./sec, magnetizing pulses of less than 20 microseconds duration lengthen the magnet less than 0.00024 in.

When a magnetized wire is drawn across the air gap of the output head, the magnets serve as a source of magnetizing force, and the resulting induction in the head links the output coil. Changes in flux linkages as the magnets move across the air gap induce voltages in the coil. As the magnets are packed closer and closer together in the wire, more effect is produced between the magnetic fields of adjoining magnets until sufficient distortion is produced in the magnetic fields to measurably change the shape of the output voltage pulses. Also, the overlapping of magnetic fields prevents the amplitude of the output voltage from becoming zero between successive magnets. The ratio of the minimum output voltage between magnets to the maximum output voltage is defined in this report as the interference ratio.

III. Interference Ratio

In *a*, left side of figure 1, are shown two input current pulses of opposite polarity. These two pulses produce two magnets in the wire as shown in *b*. These magnets produce two pairs of readback pulses as shown in *c*. For the case shown in the left side of figure 1 the repetition rate of the input pulses is low enough so that the output

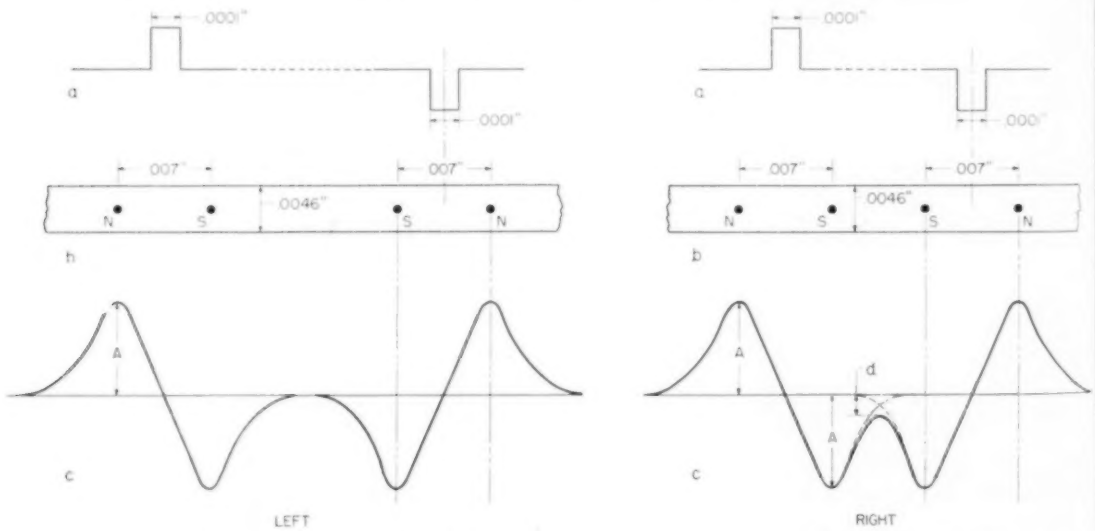

FIGURE 1. *Magnetization of recording wire by rectangular current pulses and the output voltage pulses.*

Left: a, Magnetizing pulses duration, 10 microseconds; amplitude, 40 ma. b, Magnets in recording wire. c, Output voltage pulses interference ratio=
Right: a, Magnetizing pulses duration, 10 microseconds; amplitude, 40 ma. b, Magnets in recording wire. c, Output voltage pulses interference ratio=

voltage (e) drops to zero between successive magnets. In the right side of figure 1 the repetition rate is sufficiently high to prevent the amplitude of the read-back voltage in e to return to zero between magnets. In this figure the interference ratio is shown as d/A. It is obvious that the interference ratio is zero for successive pulses of the same polarity. An interference ratio of 0.1 (or 10%) was chosen as the criterion of satisfactory pulse packing. Consequently d in right side of figure 1 should not exceed 10 percent of A.

It should be noted from figure 1 that whereas the magnetizing pulse has a duration of 10 microseconds corresponding to a length of only 0.00012 in. on the wire at a wire speed of 12 in./sec. it produces a magnet several thousandths of an inch long in the wire. Later in this report this will be explained as resulting from the extended magnetic coupling between the wire and head.

IV. Apparatus

1. Loop Tester

In order to study the effects of input pulse parameters on pulse packing, apparatus was constructed that requires a single continuous loop of recording wire approximately 8 ft. long. The advantages of a loop tester over apparatus using reels include simplification of the driving mechanism and the elimination of reeling difficulties.

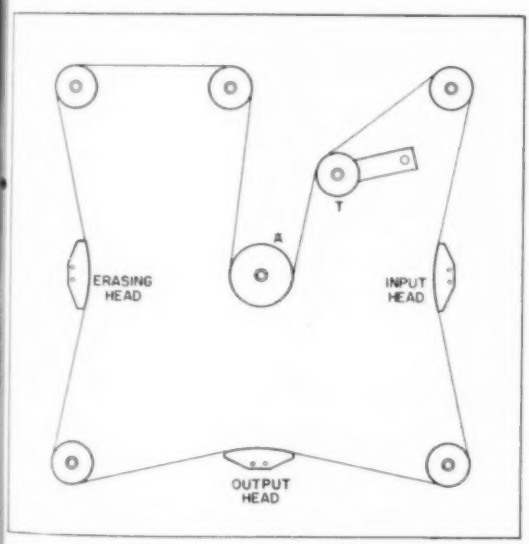

FIGURE 2. *Loop tester.*

The use of a short length of wire also decreases the probability of variations in output pulses arising from nonuniform magnetic characteristics that can occur in long lengths of recording wire. Separate input, output, and erasing heads were used. These heads were spaced sufficiently far apart to prevent noticeable electro-magnetic interaction between the heads. Figure 2 shows the top view of the loop tester. The driving force is supplied to the wire loop through the driving pulley, A, by a multipole phonograph motor mounted beneath and direct-coupled to the driving pulley. The wire is positioned by five grooved pulleys. The take-up pulley, T, serves to adjust the tension in the wire so that good contact is possible between the heads and the wire.

2. Wires and Heads

Two types of wire were tested, solid stainless steel and Co-Ni plated wire.[2] The stainless steel wire is a solid metal wire specially cold worked in the drawing process in order to produce the magnetic properties suitable for magnetic recording wire. The stainless steel wire generally used has a diameter of 0.004 in. The plated wire consists of a magnetic coating of cobalt-nickel alloy plated on nonferrous material such as brass or phosphor bronze. The magnetic coating is generally 0.0003 in. thick, and the nonmagnetic wire is 0.004 in. in diameter. Thus the plated wire is 0.0046 in. in diameter compared with 0.004 in. for the stainless steel wire (see fig. 3). The values obtained for the intrinsic coercive force (H_{ci}) and the residual induction (B_r) of the wires used in this investigation are given in the following tabulation.

Type of wire	H_{ci}	B_r
	Oersted	*Gauss*
Stainless steel	150	3, 700
Plated wire	220	9, 700

These values were obtained from a maximum magneti ing force of 1,000 oersteds.

The magnetization of the wire is longitudinal along the wire parallel to the direction of motion. Transverse recording cannot be used, since twist-

[2] Frequency response of magnetic recording by Otto Kornei, Electronics, Vol. 20, No. 8, pp. 124 to 128 (August 1947).

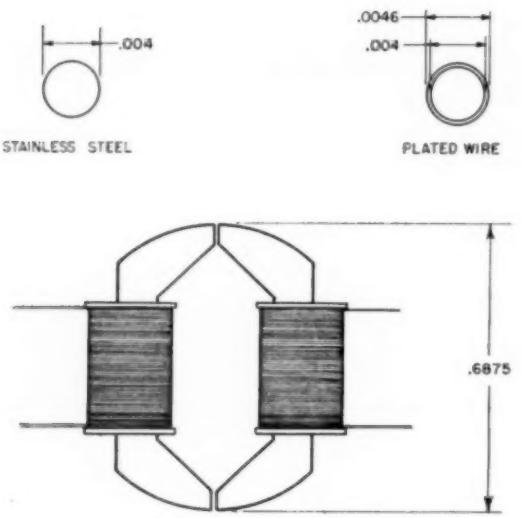

FIGURE 3. *Two types of magnetic recording wire and a magnetizing head.*

ing or rotation of a wire about its longitudinal axis during spooling could reverse the polarity of the magnet as read back by the output head. This change in polarity could result in errors in the numerical values of the coded numbers.

The magnetic heads were not especially designed and constructed for pulse recording but are commercially available sound recording heads. Their construction is shown in figure 3. Each head consists of a core of two molybdenum permalloy laminations, 0.014 in. thick, with a coil of 900 turns surrounding each lamination. The gaps between the laminations are approximately 0.001 in. long. In addition to the gaps between the laminations, there is also an effective air gap between the recording wire and the laminations. Even small spatial variations in this gap between the wire and head can produce appreciable changes

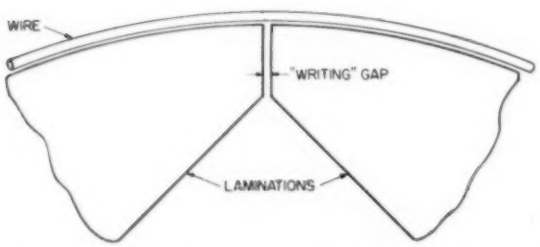

FIGURE 4. *Enlarged view of the region near a "writing" gap of a magnetizing head.*

in the size and shape of the output pulses. An enlarged view of the "writing" gap between the lamination and the smaller effective air gap between the wire and head is shown in figure 4. The wire and the head are magnetically coupled for some distance each side of the writing gap by the fringing flux. This may account for the fact that the magnets produced in the wire are several times as long as the gap.

3. Recording Circuit

As mentioned above, the magnetizing heads used have two coils, one on each lamination. This allows a simple circuit to be used for producing successive magnetizing pulses that produce fields having opposite directions.

A schematic diagram of the circuit and apparatus used for supplying input pulses of opposite polarity to the recording head is shown in figure

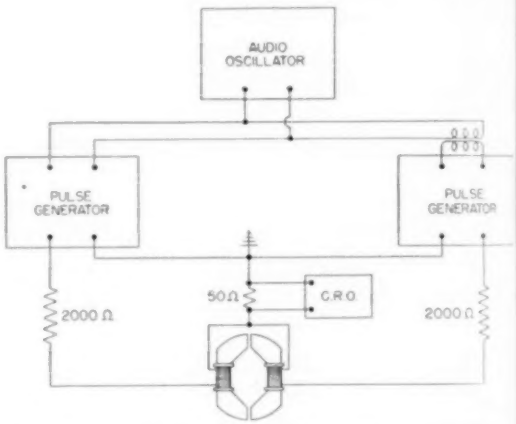

FIGURE 5. *Recording circuit for rectangular input pulses.*

5. In this figure is shown an audio oscillator supplying the input of two pulse generators. One pulse generator is fed directly from the oscillator, and the other pulse generator is fed through a transformer. The transformer is used to shift the phase of the input voltage to this pulse generator by approximately 180° from the input voltage of the direct-fed pulse generator. The ground sides of the generators are connected together at one terminal of a 50-ohm resistor. The resistor is then connected to the common side of the magnetizing coils. The other terminal of each generator is connected to a magnetizing coil through a resistor of 2,000 ohms. The 2,000-ohm

resistors were found necessary to obtain a satisfactory time constant for the circuit. With the above circuit constants, the magnetizing current pulse as observed across the 50-ohm resistor by the cathode ray oscillograph is practically rectangular. The amplitude and shape of the current pulses, as well as the time relations of the pulses from the two generators can be observed on the cathode ray oscilloscope. This oscilloscope is calibrated by means of a sine wave, so that peak values of current can easily be determined.

The pulse repetition rate is controlled by the oscillator and the pulse duration, amplitude, and polarity are determined by the dial settings on the pulse generators. By the use of the apparatus and circuit described above, the recording wire can be magnetized by current pulses of alternate polarities or the same polarity. Thus studies can be made of the effect of pulse amplitude, duration, and repetition rate on the interference ratio.

4. Output Apparatus

The current pulses in the magnetizing coils are recorded in the wire as minute magnets. As the magnetized wire is moved across the air gap of the output head, varying induction is produced in the permalloy core; the variations in induction through the coil generate voltages at the coil terminals having peak values up to 5 or 6 mv. This small alternating voltage is amplified and then observed on a calibrated cathode ray oscilloscope. A battery-operated resistance-capacity coupled preamplifier is connected between the output head and the amplifier of the cathode ray oscilloscope. On the screen of the oscilloscope, the values of d and A are read for different values of pulse duration, amplitude, and repetition rate. The oscilloscope is calibrated to read peak voltages so that the output voltage as well as the interference ratio can be obtained from the data. Since stationary synchronized patterns are produced on the oscilloscope, the reading of d and A can be made fairly accurately.

5. Erasing Circuit

A head similar in construction to the input and output heads is used as the erasing head. It was experimentally found that when using a wire speed of 12 in./sec, an erasing current of 17 ma peak to peak at a frequency of 20 kc/sec is suitable for demagnetizing the wire. This current is supplied from a power amplifier connected to the output of an oscillator. During tests with the loop tester the erasing circuit was continuously energized so that the pulses are first recorded, then read back and finally erased.

V. Results

The over-all resolution achieved in a pulse recorder depends both upon the length of the magnets produced in a given wire by the input head and upon the resulting pulses read back at the output head. In sound recording it is well known that the mechanical and magnetic requirements of the output head are much more critical than for the input head. Consequently for this investigation all available heads were successively tried as the output head in the loop tester, and the head that gave the smallest interference ratio for a given magnetizing current, pulse duration, and repetition rate was selected for the output head. It was found that among the 18 heads tried in the output position there was a spread of approximately 50 percent in the pulse packing for the same interference ratio. This indicates that the data presented on pulse packing can be considered only as a comparison between wires tested or as relative effects of certain parameters on the same wire and may not represent the greatest packing possible.

The data are also presented in most cases with the peak input current as a variable, whereas for comparison purposes it would be more logical to state the variable as current-turns. However since each magnetizing coil has 900 turns, ampere-turns can be obtained by multiplying the current in milliamperes by 0.9.

Comparisons between the output peak voltages as a function of input peak currents for the two types of wire are shown in figure 6. These curves indicate that the output voltage for an input pulse of 10-microseconds duration is proportional to the peak input current until a peak current of approximately 20 ma is supplied to the magnetizing coil. Then the curves tend to level off so that a large increase in input current causes only a slight increase in the output voltage. The repetition rate for a given pulse duration and peak input current has only a slight effect on the output

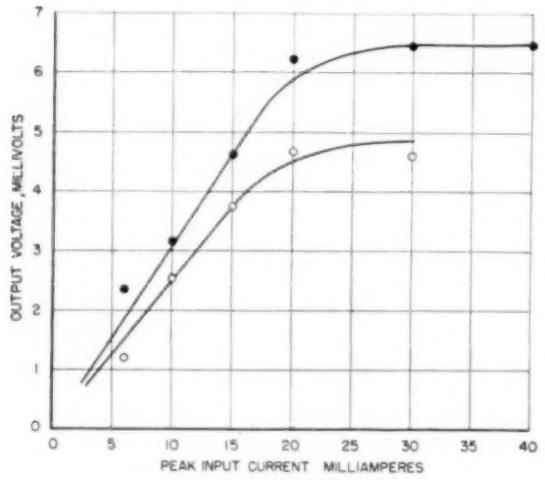

FIGURE 6. *Variation of peak voltage of output pulses with magnetizing current.*

●, Plated wire; ○, stainless steel wire; Wire speed, 12 in./sec; pulse duration 10 microseconds.

voltage. For example, the output voltage for the plated wire remained constant at 4.65 mv when the pulse repetition rate was varied from 50 to 117 pulses per inch.

Figure 7 shows the effect on output peak voltage of increasing the duration of the input pulse. In general the output voltage is proportional to pulse duration for short pulses. As the pulse duration is increased, smaller and smaller relative increases occur in output voltage until the curves apparently level off.[3] Under similar conditions the plated wire has a greater signal output for the same input.

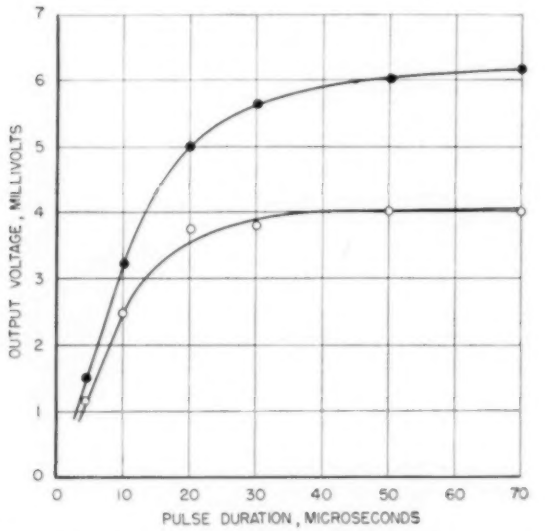

FIGURE 7. *Variation of peak voltage of output pulses with duration of input pulses.*

●, Plated wire; ○, stainless steel wire; Wire speed 12 in./sec; peak input current 10 ma.

Typical curves for the effect of peak input current on the interference ratio, using plated wire as a recording medium, are shown in figure 8.

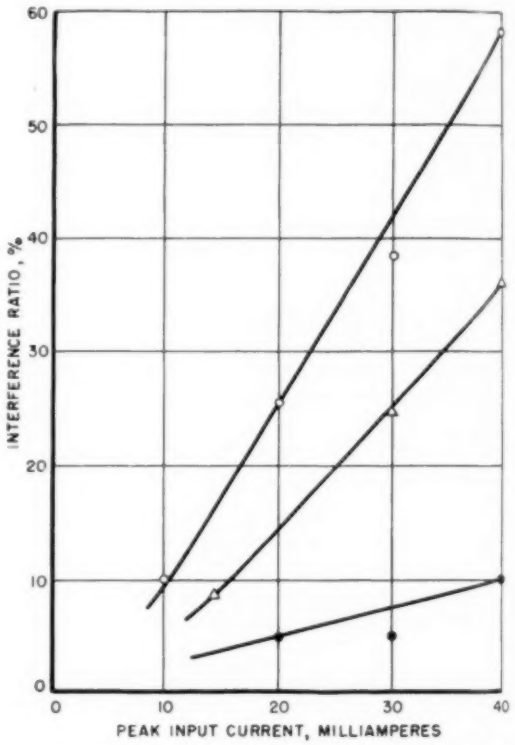

FIGURE 8. *Variation of interference ratio with peak input current.*

In this figure ppi is the abbreviation for pulses per inch. Plated wire; pulse duration 5 microseconds; wire speed 12 in./sec. ○, 100 ppi; △, 80 ppi; ●, 60 ppi.

These curves show that for an input pulse duration of 5 microseconds, and a repetition rate of 60 pulses per inch, the input current may be as large as 40 ma before the interference ratio exceeds 10

[3] L. Cahn of the Bureau's Electronics Computers Section has investigated the storage of pulses whose durations are between 50 microseconds and 6 milliseconds, using plated wire and a wire speed of 2 in./sec. His results show that increasing the pulse duration from 50 microseconds to 5 milliseconds increases the output peak voltage by a factor of two. Further increases in pulse duration produce only small increases in output voltage.

percent. However, if the repetition rate is increased to 80 pulses per inch, 15 ma would be the maximum permissible input current to keep the interference ratio as low as 10 percent. If the repetition rate is increased to 100 pulses per inch, the peak current cannot exceed 10 ma or less if the interference ratio is not to exceed 10 percent.

Figure 9 shows the dependence of the interference ratio on the pulse duration when a peak input current of 15 ma is used. An increase in pulse duration results in an increase in the interference ratio.

Typical design curves can be assembled from the data already presented if two parameters (e. g. pulse duration and interference ratio) are fixed. On the basis of previous experience a pulse duration of 10 microseconds was chosen. Also it was tentatively decided to use an interference ratio of 10 percent as a criterion of suitable performance. Then the relationship between the pulse packing and the peak input current for the two types of wire is represented by the curves in figure 10. From these curves it may be seen that a pulse packing of 60 per inch may be obtained with stainless steel wire for a peak input current of 6 to 7 ma, whereas for the plated wire as much as 23 or 24 ma could be used and a much greater output

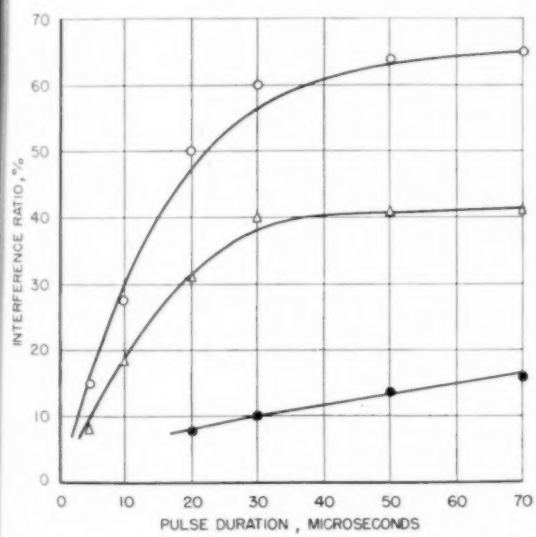

FIGURE 9. *Variation of interference ratio with duration of input pulses.*

In this figure ppi is the abbreviation for pulses per inch. Plated wire; peak current 15 ma; wire speed, 12 in./sec. ○, 100 ppi; △, 80 ppi; ●, 60 ppi.

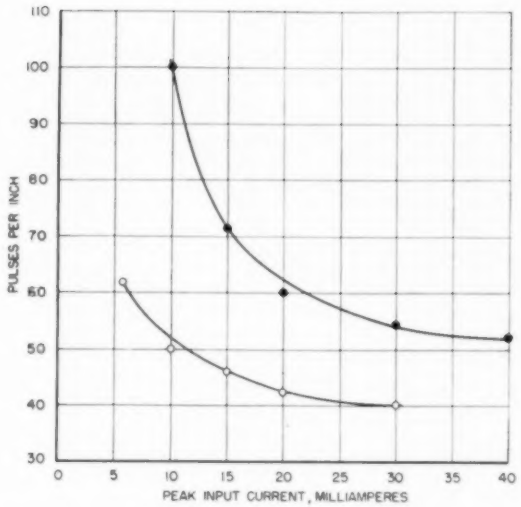

FIGURE 10. *Relation between pulse packing and peak input current for two types of wire.*

Pulse duration, 10 microseconds; interference ratio, 10 percent; wire speed, 12 in./sec. ●, Plated wire; ○, stainless steel.

signal strength obtained, as is shown in figure 6. If more than 100 pulses per inch are desired, this packing could be obtained with the plated wire when less than 10 ma is used in the input head.

VI. Magnetic Patterns

Studies of the magnetizing current, pulse duration, and repetition rate as related to the interference ratio gave useful data on the over-all performance of a pulse recorder. It is known, however, that the length of the air gap in the output or reproducing head has considerable effect on the high frequency response of magnetic recorders, and it was considered possible that the small magnets in the wire resulting from the current pulses may be "spread out" by the output head. Consequently it was very desirable to determine directly the length of the magnets on the wire. A wire retaining magnetically recorded pulses is similar to a succession of short cylindrical magnets laid in a line and connected end to end by a ferro-magnetic medium. Therefore if the magnetic field surrounding these minute magnets could be mapped and the pattern photographed, the length of the magnet could easily be determined. As is well known from elementary physics, iron filings when scattered about a magnet are not only attracted to the magnet but also

arrange themselves in definite lines that appear to begin and end at the so-called poles of the magnet. These lines of iron filings are said to "map" the magnetic field. In a similar way the magnetic field of extremely small magnets can be mapped if the iron particles are sufficiently small and proper techniques are used in producing the pattern.

VII. Pattern Formation

A sample of wire approximately 3 in. long, taken from a loop of wire magnetized in the usual way on the loop tester is mounted on a clean glass plate with sufficient tension to hold the wire tightly against the glass surface. The glass plate with the attached wire is then placed on the stage of a standard Bausch and Lomb Contour Measuring Projector. Referring to figure 11, the wire is shown at (5). The wire is illuminated by an optical system consisting of a tungsten arc lamp (1), a pair of achromatic condensers (2), and a mirror (3). The image of the wire is projected by a lens, roof prism, and mirror system onto a vertical screen. The vertical screen is an 8- by 10-in. ground glass plate upon which the magnified image of the wire is focused.

The fine magnetic powder used to delineate the external magnetic field is composed of carbonyl iron particles having an average diameter of approximately 0.0001 in. The carbonyl iron particles are suspended in an acid-free oil having an SAE viscosity rating of 10. The proportion of iron particles to oil is not critical but is varied according to the density of pattern that is desired.

Referring again to figure 11, a drop of iron-particle suspension is placed on the wire at (5). The iron particles settle at a rate suitable to give a definite and distinct pattern of the external field surrounding the wire.

The particles in the strongest field (near the wire) are attracted and adhere to the magnetized portion of the wire and build up a pattern in a few minutes that extends out a distance approximately equal to one-half to the full diameter of the wire. The portion of the pattern than is produced on the glass plate takes longer for the settling to be completed since the magnetic forces acting there are much smaller. Usually a satisfactory pattern will be produced in approximately 30 min. After the pattern is formed, the ground glass plate in the contour measuring projector is

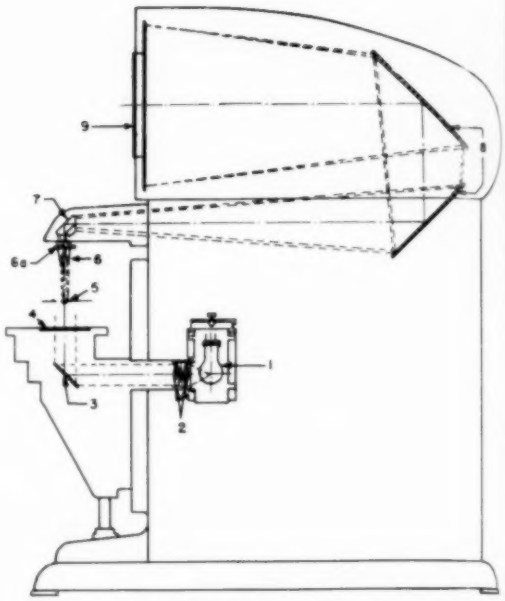

FIGURE 11. *Modified Bausch and Lomb Contour Measuring Projector.*

1, Tungsten arc lamp; 2, achromatic condensers; 3, mirror; 4, stage; 5, magnetized wire; 6, lens; 6a, camera shutter; 7, roof prism; 8, mirrors; 9, viewing screen.

replaced with film and the pattern photographed. The exposure time is controlled by means of a camera shutter (6A) built into the lens mounting.

VIII. Magnetic Field Patterns

Figure 12 illustrates the type of pattern obtained by this method for plated wire 0.0046 in. in diameter, erased at a frequency of 20 kc/sec and recorded at a wire speed of 12 in./sec. The total magnification is 150 diameters unless otherwise stated.

Figure 12, A shows three magnets produced in the wire with pulses of 40 ma peak current, 70-microseconds duration and a pulse-repetition rate of 60 pulses per inch. With only a small number of carbonyl iron particles in the field, a clear and distinct pattern is obtained, which allows measurement of the effective length of the magnets. For comparative purposes the effective length of the magnet is taken as the distance between the poles. Figure 12, B is a photograph of the same pulses as in figure 12, A except that more carbonyl iron particles have been added and the extended field is clearly shown. The successive magnetizing

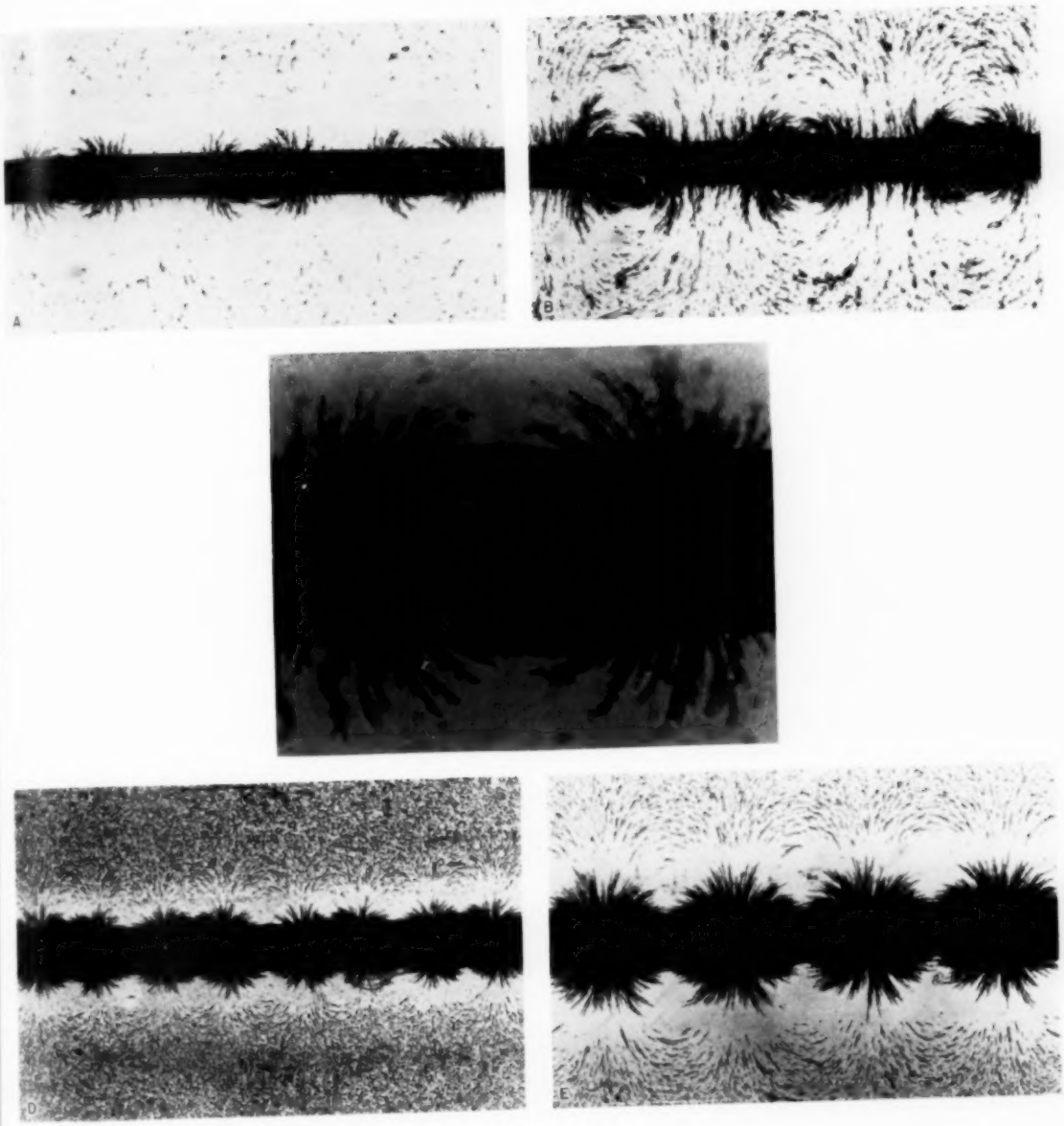

FIGURE 12.

A, Magnets produced by three pulses of opposite polarity; peak current, 40 ma; pulses per inch, 60; pulse duration, 70 microseconds. B, Same as A but showing the extended field. C, Pulse from A, total magnification 640 diameters. D, Magnets produced by four pulses of the same polarity; peak current, 40 ma; pulses per inch, 70; pulse duration, 10 microseconds. E, Magnets produced by a sine wave current; peak current, 8.5 ma; cycles per inch, 35.

pulses were of opposite polarity, so that neighboring poles of successive magnets are of the same kind and result in characteristic patterns as shown in the photograph.

A further enlargement of one of the pulses in figure 12, A is shown in figure 12, C. This photograph was made with an enlargement of 640 diameters.

Figure 12, D shows four magnets produced by four pulses of the same relative polarity. These pulses had a peak current of 40 ma, a duration of 10 microseconds, and a repetition rate of 70 per inch. Neighboring poles of adjacent magnets are of opposite sign.

The type of pattern obtained when the wire is magnetized with a sine wave current is shown in figure 12, E. The peak value of current in 1,800 turns was 8.5 ma, 35 cycles per inch being recorded. At a wire speed of 24 in./per sec (frequently used in magnetic recording) this would correspond to a recorded tone of 840 c/s. If each sine wave is considered as two pulses of opposite polarity, each of the four poles shown in the photograph is seen to be a pair of poles of the same sign.

In comparing the results obtained by the visual method with the data on pulse packing, it must be borne in mind that the output pulse voltage begins before the leading pole of the magnet reaches the writing gap and continues after the trailing pole has left the gap. Measurements made on the photograph of figure 12, A and others, indicate that the average distance between poles is of the order of 0.008 in. for magnetizing pulses having a peak value of 40 ma and a duration of 70 microseconds. These photographs also show that the external field of the minute magnets is appreciable for several thousandths of an inch beyond each pole. Oscillograph records obtained with the loop tester using similar pulse parameters for recording, indicate that the duration of the voltage of the output pulse corresponds to the time required for the wire to travel between 0.016 and 0.020 in., which is between 2 and 2½ times the distance between the poles of the magnet as indicated visually.

IX. Conclusions

A method and apparatus are described for determining the relative pulse packing of different types of magnetic recording wire used for pulse storage. Typical curves are presented to show the influence of the amplitude, duration, and repetition rate of the magnetizing pulses on the pulse packing in two types of recording wire.

A powder pattern method is described for visually observing the length of the magnets produced by the magnetizing pulses. The data obtained by this method verify the pulse-packing data obtained by the interference ratio method.

Using an interference ratio of 0.1 as a criterion, it is possible to pack approximately 100 pulses per inch in the plated wire, when the input pulses have a length of 0.0001 in. (i. e. 10 microseconds) and a peak current of less than 10 ma.

From a study of the photographs (fig. 12) it is concluded that magnets whose average length is 0.008 in. are produced in plated wire 0.0046 in. in diameter by magnetizing pulses of 40 ma through 900 turns (i. e. 36-amp turns), if the duration of the input magnetizing pulse is 70 microseconds, and the wire speed is 12 in./sec. If the input pulse parameters are the same except that the duration is decreased to 10 microseconds, the average length of the magnet is decreased by 0.001 in.

Washington, August 17, 1949.

U. S. Department of Commerce
National Bureau of Standards

Research Paper RP2068
Volume 44, February 1950

Part of the Journal of Research of the National Bureau of Standards

Note on the Stabilization of Acetylglycosyl Halides and Sugar Acetates

By Horace S. Isbell and Harriet L. Frush

In connection with an investigation of the stereomeric factors affecting replacement reactions,[1] it was necessary to prepare and store a number of acetylglycosyl bromides. These compounds are useful intermediates for the synthesis of sugars and many sugar derivatives. Their utility for synthetic purposes depends upon the high reactivity of the halogen, but this property also makes them relatively unstable. Decomposition is accelerated by the presence of water, alcohol, acids, or other substances that react with active halogen; the resultant hydrogen halide, unless removed, acts catalytically to cause further deterioration. To restrict decomposition, it has been customary to store acetylglycosyl halides at low temperatures over sodium hydroxide in a vacuum desiccator.[2] Even under these conditions, certain acetylglycosyl halides decompose in a short time.[3]

It has now been found that the addition of a small quantity of an insoluble substance capable of neutralizing the acid formed by incipient decomposition stabilizes the acetylglycosyl halides to a striking degree. Finely powdered carbonates, especially those of calcium and barium, are particularly useful; the quantity added for stabilization is not critical, but may be varied to suit conditions of storage and purity. The solid carbonate is advantageous during the purification of the substance as well as in the final product. For some purposes the presence of the inorganic carbonate is not objectionable; but if the pure acetylglycosyl halide is desired, it can be separated when required by dissolving the material in an organic solvent and filtering the solution.[4]

To illustrate the effectiveness of carbonates in the stabilization of acetylglycosyl halides, two 0.2-g samples of tetraacetylmannosyl bromide, one of which contained 1 percent of calcium carbonate, were sealed in glass and stored at 20° C. Figure 1 shows the difference in appearance after 1 week. The samples were then dissolved in 40 ml each of chloroform, and light

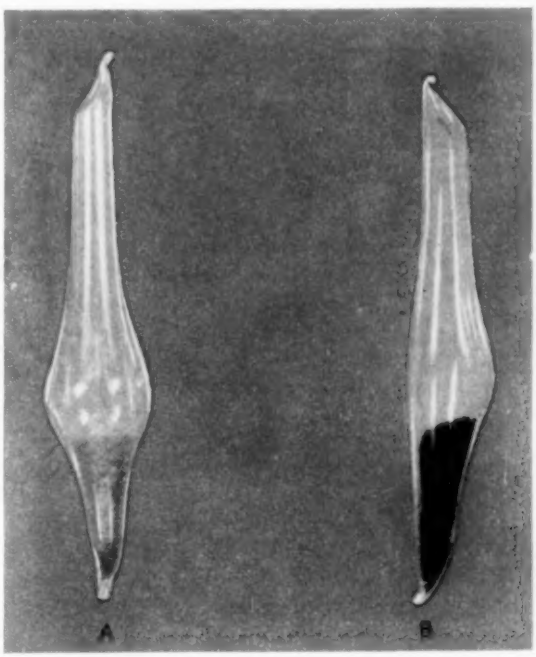

FIGURE 1. *Effect of a trace of calcium carbonate on the stability of tetraacetylmannosyl bromide.*

A, Tetraacetylmannosyl bromide containing 1 percent of calcium carbonate; B, tetraacetylmannosyl bromide untreated.

[1] H. S. Isbell and H. L. Frush, J. Research, NBS **43,** 161 (1949).

[2] D. H. Brauns, J. Am. Chem. Soc. **51,** 1820 (1929).

[3] In general, the reactivity of the acetylglycosyl halides increases from the fluorides to the iodides. For synthetic purposes, the chlorides and bromides are the most useful.

[4] In some organic solvents a trace of calcium halide will be brought into solution at this point, if calcium carbonate has been used. If this is objectionable, the acetylglycosyl halide may be recrystallized and separated immediately before use.

transmittancy measurements were made at 436 μ. In a 1-cm cell, the stabilized sample showed a transmittancy of 96 percent, and the untreated sample of only 53 percent.

Calcium carbonate has been found useful, also, in the long-term storage of sugar acetates. Most of these acetates decompose to some extent on long standing, especially if slightly impure. Thus a bottle of commercial glucose pentaacetate that had been kept for several years was found to have a strong odor of acetic acid. A slightly impure heptose acetate was converted almost entirely to the free sugar during long-term storage. It has been the practice in this laboratory for the past 2 years to mix acetates, unless highly purified and carefully dried and sealed, with a small amount of calcium carbonate before storage. No such preparation has shown evidence of decomposition.

WASHINGTON, October 4, 1949.

U. S. Department of Commerce
National Bureau of Standards

Research Paper RP2069
Volume 44, February 1950

Part of the Journal of Research of the National Bureau of Standards

Phase-Equilibrium Studies of the High-Lime Portion of the Quinary System Na_2O-CaO-Al_2O_3-Fe_2O_3-SiO_2[1]

By William R. Eubank [2]

Two means, one graphic and the other analytic, for studying the phase-equilibrium relations in a portion of the five-component system Na_2O-CaO-Al_2O_3-Fe_2O_3-SiO_2 are described. Using the graphic procedure, compositions in two series of planes in the quinary system were investigated by the quenching method. In each of the two series one component was held constant and another given different values in successive planes. In each plane two components remained constant while three were varied. In this way the minimum temperature for complete melting in each plane was determined. Data for a number of these planes were then employed to locate the quinary invariant point, which was found to have the composition, 1.0 Na_2O, 48.0 CaO, 31.0 Al_2O_3, 13.5 Fe_2O_3 and 6.5 percent of SiO_2. At this point the five crystalline phases, $Na_2O.8CaO.3Al_2O_3$, $3CaO.Al_2O_3$, Fe_2O_3-containing solid solution, $2CaO.SiO_2$, and $3CaO.SiO_2$ exist in equilibrium with liquid.

The temperature of the invariant point was found to be 1,310° ± 3° C. Compositions including the five constituents and approximating that of portland cement clinker will crystallize completely, upon slow cooling, at or near 1,310° C. The stable existence of the soda compound $Na_2O.8CaO.3Al_2O_3$ in the presence of the principal components of clinker was established. The data obtained permit a closer approximation of the amount of glass in rapidly cooled clinker. Dicalcium silicate and the iron-containing phase were observed to exist in various forms of solid solution.

Application of an analytic method for locating and following compositions within the quinary system has likewise been made. Equations have been developed and examples are given for depicting specific planes and points within these planes in the quinary system without the necessity of using geometric relations. The graphic and analytic methods, however, complement each other and together serve as a convenient procedure for studying any system of five components.

I. Introduction

Phase-equilibrium studies on the components of portland cement clinker have proved invaluable in predicting compound composition, explaining chemical activity, and in improving manufacturing practices. The four major components (lime, alumina, ferric oxide, and silica) have been considered, but many of the systems including the minor components (the alkalies, titania, manganese, and others) still await investigation. It is essential, therefore, to extend phase-equilibrium studies of this important material to include additional components and crystallization products.

The presence of soda in portland cement has long been recognized, but the part it plays in the complex cement systems has not yet been fully defined. In the present study the role of Na_2O is examined in a portion of the system N-C-A-F-S,[3] including the composition range of portland

[1] Part of a dissertation submitted to the Board of University Studies of the Johns Hopkins University in conformity with the requirement for the degree of Doctor of Philosophy, granted in June 1947.

[2] Research Associate at the National Bureau of Standards, representing the Portland Cement Association Fellowship.

[3] For convenience, the otherwise cumbersome formulas of the compounds encountered in this investigation are given in the following abbreviated forms:

N = Na_2O,
C = CaO,
A = Al_2O_3,
F = Fe_2O_3,
S = SiO_2.

Thus NC_8A_3 = $Na_2O.8CaO.3Al_2O_3$.

cement. This investigation marks the first attempt, so far as is known, to study systematically and simultaneously the relations of these five components to each other.

Methods for defining the phase-equilibrium relations in binary, ternary, and quaternary systems are well known and have been extensively applied, but with systems of more than four components the difficulty of geometrical representation has severely restricted investigation. It has been customary in the treatment of quaternary systems to select regions that may be reduced to two or three components. In the present study a method is presented for the treatment of a five-component system by graphic methods and also by an analytic treatment developed in this laboratory.

The means of studying quinary systems is of particular interest for an understanding of the constitution not only of portland cement clinker but also of natural rocks and ceramic products, including glasses. The methods herein described for a study of the particular quinary system NC_5A_3-C-C_5A_3-C_2F-C_2S are of a general nature and may be applied to the study of other systems.

A brief review will first be given of the boundary systems previously investigated, followed by the description of the methods employed in this investigation and the results obtained. It should be pointed out that this study has been mainly exploratory, and that a more complete study of the system is a matter for future investigation.

II. Previous Work on Boundary Systems

Of the five quaternary systems bounding the quinary system N-C-A-F-S, one (N-A-F-S) contains no CaO and is not considered significant in this study. A portion of the system C-A-F-S covering the region C-C_5A_3-C_4AF-C_2S was reported in 1934 by Lea and Parker [1] [4] and, more recently, the region C-C_5A_3-C_2F-C_2S was examined by Swayze [2]. A portion of the system N-C-A-S covering the region NA-C-A-C_2S was investigated by Greene and Bogue [3]. Some preliminary studies on the system N-C-A-F in the regions (NA_3)-C-C_4AF and N-C-C_5A_3-C_2F and on the system N-C-F-S in the region N-C-CF-C_2S were reported recently by Eubank and Bogue [4].

[4] Figures in brackets indicate the literature references at the end of this paper.

Temperatures [5] and compositions of certain invariant points determined in these boundary systems are given in table 1.

Throughout this investigation the phase containing iron is designated by the short notation *Fss* indicating an Fe_2O_3-containing solid solution, and for brevity is called the "iron phase." A more quantitative but longer formula for this solid-solution phase is $C_6A_xF_{3-x}$, with x varying from 0 to 2. This represents any composition in a series of solid solutions extending from C_2F to C_6A_2F. These solid solutions have been reported by Swayze [2].

III. Experimental Procedure

The experimental procedure followed the quenching method as described by Bogue [5] with certain modifications. Identification of phases in the quenched charges was made with the petrographic microscope.

Because of the difficulty in obtaining sufficiently rapid cooling to form identifiable crystals, very small charges weighing only a few milligrams were used. Quenching in water, mercury, and liquid air was tried. Mercury did not prove satisfactory, because the charge floated on it with only its underside cooling rapidly. Good quenching resulted in liquid air, even though this has a lower heat capacity than water. Satisfactory results were obtained by quenching very small charges in water. Hydration of the quenched charge was not enough to interfere with petrographic observations.

Platinum envelopes (closed containers), and platinum pans (open containers) as used by Swayze [2], were compared. Loss of soda by volatilization at high temperatures was found to be greater in the case of the open pans. Therefore platinum envelopes were generally used but were reduced to the very small size of 2 to 3 mm square.

An arrangement was employed by means of which two charges of different composition could be quenched simultaneously at a particular temperature. Two pairs of heavy L-shaped platinum leads at the bottom of the quenching assembly were used to suspend, by means of fine platinum wire, two platinum envelopes on opposite

[5] All temperatures are given in degrees Centigrade. Temperature values determined in this study are considered reliable to within ±3 deg; however, temperatures could be controlled to within ±0.1 deg.

sides of the thermocouple junction. The voltage necessary to melt both fine suspension wires was applied at the top of the assembly. Two battery clips, each connecting one lead of each pair, made double quenching possible. This allowed the investigation to proceed more rapidly than is possible in a single-quench operation.

It was found convenient to have a thermocouple mounted in the furnace slightly below the level of the quenching assembly. The temperature of the furnace could then be read and adjusted to the desired value before the charges were introduced. A second thermocouple within the quenching assembly was used for precise temperature measurement. This thermocouple was recalibrated frequently against an NBS standard thermocouple or the melting point of pure $BaO.2SiO_2$ (m. p. 1,418°) [6]. A method of precise temperature control making use of a thyratron quenching-furnace thermostat [7] was developed for this investigation.

The cement compounds and base mixes used in this study were prepared from oxides or carbonates of unusually high purity. Two of these specially prepared starting materials, ferric oxide and silica gel, were of better than 99.99-percent purity by spectrographic analysis. Chemical analysis showed that the sodium and calcium carbonates contained a maximum of 0.04 percent of impurity and that the alumina contained no more than 0.10 percent of impurity. All compounds were ground in a mullite mortar to pass a No. 200 U. S. Standard Sieve. Compositions were dry-ground to insure thorough mixing. Homogeneity was checked by microscopic examination.

The practice of making powder-slides of important charges using Hyrax resin, refractive index 1.715, was continued [4], because this index is very close to that of several cement compounds. Restudy of these permanent specimen-preparations could then conveniently be made.

IV. Methods for Studying a Quinary System

Two means, one graphic and the other analytic, may be used in tracing the phase-equilibrium relations in a system of five components. The first of these, the graphic method, was used for the most part in this study. The analytic method was developed by Dahl [8, 9] subsequent to the use of the graphic method. Both methods will be presented and their applications discussed.

1. Graphic Method

Phase studies in a quaternary system are usually made with a series of triangular sections (diagrams) through a tetrahedron. These may be located in the tetrahedron by choosing various ratios of two of the components and holding these constant for each plane (triangular diagram) or, as is more often the case, planes parallel to the base with a constant amount of the fourth component in each plane may be studied, allowing the other three components to vary. Each plane will represent the intersection of that plane with one or more primary-phase volumes. Invariant points are likely to be located between planes, since the choice of a plane with the exact amount of the fourth component for an invariant point would be accidental. Such points would have to be extrapolated from the data obtained for the planes above or below it, or additional planes between the two might be studied.

The best means for beginning the investigation of the quinary system would seem to be that of first studying the corresponding invariant points in the boundary quaternary systems. Some of these invariant points [4] were determined preliminary to the study of this quinary system. A small tetrahedron, 20 percent on a side, was chosen containing the compositions of these invariant points for the boundary quaternary systems, for example, T_1 and T_2, figure 1 [1]. For

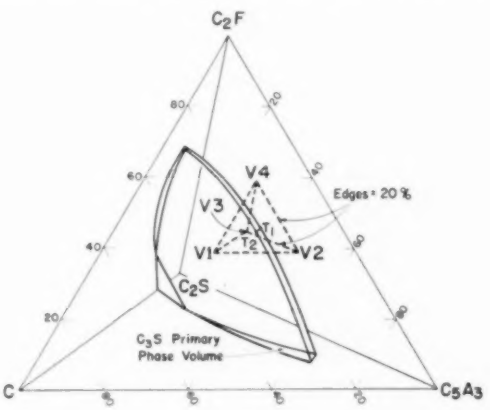

FIGURE 1. *Location of a small tetrahedron containing quaternary invariant points [1].*

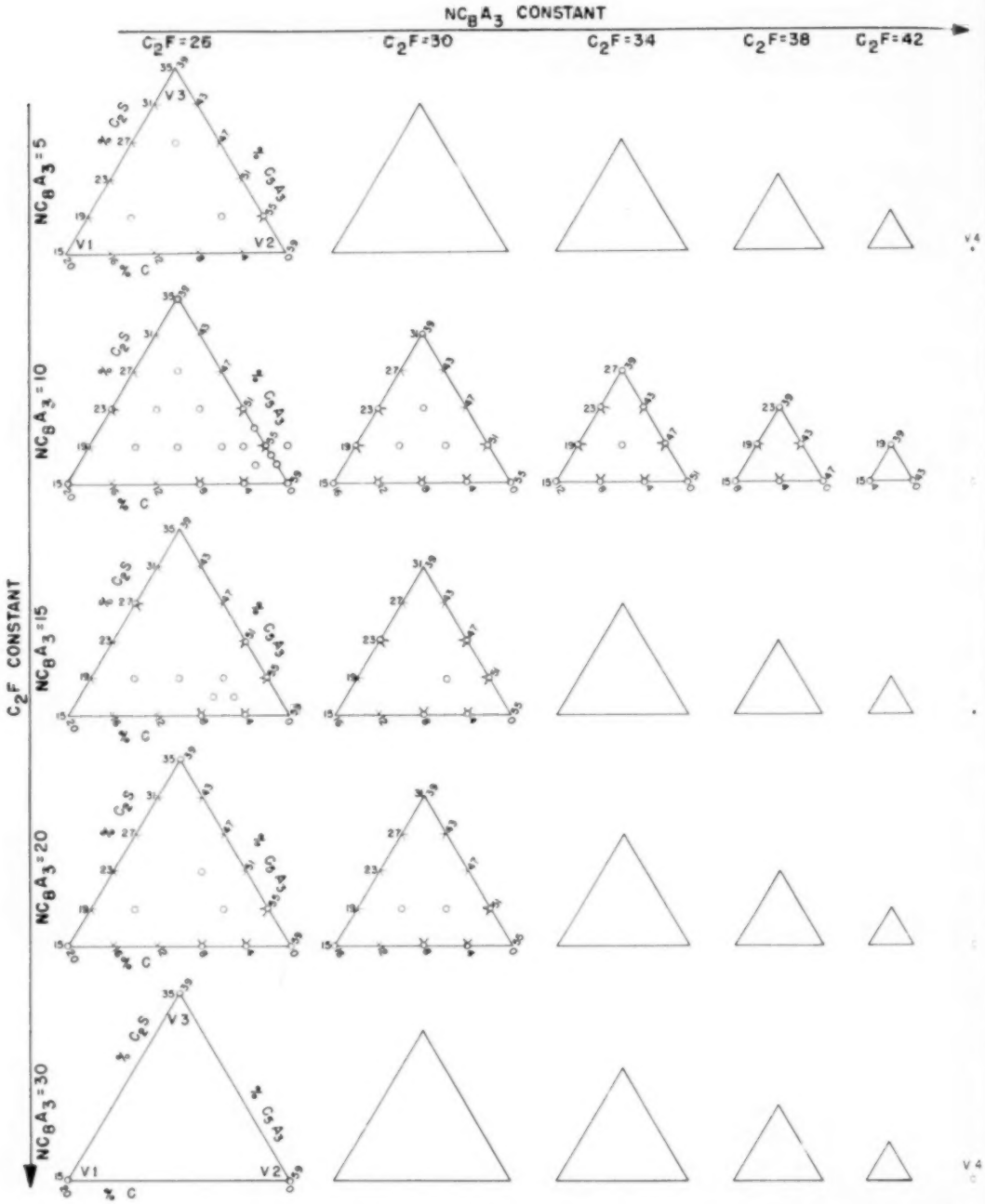

FIGURE 2. *Circled points represent compositions studied within the quinary system* NC_5A_3-C-C_5A_3-C_2F-C_2S.

Only NC_5A_3 is given as a quinary composition. The remaining four components are given as the quaternary components of figure 1. When X percent of NC_5A_3 was added, the percentage of each of the four quaternary components was multiplied by $(100-X)/100$ to bring all compositions within the quinary system. For example, a particular point in the 10 NC_5A_3-25 C_2F plane will contain 10 percent of NC_5A_3 0.90 × 25 percent of C_2F, and 0.90 × the percentages of the other three indicated in the triangular diagram.

points located in this tetrahedron, X percent of the fifth component would be added and $100-X$ percent taken of the remaining four. This would bring the compositions to be studied within the quinary system. Both oxide and compound compositions at the vertices of this small tetrahedron to which soda is to be added are given in the following tabulation.

Vertex	Oxide Composition,* Percent			
	CaO	Al_2O_3	SiO_2	Fe_2O_3
1	59. 15	20. 35	5. 23	15. 27
2	48. 72	30. 78	5. 23	15. 27
3	52. 17	20. 35	12. 21	15. 27
4	47. 40	20. 35	5. 23	27. 02
	Compound Composition, Percent			
	CaO	C_3A_3	C_2S	C_2F
1	20	39	15	26
2	0	59	15	26
3	0	39	35	26
4	0	39	15	46

* All compositions referred to in this work are given in weight percent.

Compositions in the quinary system may be followed by the two series of planes (triangular diagrams) shown in figure 2. In the first series the iron phase is allowed to vary, whereas in the second the soda phase is varied. In each particular plane both the iron phase and soda are maintained constant and the other three components allowed to vary. The composition melting at the lowest temperature in each plane locates a point on a bivariant surface in the quinary system. The locus of these points for each series of planes intersects a univariant curve. This intersection, usually a directional change point, may be located by plotting the various components or ratios of the components for a number of intersection points. It is not likely that this point of intersection will be on any plane chosen, but it will occur between planes and can thus be estimated by the extension of the curves. A number of these intersection points will define a univariant curve that may be followed to the invariant point.

Visualization of the relations between a large number of bivariant surfaces is limited by conventional three-dimensional representation. It is possible, however, to show diagrammatically the relations between such surfaces at a single invariant point, as is shown in figure 3. Five univariant curves meet at an invariant point. These are boundaries of the bivariant surfaces intersecting at that point. The number of curves and surfaces meeting at the invariant point and the number of solid phases represented for each meet the requirements of the phase rule for a

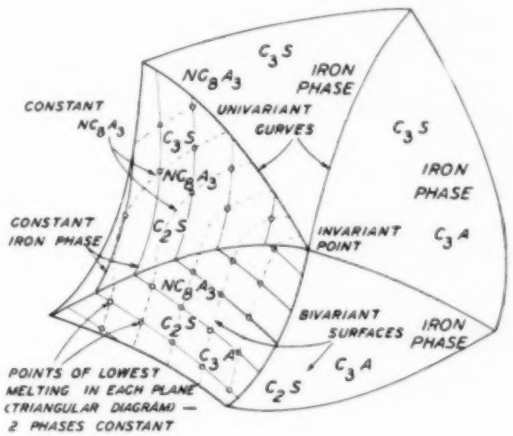

FIGURE 3. *Successive percentages of the iron phase are shown along the solid lines on the bivariant surface at the left.*

Successive percentages of the soda phase are represented by dashed lines. The intersections of these two sets of lines represent the composition point of the lowest temperature for complete melting determined for each plane when both the iron and soda phases were held constant. A univariant curve is the locus of points of directional change in the curves representing constant NC_8A_3 or constant iron phase. A univariant curve may then be followed to the quinary invariant point.

condensed system. Five solid phases are in equilibrium with liquid at the invariant point. Five univariant curves along which four solid phases are in equilibrium with liquid intersect at this point. Five bivariant surfaces on which three solid phases are in equilibrium with liquid meet at the invariant point. The volumes bounded by these surfaces may be considered trivariant with two solid phases in equilibrium with liquid. The tetravariant primary-phase regions for the five solid phases cannot be shown in a conventional space model. Phase-equilibrium relations at a quinary invariant point are pictured arbitrarily in figure 3.

Each triangle in figure 2 is analogous to a straight line in the space model of a quaternary system A-B-C-D, parallel to one of the edges, thus fixing the percentages of two of the components of the system. Such a line may be represented by two equations, for example, $A=5$ and $C=45$. It is apparent that the line may not intersect any univarant curve and that it will intersect a bivariant surface at only one point. Similarly, a quaternary system within a quinary system may be represented by an equation, and a ternary system within a quinary system may be represented by two equations. Interpretation of the data obtained from the triangles in figure 2 requires a knowledge of the manner in which invariant points, univariant curves, etc., in a quinary system appear in triangular diagrams. The following tabulation shows how these relations in a quinary system appear in a triangular diagram and a space model (tetrahedron), according to Dahl [10].

Geometric relations in quinary system	Tetravariant hypervolume	Trivariant volume	Divariant surface	Univariant curve	Invariant point
Number of solid phases in equilibrium with liquid and vapor	1	2	3	4	5
Intersections with triangular diagram	Area	Curve	Point	(a)	(b)
Intersections with space model	Volume	Surface	Curve	Point	(c)

a May appear as a point in the triangular diagram, but only when *both* of the two equations of the triangular diagram are satisfied by some point on the univariant curve. The point in the diagram then represents that particular point.

b May appear as a point in the triangular diagram, but only when *both* of the two equations of the triangular diagram are satisfied by the invariant point.

c May appear as a point in a space model, but only when the equation of the space model is satisfied by the invariant point.

2. Analytic Method

In representing phase-equilibrium relations of a quinary system within a triangular diagram or space model, conditions are imposed that indicate the manner in which compositions in these figures are different from all other compositions in the quinary system. A set of intrinsic equations, that is, equations involving components of a system and lacking a constant term, may be used to express these conditions. For example, in dealing with the system NC_8A_3-C-C_5A_3-C_2S-C_2F, it may be decided to work for a time with compositions limited to 10 percent of C_2F. A space model (tetrahedron) may be used to represent the composition relations under this condition, since the sum of the percentages of the remaining components is constant. The equation of the space model is $C_2F=10$. When the percentages of two of the components are fixed, for example if $C_2F=10$ and $NC_8A_3=5$, the sum of the remaining components is 85 percent, and relations between the remaining components may be shown in a triangular diagram.

Dahl has recently published a paper on the analytic treatment of multi-component systems using intrinsic equations [9]. This has been followed by another paper [8] on the properties and application of parametric equations. Dahl's equations are derived directly in terms of composition without considering geometric relations and may be applied to multi-component systems without the necessity of thinking in terms of hyperspace.

The number of intrinsic equations required to define a secondary system of m components in a primary system of N components is equal to the difference $N-m$. For example, a binary system is represented by a single equation when it is in a ternary system but requires three equations if it is in a quinary system. The number of terms that may appear in the equations also increases with the complexity of the system. A binary system within a quinary system may, however, be expressed by parametric equations using only one parameter. A ternary system requires two parameters, and so on. Parametric equations may therefore be used to define binary and ternary systems within a quinary system and intrinsic equations may be used in defining the more complicated quaternary systems within a quinary system. Thus, both types of equations may be employed in defining relations in a quinary system. The intrinsic equations may be set up in the manner of Dahl by using algebraic and determinant methods in connection with oxide or compound formulas and their molecular weights.

A parameter is introduced in order to express the composition of each component in terms of that variable. To define a system of m components in an N-component system, N parametric equations and $m-1$ parameters are required. To illustrate

Substitution of 23.4 and 10.0 for D_1 and E_1 ... of these points crosses a univariant curve, ...

he procedure as applied to systems requiring more than one parameter, the ternary system NC_3A_3-C_4AF-C_2S may be defined within the quinary system, N-C-A-F-S. The data needed are the compositions of the components of the ternary system as calculated from their molecular weights. Two parameters are required. This is illustrated in the following tabulation, in which the parameters are r and s. The weight fraction of NC_3A_3 is r, that of C_4AF is s, and that of C_2S is $1-r-s$. Thus, by varying r and s between 0 and 1, with $r+s$ not exceeding 1, compositions in any part of the ternary system NC_3A_3-C_4AF-C_2S within the quinary system N-C-A-F-S can be located and studied. The sum of the parametric expressions in the equations must be equal to 100 percent.

Primary component	NC_3A_3	C_4AF	C_2S	Parametric equation
	Percent	*Percent*	*Percent*	
N	7.6	.....	.....	$N=7.6r,$
C	54.9	46.2	73.7	$C=18.8r-27.5s+73.7,$
A	37.5	20.9	.....	$A=37.5+r20.9s,$
S	.....	.....	26.3	$S=26.3r-26.3s+26.3,$
F	.....	32.9	.....	$F=\quad 32.9s,$
Weight fraction	r	s	$(1-r-s)$	

Parametric equations may be used to trace compositions in planes within the quinary system. This serves the same purpose as the series of planes described in the graphic method, but without the necessity of considering geometric relations. For this study compositions in the quinary system are confined to a subordinate system in which the components are those at the vertices of the small tetrahedron in figure 1, with NC_3A_3 as the fifth component. The first step in the analytic method is to obtain parametric equations in which the percentage of each component of the quinary system is expressed in terms of weight fractions of components of the subordinate system. This is shown in the tabulation below.

Composition points of subordinate system	A	B	C	D	E	Weight fraction
	CaO	C_2S	C_3A_3	C_2F	NC_3A_3	
	%	%	%	%	%	
V1	20	15	39	26	0	r
V2	0	15	59	26	0	w
V3	0	35	39	26	0	x
V4	0	15	39	46	0	y
V5	0	0	0	0	100	$1-r-w-x-y$

Equations for the quinary system are:

$$A = \quad 20r, \tag{1}$$

$$B = \quad 15r + 15w + 35x + 15y, \tag{2}$$

$$C = \quad 39r + 59w + 39x + 39y, \tag{3}$$

$$D = \quad 26r + 26w + 26x + 46y, \tag{4}$$

$$E = -160r - 100w - 100x - 100y + 100. \tag{5}$$

Parametric equations for a ternary system (triangular diagram) require only two parameters, and the second step is to eliminate two of the parameters in eq 1 to 5. These parameters may be selected arbitrarily, and in this case x and y are chosen. Since C_2F and NC_3A_3 are to be maintained constant in each triangle, as in figure 2, it will be assumed that D and E are equal to the constants D_1 and E_1, respectively. Transposing eq 4 and 5, and simplifying, the following equations are obtained:

$$26x + 46y = D_1 - 26r - 26w, \tag{4a}$$

$$x + \quad y = -0.01E_1 - r - w + 1. \tag{5a}$$

Solving for x and y,

$$x = -0.05D_1 - 0.023E_1 - r - w + 2.3, \tag{6}$$

$$y = \quad 0.05D_1 + 0.013E_1 \qquad - 1.3. \tag{7}$$

Substituting in eq 1 to 3,

$$A = \quad 20r \tag{8}$$

$$B = -20r - 20w + 0.61(100 - E_1) - D_1, \tag{9}$$

$$C = \qquad 20w + 0.39(100 - E). \tag{10}$$

Upon substituting in eq 8 to 10, the values of D_1 and E_1 to be maintained constant in any given triangle, equations for A, B, and C will be obtained in terms of the parameters r and w. For example, if D_1 and E_1 (that is, C_2F and NC_3A_3) are to be given the values 23.4 and 10.0 percent, respectively, substitution of these values in eq 8 to 10 yields the following equations for compositions in the triangle.

$$A = \quad 20r, \tag{8a}$$

$$B = -20r - 20w + 31.5, \tag{9a}$$

$$C = \qquad 20w + 35.1. \tag{10a}$$

TABLE 2. *Quenching data on quaternary invariant-point compositions with and without addition of soda*

Substitution of 23.4 and 10.0 for D_1 and E_1, respectively, in eq 6 leads to the equation,

$$x=0.9-v-w.$$

Since the weight fractions of the subordinate components cannot be negative, $(v+w)$ in the triangle under consideration cannot exceed 0.9.

Thus, by varying the weight fractions v and w, within the limits specified, any composition of the ternary system in which $D=23.4$ and $E=10$ within the quinary system may be obtained. For example, the test composition 10N26F5, discussed later and given in table 4, is located within this plane when $v=0$ and $w=0.72$ and can then be studied. Additional parametric equations for other planes and points within planes may be found in a similar manner. The lowest melting composition for each plane is then determined experimentally. As described earlier, the locus of these points crosses a univariant curve, which may then be traced to the invariant point.

V. Results

The compositions studied by use of the graphical method are indicated by the circled points in the two series of triangular diagrams given in figure. These compositions, along with the quenching data and the results of petrographic examination are given in tables 2 through 4. Only the data necessary to locate the liquidus or to identify both primary and secondary phases are presented. For many compositions only one quench was required when it was obvious that the liquidus temperature was increasing, i. e., compositions were getting farther from the invariant point. In these cases the appearance of primary and secondary phases was more important than the location of the exact liquidus temperature.

TABLE 1. *Invariant points for systems bounding the quinary system* NC_3A_2-C-C_3A_2-C_2F-C_2S

System [a]	Investigator and reference	Temperature	Percent composition				
			Na_2O	CaO	Al_2O_3	SiO_2	Fe_2O_3
C-C_3A_2-C_4AF-C_2S:		°C					
C_2S, C_3A, F *ss*, C_2S and liquid	Lea and Parker [1]	1,338	0	54.8	22.7	6.0	16.5
C, C_3A, F *ss*, C_2S and liquid		1,341	0	55.0	22.7	5.8	16.5
C-C_3A_2-C_2F-C_2S:							
C_3A, C_2F, C_2S, C_3S, liquid	Swayze [2]	1,338	0	53.5	22.3	6.0	18.2
C, C_3A, C_2F, C_2S, liquid		1,342	0	53.9	21.2	5.8	19.1
NA-C-A-C_2S:							
NC_3A_2, C_3A, C_2S, C_3S liquid	Greene and Bogue [3]	1,440	3.5	55.2	31.0	10.3	0
NC_3A_2, C, C_3A, C_2S, liquid		1,442	3.5	56.0	31.0	9.5	0
NC_3A_2, C, C_2S, C_2S, liquid		1,445	5.0	54.1	28.6	12.3	0
(NA_2)-C-C_4AF:							
NC_3A_2, C_2A_3, F *ss*, liquid	Eubank and Bogue [4]	1,344	4.7	44.0	34.2	0	17.1
NC_3A_2, C, F *ss*, liquid		1,390	2.5	48.4	26.8	0	22.3
N-C-C_2F-C_2S	Eubank and Bogue [4]	No ternary compounds found in compositions up to 5% Na_2O					

[a] For convenience the otherwise cumbersome formulas of the compounds encountered in this investigation are given the following abbreviated form: N = Na_2O, C = CaO, A = Al_2O_3, F = Fe_2O_3, and S = SiO_2. Thus NC_3A_2 = $Na_2O.8CaO.3Al_2O_3$, etc.

TABLE 2. *Quenching data on quaternary invariant-point compositions with and without addition of soda*

Test No.	Temperature	Method of quenching	Quench liquid	Phases observed
Point T_1 of Lea and Parker [1]. CaO 55.0, Al_2O_3 22.7, SiO_2 5.8, Fe_2O_3 16.5				
	°C			
T5	1,342	Open pan	Water	CaO, F *ss* in glass.
T8	1,345	do	Liquid air	CaO, C_2S, F *ss* in glass.
T11	1,347	Small envelope	Water	CaO, C_2S in glass.
T6	1,347	Open pan	do	CaO, F *ss* in glass.
T9	1,348	do	Liquid air	CaO in glass.
T7	1,352	do	Water	All glass.
T12	1,352	Small envelope	do	Do.
T10	1,353	Open pan	Liquid air	Do.
Point 1 of Swayze [2]. CaO 53.9, Al_2O_3 21.2, SiO_2 5.8, Fe_2O_3 19.1				
S5	1,345	Open pan	Water	C_2S, F *ss*, trace CaO in glass.
S7	1,348	Small envelope	Liquid air	F *ss*, C_2S in glass.
S9	1,348	do	Water	Do.
S8	1,354	do	Liquid air	All glass.
S10	1,354	do	Water	Do.
S6	1,355	Open pan	do	Do.
Point 1 of Swayze plus 2% Na_2O *				
S11	1,377	Small envelope	Water	Small amount CaO in glass.
S12	1,397	do	do	Do.
S13	1,409	do	do	All glass.
Point 1 of Swayze plus 4% Na_2O *				
S14	1,377	Small envelope	Water	Small amount CaO in glass.
S15	1,387	do	do	Do.
S16	1,405	do	do	All glass.

Point 2 of Swayze plus NC_3A_2 *

No.	CaO	C_3A_2	C_2S	C_2F	NC_3A_2	Temperature	Phases observed
						°C	
10NS2-1	8.1	38.4	15.5	27.9	10.0	1,325	Small crystals F *ss* in glass.
20NS2-1	7.2	34.2	13.8	24.8	20.0	1,325	Do.
Additions of NC_3A_2; NC_3A_2 subtracted from C_3A_2							
10NS2-2	9.1	32.7	17.2	31.0	10.0	1,330	Little glass, small crystals unreacted compounds.
20NS2-2	9.1	22.7	17.2	31.0	20.0	1,330	Small amounts F *ss*, C_3A, CaO in glass.
30NS2-1	9.1	12.7	17.2	31.0	30.0	1,330	Much CaO, traces F *ss* in glass.
40NS2-1	9.1	2.7	17.2	31.0	40.0	1,330	More CaO, F *ss* in glass.

* When x% of soda phase was added, $(100-x)$% of each constituent of the quaternary composition point was taken. Unless otherwise stated, all quenches were made in small platinum envelopes into water.

TABLE 3. *Quenching data on boundaries of the small tetrahedron figure 1, with and without additions of soda*

Test No.[a]	Compound composition					Temperature	Petrographic examination
	C_3O	C_3A_3	C_2S	C_2F	NC_8A_3		
	Percent	*Percent*	*Percent*	*Percent*	*Percent*	° *C*	
V1-1	20	39	15	26		1,399	Large amounts free CaO in glass.
-2						1,435	Do.
-3						1,501	Considerable free CaO in glass.
-4						1,521	Small amounts free CaO in glass.
V2-1	0	59	15	26		1,312	C_3A,F *ss*—composition gradients in glass.
-2						1,325	Small amount C_3A,F *ss* in glass.
-3						1,345	Traces F *ss* in glass.
-4						1,365	All glass.
V3-1	0	39	35	26		1,350	Small crystals C_2S, F *ss* in glass.
-2						1,362	Do.
-3						1,380	Traces crystals C_2S,F *ss* in glass.
-4						1,392	All glass.
V4-1	0	39	15	46		1,353	Large amounts F *ss* in glass.
-2						1,366	Considerable F *ss* in glass.
-3						1,375	All glass.
	Vertex composition						
	V1	V2	V3	V4			
	Percent	*Percent*	*Percent*	*Percent*	*Percent*		
123V -1	33.3	33.3	33.3			1,378	Small crystals C_2S in glass.
-2						1,401	Do.
-3						1,412	Traces C_2S in glass.
124V -1	33.3	33.3		33.3		1,347	Many F *ss* crystals in glass.
-2						1,358	Traces F *ss* crystals in glass.
-3						1,368	All glass.
134V -1	33.3		33.3	33.3		1,375	F *ss*, protected phases, C_2S in glass.
-2						1,406	Traces C_2S in glass.
234V -1		33.3	33.3	33.3		1,378	Do.
10V2-1		90			10	1,334	Traces C_3A and F *ss* in glass.
-2						1,345	All glass.
20V2-1		80			20	1,345	Small amount C_3A in glass.
-2						1,358	Traces C_3A in glass.
30V2-1		70			30	1,359	NC_8A_3,C_2S in glass.
-2						1,382	NC_8A_3,C_3A in glass.
50V2-1		50			50	1,359	NC_8A_3,C_3A in glass.
-2						1,382	Large crystals NC_8A_3 in glass.
10V3			90		10	1,411	Many rounded grains NC_8A_3, C_2S in glass.
20V3			80		20	1,409	C_2S in glass.
30V3			70		30	1,407	Traces NC_8A_3 in glass.
10V4-1				90	10	1,360	Small crystals F *ss*, C_3A in glass.
-2						1,375	All glass.
20V4				80	20	1,360	Traces F *ss* in glass.
30V4-1				70	30	1,355	Large crystals F *ss*, C_3A in glass.
-2						1,375	All glass.

[a] V refers to the vertices of the small tetrahedron of figure 1.

TABLE 4. *Quenching data on planes (fig. 2) within the quinary system*

Test No.	Percent composition					Temperature	Petrographic examination
	C_3O	C_3A_3	C_2S	C_2F	NC_8A_3		
						°C	
F%, NC_8A_3* 20% C_2F plane							
10N26F1	10.8	38.7	17.1	23.4	10.0	1,390	Many free CaO grains in glass.
10N26F2-1	3.6	45.9	17.1	23.4	10.0	1,332	C_3A, NC_8A_3,F *ss* in glass.
-2						1,342	All glass.
10N26F3	3.6	38.7	24.3	23.4	10.0	1,360	Many small rounded grains C_2S, NC_8A_3 in glass.
10N26F4	3.6	40.5	13.5	23.4	10.0	1,342	Small amounts C_3A, traces NC_8A_3 in glass.
10N26F5-1	0	49.5	17.1	23.4	10.0	1,310	F *ss*, C_2S, NC_8A_3 in glass.
-2						1,316	Small amounts F *ss*, C_2S, NC_8A_3 in glass.
-3						1,320	All glass.
10N26F6	7.2	45.9	13.5	23.4	10.0	1,342	NC_8A_3 in glass.
10N26F7-1	0	45.9	20.7	23.4	10.0	1,336	Do.
-2						1,342	Small amount NC_8A_3 in glass.
10N26F8	1.8	47.7	17.1	23.4	10.0	1,320	C_2S,NC_8A_3, F *ss* in glass.
10N26F9	0	51.3	15.3	23.4	10.0	1,320	Small amount F *ss* in glass.
10N26F10	1.8	49.5	15.3	23.4	10.0	1,320	F *ss*, C_3A,NC_8A_3 in glass.
10N26F11	.9	50.4	15.3	23.4	10.0	1,320	F *ss* in glass.
10N26F12	7.2	38.7	20.7	23.4	10.0	1,353	Many small crystals C_2S, NC_8A_3, C_3S in glass.
10N26F13	3.6	42.3	20.7	23.4	10.0	1,353	Many small crystals C_2S, NC_8A_3, more glass.
10N26F14	7.2	42.3	17.1	23.4	10.0	1,353	Small amount C_3A in glass.
10N26F15	10.8	35.1	20.7	23.4	10.0	1,331	Large amount C_3A, fine crystals F ss in glass.
10N26F16	0	50.4	16.2	23.4	10.0	1,330	Small amounts C_3A, F *ss*, NC_8A_3 in glass.
10% NC_8A_3, 30% C_2F plane							
10N30F1	3.6	45.9	13.5	27.0	10.0	1,320	Many crystals F *ss*, C_3A, traces NC_8A_3 in glass.
10N30F2	0	49.5	13.5	27.0	10.0	1,320	Many crystals F *ss*, traces C_2S, NC_8A_3 in glass.
10N30F3	3.6	42.3	17.1	27.0	10.0	1,322	F *ss*, C_3A, small amounts C_2S, NC_8A_3 in glass.
10N30F4	0	45.9	17.1	27.0	10.0	1,322	Small amounts F *ss*, C_2S, NC_8A_3 in glass.
10N30F5	7.2	38.7	17.1	27.0	10.0	1,336	Traces C_3A in glass
10N30F6	3.6	38.7	20.7	27.0	10.0	1,336	Large grains C_2S in glass.
10N30F7	14.4	35.1	13.5	27.0	10.0	1,320	Some glass, quench growths, unreacted materials.
10N30F8	0	35.1	27.9	27.0	10.0	1,320	Many F *ss*, C_2S, NC_8A_3 crystals in glass.
10N30F9	7.2	35.1	20.7	27.0	10.0	1,330	C_3A, fine quench growths in glass.
10N20F10	10.8	35.1	17.1	27.0	10.0	1,331	Many crystals C_3A, F *ss* in glass.
10N30F11	10.8	38.7	13.5	27.0	10.0	1,331	Many crystals C_3A, F *ss* in glass.
10N30F12	7.2	42.3	13.5	27.0	10.0	1,331	Many crystals C_3A, F *ss* in glass.
10% NC_8A_3, 34% C_2F plane							
10N34F1	10.8	35.1	13.5	30.6	10.0	1,320	Small crystals F *ss*, C_2S, NC_8A_3, little glass.
10N34F2	0	45.9	13.5	30.6	10.0	1,320	Many F *ss* crystals in glass.
10N34F3	0	35.1	24.3	30.6	10.0	1,320	C_2S, C_3S, F *ss* in glass.
10N34F4	3.6	38.7	17.1	30.6	10.0	1,320	F *ss*, C_2S, C_3A in glass.
10N34F5	3.6	35.1	20.7	30.6	10.0	1,323	F *ss*, C_2S in glass.
10N34F6	7.2	35.1	17.1	30.6	10.0	1,323	Many crystals F *ss*, small amounts C_2S, C_3A, NC_8A_3 in glass.
10N34F7	7.2	38.7	13.5	30.6	10.0	1,331	Small crystals F *ss*, C_3A in glass.
10N34F8	3.6	42.3	13.5	30.6	10.0	1,331	Traces F *ss*, C_3A, mostly glass.
10N34F9	0	42.3	17.1	30.6	10.0	1,332	Small amount F *ss* traces C_3A mostly glass.
10N34F10	0	38.7	20.7	30.6	10.0	1,332	Several crystals F *ss*, C_2S, traces NC_8A_3 in glass.

* When X% of soda phase was added, (100−X)% of each constituent of the quaternary composition point was taken.

TABLE 4. *Quenching data on planes (fig. 2) within the quinary system*—Continued

Test No.	Percent composition					Temperature	Petrographic examination
	CaO	C_3A_3	C_2S	C_2F	NC_8A_3		
				10% NC_8A_3, 38% C_2F plane			
10N38F1	7.2	35.1	13.5	34.2	10.0	1,328	Many small crystals F *ss*, few large crystals C_3A in glass.
10N38F2	0.0	42.3	13.5	34.2	10.0	1,328	Many crystals F *ss*, traces free CaO in glass.
10N38F3	.0	35.1	20.7	34.2	10.0	1,330	Several crystals F *ss*, C_2S, NC_8A_3 in glass.
10N38F4	3.6	35.1	17.1	34.2	10.0	1,330	Several crystals F *ss*, C_2S, NC_8A_3 in glass.
10N38F5	0.0	38.7	17.1	34.2	10.0	1,330	Many crystals F *ss*, some C_2S, small amounts NC_8A_3 in glass.
10N38F6	3.6	38.7	13.5	34.2	10.0	1,330	Many crystals F *ss*, some large crystals C_3A, C_2S (twinned) in glass.
				10% NC_8A_3, 42% C_2F plane			
10N42F1	3.6	35.1	13.5	37.8	10.0	1,331	Small crystals F *ss*, small amounts C_2S, NC_8A_3 in glass.
10N42F2	0.0	38.7	13.5	37.8	10.0	1,331	Small crystals F *ss*, small amounts C_2S, NC_8A_3 in glass.
10N42F3	.0	35.1	17.1	37.8	10.0	1,330	Small crystals F *ss*, small amounts C_2S, NC_8A_3 in glass.
				5% NC_8A_3, 26% C_2F plane			
5N26F1	11.6	40.8	18.0	24.7	5.0	1,342	Free CaO, NC_8A_3 in glass.
5N26F2-1	3.8	48.4	18.0	24.7	5.0	1,342	NC_8A_3 in glass.
-2						1,355	All glass.
5N26F3	3.8	40.8	25.6	24.7	5.0	1,363	Many crystals NC_8A_3, C_2S in glass.
5N26F5-1	0.0	52.2	18.1	24.7	5.0	1,321	Many crystals F *ss*, C_2S, NC_8A_3 in glass.
						1,332	All glass.
				10% NC_8A_3, 22% C_2F plane			
10N22F1	3.6	49.5	17.1	19.8	10.0	1,320	Many crystals C_3A, C_2S in glass, small amounts NC_8A_3 and F *ss*.
10N22F2	0.0	53.1	17.1	19.8	10.0	1,320	Traces C_2S in glass.
10N22F3	.0	49.5	20.7	19.8	10.0	1,321	Several crystals C_2S, some NC_8A_3 in glass.
10N22F4	3.6	53.1	13.5	19.8	10.0	1,320	Many crystals C_3A, some F *ss*, traces NC_8A_3, C_3A_3 in glass.
				15% NC_8A_3, 26% C_2F plane			
15N26F1	0.0	43.4	19.5	22.1	15.0	1,320	C_2S, NC_8A_3 in glass.
15N26F2	6.8	43.4	12.7	22.1	15.0	1,320	NC_8A_3,C_3A in glass.
15N26F3	3.4	43.4	16.1	22.1	15.0	1,318	Small amounts NC_8A_3,C_3A,C_2S,F *ss* in glass.
15N26F4	6.8	40.0	16.1	22.1	15.0	1,318	Small amounts NC_8A_3,C_2S,F *ss* in glass.
15N26F5	0.0	46.8	16.1	22.1	15.0	1,321	NC_8A_3,C_3A,C_2S in glass.
15N26F6	3.4	45.1	14.5	22.1	15.0	1,321	Do.
15N26F7	5.1	43.4	14.5	22.1	15.0	1,323	Do.
15N26F8	3.4	46.8	12.7	22.1	15.0	1,323	Do.
15N26F9	6.8	39.2	22.9	22.1	15.0	1,330	C_2S,C_2S,NC_8A_3 in glass.
15N26F10	10.2	36.6	16.1	22.1	15.0	1,330	Free CaO,NC_8A_3, in glass.

TABLE 4. *Quenching data on planes (fig. 2) within the quinary system*—Continued

Test No.	Percent composition					Temperature	Petrographic examination
	CaO	C_3A_3	C_2S	C_2F	NC_8A_3		
				15% NC_8A_3, 30% C_2F plane			
15N30F1	0.0	43.4	16.1	25.5	15.0	1,330	Small amounts F *ss*, NC_8A_3 in glass.
15N30F2	3.4	43.4	12.7	25.5	15.0	1,330	Do.
15N30F3	3.4	40.0	16.1	25.5	15.0	1,330	Do
15N30F4	6.8	33.2	19.5	25.5	15.0	1,330	F *ss*, C_2S in glass.
15N30F5	0.0	40.0	19.5	25.5	15.0	1,330	Do.
15N30F6	6.8	40.0	12.7	25.5	15.0	1,330	F *ss*, NC_8A_3 in glass.
				20% NC_8A_3, 20% C_2F plane			
20N26F1	9.6	34.4	15.2	20.8	20.0	1,330	NC_8A_3,free CaO,C_3A in glass.
20N26F2	3.2	40.8	15.2	20.8	20.0	1,330	NC_8A_3,C_3A in glass.
20N26F3	3.2	34.4	21.6	20.8	20.0	1,330	C_2S,C_3S,NC_8A_3 in glass.
20N26F4	3.2	44.0	12.0	20.8	20.0	1,330	NC_8A_3,C_3A in glass.
20N26F5	0.0	44.0	15.2	20.8	20.0	1,330	Do.
20N26F6	6.4	40.8	12.0	20.8	20.0	1,330	Do.
				20% NC_8A_3, 30% C_2F plane			
20N30F1	6.4	34.4	15.2	24.0	20.0	1,330	Large crystals F *ss*, C_3A, traces C_2S, NC_8A_3 in glass.
20N30F2	6.4	37.6	12.0	24.0	20.0	1,330	Large amounts C_3A,small amounts F *ss*, traces NC_8A_3 in glass.
20N30F3	3.2	37.6	15.2	24.0	20.0	1,330	Do.
20N30F4	0.0	40.8	15.2	24.0	20.0	1,330	Do.
20N30F5	9.6	31.2	15.2	24.0	20.0	1,330	Considerable C_3A,F *ss* in glass.
20N30F6	12.8	28.0	15.2	24.0	20.0	1,330	Do.

The procedure for locating invariant points within the quinary system may be followed systematically by reference to the above mentioned figure and tables. Selection of a small tetrahedron to which the fifth component, the soda phase, was to be added, was made by studying the relations in the boundary systems as discussed in conjunction with figure 1.

Invariant points for the soda-free quaternary system have been reported by other investigators [1, 2]. Lea and Parker's point T_1 and Swayze's point 1 were reported as invariant points at which CaO, C_3S, C_3A, and iron phase are in equilibrium with liquid. Compositions for point T_1 and point 1 were investigated by the quenching methods described earlier, table 2. The observed liquidus temperature was 1,350° C for each of these compositions. This is higher than the 1,341° reported by Lea and Parker for composition T_1 and the 1,342° reported by Swayze for point 1. It is likely that these departures from the published data result from differences in the impurities of the reagents used by the several investigators. Since such variations produce slight changes in composition, the liquidus temperature obtained by the present author in the quaternary system cannot be assumed to be the liquidus temperature of the true invariant-point composition.

The effect of soda in the forms of the oxide and the compound NC_8A_3 on this liquidus temperature is worthy of note, table 2. Additions of 2 and 4 percent of Na_2O raised the liquidus temperature above 1,400°, an increase of more than 50 deg. On the other hand, when soda was added in the form of NC_8A_3 (10 to 20%), the stable soda phase in clinker, the liquidus was lowered about 20 deg. to 1,330°. The addition of Na_2O in the form of the oxide causes extensive changes in the potential compound composition of the mixture, through formation of NC_8A_3. The effect of the addition of Na_2O in the form of the oxide cannot therefore be readily interpreted. It is preferable to add

Na_2O in the form of NC_8A_3, and this practice was followed in the remainder of the investigation.

The vertices of the small tetrahedron with additions of the soda phase were studied first, see table 3 and figure 2. It was found that those compositions obtained by adding NC_8A_3 to vertices *V2* and *V4*, representing higher concentrations of C_3A_3 and C_2F, respectively, melted at lower temperatures than the other two. Actually, compositions obtained by adding NC_8A_3 to vertex *V1*, higher CaO content, contained free CaO even when heated above 1,550°.

The centers of the faces of the tetrahedron were next studied. These compositions were prepared by mixing equal weight proportions of three vertex compositions. The center of the *V1–V2–V4* face had the lowest melting temperature.

When 10 to 30 percent of NC_8A_3 was added to each of the *V2*, *V3*, and *V4* vertex compositions the liquidus temperature was increased except in the case of the 10-percent addition to vertex *V2*, which reduced the liquidus temperature to 1,339°.

Having studied the boundaries of the small tetrahedron with and without additions of soda, planes within the tetrahedron were selected (fig. 2). To points within the tetrahedron representing quaternary compositions, *x* percent of the soda phase was added, and 100— *x* percent of the amount of each of the four quaternary constituents making up this point was taken. In the plane studied, 10 percent of NC_8A_3 was added, and the C_2F was held constant at 26 percent (quaternary composition). The remaining three components were then allowed to vary. The lowest melting composition in this plane, 10N26F5 [6] listed in table 4, was found to be all liquid at 1,318°. The iron phase appeared to be the primary phase. At only 2 deg. below this liquidus temperature, however, three solid phases were in equilibrium with liquid. This point, then, is on a bivariant surface in the quinary system and is probably near a univariant curve that extends to the invariant point. It is unusual that the first plane studied should be so close to the invariant point.

The next plane considered, 10 percent of NC_8A_3 and 30 percent of C_2F, contained no composition melting as low as the composition indicated by 10N26F5 in the previous plane. The iron phase appeared in larger quantities. A fe points in the $10NC_8A_3$-$34C_2F$, $10NC_8A_3$-$38C_2$ and $10NC_8A_3$-$42C_2F$ planes were studied to com plete the series, but none of them melted as lo as 1,318°. The plane $10NC_8A_3$-$22C_2F$ was als studied. Quenched charges in this plane co tained the iron phase in small quantities but on as a secondary phase. This indicated that th invariant-point composition was at a higher val of C_2F, that is, between 22 and 26 percent C_2F (quaternary composition).

In the next series of planes the iron phase wa held constant, and the soda phase varied from to 30 percent (quinary composition). In th $5NC_8A_3$-$26C_2F$ plane, NC_8A_3 did not appear a the primary phase, and the minimum liquidu temperature was again higher than that for th $10NC_8A_3$-$26C_2F$ plane.

The $20NC_8A_3$-$26C_2F$ plane was likewise at higher liquidus temperature but contained NC_8A_3 as the primary phase. Compositions in th $20NC_8A_3$-$30C_2F$ plane were studied. At this C_2F concentration (24% in the quinary system) *F ss* and C_3A appeared as the predominan phases. Compositions of minimum liquidus tem perature in this plane were still further remove from the invariant point. Therefore, the in variant point would appear to contain less than 2 percent of NC_8A_3 and near 26 percent (23.4% in the quinary system) of C_2F.

The 15 percent NC_8A_3—26 percent C_2F plan was then studied. The temperature found fo the point of lowest melting, 1,320°, was somewha lower than that found in other planes, with th exception of the $10NC_8A_3$-$26C_2F$ plane. *F ss* did not appear as a primary phase (22.1% of C_2F in the quinary system). The primary phase in the compositions melting at lower temperature was NC_8A_3.

A few points were studied in the $15NC_8A_3$-$30C_2F$ plane. At this C_2F concentration (25.5% in the quinary system) *F ss* was the primary phase indicating an excess of C_2F.

From the information gained in the study of these planes, additional compositions were chosen for study. These points are not shown in figure 2 but are given, together with petrographic observations of the quenched charges, in table 5.

These data indicated that the invariant point should contain less C_2F, more NC_8A_3, and more SiO_2 than point 10N26F5 in the $10NC_8A_3$-$26C_2F$

[6] For convenience and economy of space, the test number designation is used in place of the more complete form, for example, 10N=10 percent of NC_8A_3, and 26F=26 percent of C_2F, and 5=the fifth composition studied in this plane.

TABLE 5. *Quenching data on intermediate planes within the quinary system*

Test No.	Percent Composition					Temperature	Petrographic examination
	C_3O	C_3A_3	SiO_2	C_2F	NC_8A_3		
NC_8A_3 and C_3A_3 varied							
						°C	
10N1	7.0	53.5	6.5	23.0	10.0	1,318	Small amounts C_3A, C_2S, F *ss* in glass.
12N1-1	7.0	51.5	6.5	23.0	12.0	1,314	Small amounts C_2S, C_3A, F *ss* in glass.
-2						1,318	All glass.
14N1-1	7.0	49.5	6.5	23.0	14.0	1,314	Traces NC_8A_3, C_2S, C_2S, C_3A in glass.
-2						1,318	All glass.
16N1	7.0	47.5	6.5	23.0	16.0	1,319	Small amounts NC_8A_3, C_2S, F *ss* in glass.
18N1	7.0	45.5	6.5	23.0	18.0	1,318	Do.
20N1	7.0	43.5	6.5	23.0	20.0	1,320	Do.
NC_8A_3 and CaO varied							
10N2	10.5	50.0	6.5	23.0	10.0	1,318	C_3A, F *ss*, C_2S in glass
12N2	8.5	50.0	6.5	23.0	12.0	1,318	Do.
14N2-1	6.5	50.0	6.5	23.0	14.0	1,314	NC_8A_3, C_2S, C_3A, F *ss* in glass.
-2						1,318	All glass.
16N2	4.5	50.0	6.5	23.0	16.0	1,318	NC_8A_3, F *ss*, C_3A in glass.
18N2	2.5	50.0	6.5	23.0	18.0	1,320	C_3A, NC_8A_3, F *ss* in glass.
CaO and C_3A_3 varied							
13N1	14.0	43.0	6.5	23.0	13.5	1,330	C_2S, C_3S in glass.
13N2	12.0	45.0	6.5	23.0	13.5	1,330	Do.
13N3-1	10.0	47.0	6.5	23.0	13.5	1,320	Traces F *ss*, C_2S in glass.
-2						1,329	All glass.
13N4-1	8.0	49.0	6.5	23.0	13.5	1,315	Small amounts F *ss*, NC_8A_3, C_2S, C_3S in glass.
-2						1,320	All glass.
13N5-1	6.0	51.0	6.5	23.0	13.5	1,315	Small amounts C_2S, C_3A, NC_8A_3, F *ss* in glass.
-2						1,320	All glass.
13N6-1	4.0	53.0	6.5	23.0	13.5	1,315	C_3A, NC_8A_3, F *ss* in glass.
-2						1,320	Traces C_3A in glass.
13N7-1	2.0	55.0	6.5	23.0	13.5	1,320	F *ss*, C_3A, traces C_3A_3 in glass.
13N8-1	0	57.0	6.5	23.0	13.5	1,320	C_3A_3, C_3A in glass.
C_2F and SiO_2 varied							
13N9	7.0	50.0	5.5	24.0	13.5	1,315	Traces F *ss*, C_3A in glass.
13N10-1	7.0	50.0	6.5	23.0	13.5	1,310	Traces NC_8A_3, C_3A, C_2S, C_3S, F *ss* in glass.
-2						1,312	All glass.
13N11	7.0	50.0	7.5	22.0	13.5	1,317	Small amounts C_2S, C_3S, C_3A in glass.
13N12	7.0	50.0	8.5	21.0	13.5	1,317	Many fine crystals C_2S, C_3S, NC_8A_3 in glass.
13N13	7.0	50.0	9.5	20.0	13.5	1,317	Do.

plane. Consequently, NC_8A_3 was varied from 10 to 20 percent in two series of compositions. In both series SiO_2 and C_2F were held constant at 6.5 and 23.0 percent, respectively (quinary composition). In the first series CaO was also held constant at 7.0 percent and C_5A_3 and NC_8A_3 varied, the sum of the latter two being constant. In the second series C_5A_3 was held constant at 50.0 percent, and CaO and NC_8A_3 varied with their sum constant.

Similar results were obtained for each series. The minimum temperature for complete melting (1,316°) appeared at slightly less NC_8A_3 content than that for two 14-percent NC_8A_3 compositions included in the preceding paragraph. This temperature is lower than that of any composition previously studied.

From these data it was deduced that the NC_8A_3 value for the invariant point was near 13.5 percent. Because of this, another series of compositions (table 5) was prepared containing 13.5 NC_8A_3, 6.5 SiO_2, and 23.0 percent of C_2F, and varying amounts of C_5A_3 and CaO. The lowest temperature for complete melting appeared between points containing 8.0 CaO and 49.0 percent C_5A_3 and 6.0 CaO and 51.0 percent C_5A_3. Slightly below the liquidus temperature four solid phases were in equilibrium with liqui indicating that the compositions were on un variant curves near the invariant point.

The final series was prepared to contain th composition midway between these points. C_2F and SiO_2 were varied, and the other three compo nents held constant. This intermediate com position, 13N10, melted at 1,312°. At 1,310° four and possibly five solid phases were observed in equilibrium with liquid. These crystalline phases in a glassy matrix are shown in figure 4 at a magnification of 470 diameters. The same field is shown both with and without crossed nicols.

The lower part of the field consists of a large isotropic crystal of C_3A (phase 1, fig. 4, A) having a refractive index slightly below that of the mount ing medium (1.715). It contains a few dark in clusions and extinguishes under crossed nicols (fig. 4, B). Near the upper part of the field a few small crystals of C_3A also appear. The iron-containing solid solution, F*ss*, phase 2, has much higher refractive indices than either the glassy matrix or the mounting medium and is in high relief. It is colored brownish-red to tan showing pleochroism and under crossed nicols gives high-order interference colors with red being predominant. Phase 3 is C_2S, which appears near the left

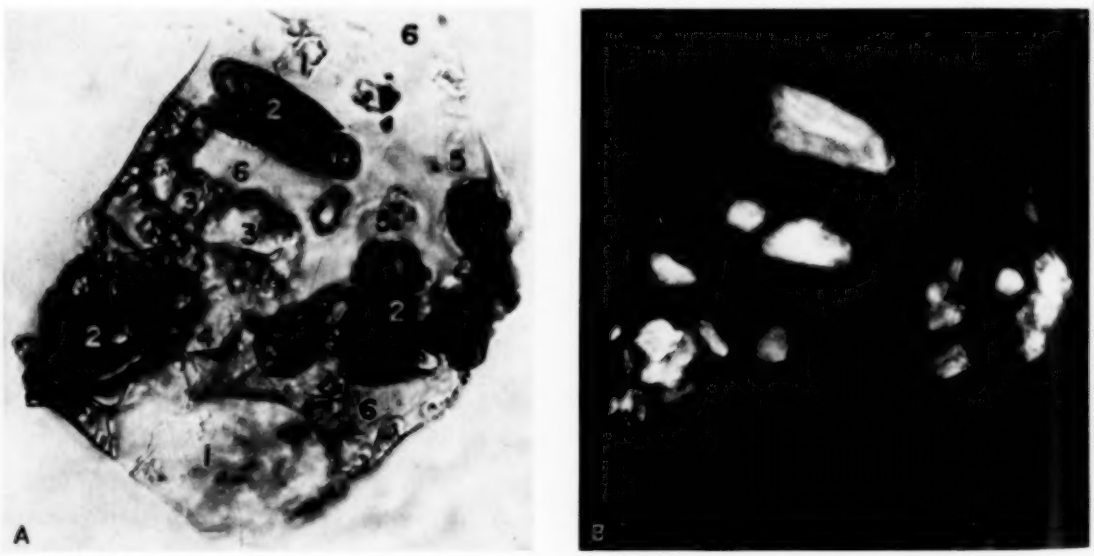

FIGURE 4. *(A) Invariant poin composition quenched from 1,310° C showing crystals of* C_3A *(1),* F *ss (2),* C_2S *(3),* NC_8A *(4), and* C_3S *(5) embedded in a glassy matrix (6), total magnification 470 diameters. (B) Same field under crossed nicols. 470 diameters.*

center of the field as clear crystals showing white to yellow birefringence. Phase 4 consists of small, transparent, flat grains of NC_8A_3 having a comparatively lower degree of birefringence. A possible phase 5, interpreted as C_2S, occurs in very small grains having low birefringence (gray). Because of the similarity in optical properties of this phase and small particles of NC_8A_3, identification was difficult. Phase 6, the glassy matrix, is light tan in color (probably caused by the presence of iron) with a refractive index higher than that of the mounting medium.

Although color plays an important part in differentiating the above phases, other optical properties were also used for actual identification. It was not feasible to reproduce these micrographs in color. Also, in the relatively large specimen that was required for viewing the five crystalline phases it was difficult to focus all phases simultaneously.

From this and similar observations it appears that the invariant point for NC_8A_3, C_3A, F_{88}, C_2S, C_2S, and liquid is about 1,310° C and is near the composition point represented by 13N10. The oxide composition of this point is about 1.0 percent-Na_2O, 48.0 percent-CaO, 31.0-percent Al_2O_3, 13.5 percent-Fe_2O_3, and 6.5-percent SiO_2. Five-component mixes in this quinary system approximating the composition of portland-cement clinker will crystallize completely at about 1,310° C upon slow cooling.

VI. Discussion

In this investigation it was noted that additions of Na_2O considerably lowered the temperature of appearance of first liquid. Certain low-melting mixes, for example, 10N26F5, table 4, showed some liquid formation when heated as low as 1,290° C. Hansen [12] in studying a high-lime, low-alumina mix having the composition 2.2 Na_2O, 65.7 CaO, 6.4 Al_2O_3, 3.2 Fe_2O_3, 22.5 percent SiO_2 found that the first indications of melting occurred at 1,315°. Much higher temperatures are required for complete melting. In the present investigation, however, the invariant composition melts completely at about 1,310°.

The effect of MgO on the quinary invariant points is important to the chemistry of cement, as this component is present in the commercial product. Magnesia, together with the five components considered in this study, represents about 99 percent of the constitution of clinker. Since there has been no evidence of new phases formed when MgO is present [11], it is probable that only a lowering of the melting temperature results. Swayze [2] found that about 5 percent of MgO could be dissolved in the liquids studied in the system CaO-C_5A_3-C_2F-C_2S as a result of which the temperatures at invariant points were lowered by about 35 deg. It may be permissible on the same basis to predict that MgO may lower the quinary invariant temperature from 1,310°, found in this investigation, to about 1,275°. Hansen [12] found that melting started at about this temperature (1,280°) when a mixture of these six components was burned.

The results also indicate that a closer computation of the actual percentage of liquid formed may be made when mixes containing Na_2O are burned. Thus, instead of adding the percentage of Na_2O present to the calculated percentage of liquid as has been suggested [13], one must also consider the effect of formation of NC_8A_3 on the relative proportions of CaO and Al_2O_3.

The observations made in this study have established the stable existence of the soda compound NC_8A_3 in the presence of the principal components of portland cement clinker.

Under certain conditions Na_2O may react with other components, producing new phases. The data also indicate that a closer approximation of the glass composition in rapidly cooled clinker can be made.

The data obtained for the quinary system represent equilibrium conditions, whereas in the commercial clinkering operation this is not the case and must be considered when applying these data. Application is further limited, since the effects of the small amounts of minor constituents such as Mn_2O_3, TiO_2, Li_2O, and others on the phase-equilibrium relations of the system are not known. More information on the quinary system itself will be necessary in order that wider application to the problems of cement manufacture may be made.

VII. References

[1] F. M. Lea and T. W. Parker, Phil. Trans. Royal Soc. [A], **234,** No. 731, 1 (1934).

[2] M. A. Swayze, Am. J. Sci. **244,** 1; 65 (1946).

[3] K. T. Greene and R. H. Bogue, J. Research NBS **36,** 187 (1946) RP1699; PCAF Paper 47.

[4] W. R. Eubank and R. H. Bogue, J. Research NBS **40,** 225 (1948) RP1867; PCAF Paper 50.

[5] R. H. Bogue, The chemistry of portland cement (Reinhold Pub. Co., New York, N. Y., 1947).

[6] K. T. Greene and W. R. Morgan, J. Am. Ceram. Soc. **24,** 111 (1941).

[7] W. R. Eubank, Precision thermostat for high temperatures (publication pending).

[8] L. A. Dahl, Parametric equations in the treatment of multi-component systems, J. Phys. Colloid Chem. (publication pending).

[9] L. A. Dahl, J. Phys. Colloid Chem. **52,** 698 (1948); PCAF Paper 51.

[10] L. A. Dahl, J. Chem. Education **26,** 411 (1949); PCAF Paper 52.

[11] H. F. McMurdie and H. Insley, J. Research NBS **16,** 467 (1936) RP884.

[12] W. C. Hansen, B. S. J. Research **2,** 55 (1930) RP39; PCAF Paper 22.

[13] F. M. Lea and T. W. Parker, Build. Res. Tech. Paper No. 16 (1935).

WASHINGTON, November 8, 1948.

U. S. Department of Commerce
National Bureau of Standards

Research Paper RP2070
Volume 44, February 1950

Part of the Journal of Research of the National Bureau of Standards

The Field Generated by an Arbitrary Current Distribution Within a Waveguide

By J. J. Freeman

Formulas are derived for the electromagnetic field generated by an arbitrary current distribution within waveguides of rectangular, circular, and coaxial cross sections. These formulas are obtained by generalizing analogous formulas obtained in a previous paper [2] for cavities of the same cross section. As a check on the formulas, it is shown that the field from an axially directed dipole within a circular guide reduces to the free space value as the radius increases indefinitely.

I. Introduction

In pursuing certain investigations, it was found necessary to derive explicit expressions for the electromagnetic field generated by an arbitrary current distribution within a waveguide. Since the corresponding problem for a cylindrical cavity had already been worked out in a previous paper (see footnote 2), henceforth designated as Paper I, the results of Paper I were generalized to apply to a waveguide of corresponding cross section by the simple expedient of allowing the length of the cavity to become infinitely large. Although the same formulas may be obtained more directly by a different method,[3] the present paper derives these formulas using the above mentioned limiting process since: (a) no explicit general solution of the problem has yet been published; (b) although the expedient of first using a finite cavity for various computations involving electromagnetic fields, and then allowing the dimensions of the cavity to become infinitely large has been widely employed, the validity of the limiting process is not entirely obvious, and the following derivation throws light on this process.

To avoid repetition it will be assumed that Paper I is available to the reader, and the results contained therein will be utilized without further comment. MKS units are employed. Although it was assumed in Paper I that the medium within the cavity was lossless, and that the wave number, $k=\omega\sqrt{\mu\epsilon}$, was real, the results are still valid for complex values of k. Accordingly, in the following, we assume that the medium has conductivity σ, so that

$$k^2=\omega^2\mu\epsilon+j\mu\omega\sigma.$$

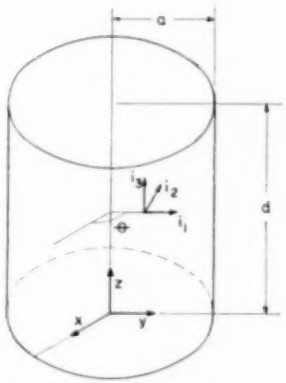

FIGURE 1. *Cylindrical cavity.*

II. The Circular Cylindrical Waveguide

Consider a cylindrical cavity, of length d (fig. 1) containing current of volume density $\boldsymbol{J}(\boldsymbol{r}')$, where $\boldsymbol{r}'$ designates the position vector of $\boldsymbol{J}$, and

[1] This paper is a revision of Report CRPL-9-3, issued under the same title (Feb. 28, 1947).
[2] J. J. Freeman, Theory and design of a cavity attenuator, J. Research NBS 40, 235 (1948) RP1868.
[3] J. J. Freeman, The noise spectrum of a diode with a retarding field, J. Research NBS 42, 75 (1949) RP1953 (see appendix I).

867020—50——6

where the time variation, $e^{j\omega t}$ is omitted. In eq 15 and 21, Paper I, it was shown that

$$\boldsymbol{E}_{TE}=j\omega\mu\sum_{n=0}^{\infty}\sum_{m=1}^{\infty}A_{nm}^{2}\int\boldsymbol{J}(\boldsymbol{r}')\cdot\boldsymbol{m}(\boldsymbol{r}')\sum_{l=1}^{\infty}\frac{\sin\frac{l\pi z'}{d}\sin\frac{l\pi z}{d}}{\delta^{2}-k^{2}+\frac{l^{2}\pi^{2}}{d^{2}}}\,d\tau', \quad (1)$$

where l, m, n, $=0, 1, 2, \ldots$ and,

$$\boldsymbol{E}_{TM}=\frac{j}{\omega\epsilon}\int\boldsymbol{J}(\boldsymbol{r}')\cdot\sum_{n=0}^{\infty}\sum_{m=1}^{\infty}F_{nm}^{2}\left\{\boldsymbol{n}(\boldsymbol{r}')\boldsymbol{n}(\boldsymbol{r})\frac{k^{2}-\lambda^{2}}{\lambda^{2}}\sum_{l=1}^{\infty}\frac{\sin\frac{l\pi z'}{d}\sin\frac{l\pi z}{d}}{\lambda^{2}-k^{2}+\frac{l^{2}\pi^{2}}{d^{2}}}+\boldsymbol{n}(\boldsymbol{r}')\boldsymbol{p}(\boldsymbol{r})\sum_{l=1}^{\infty}\frac{\frac{l\pi}{d}\sin\frac{l\pi z'}{d}\cos\frac{l\pi z}{d}}{\lambda^{2}-k^{2}+\frac{l^{2}\pi^{2}}{d^{2}}}+\boldsymbol{p}(\boldsymbol{r}')\boldsymbol{n}(\boldsymbol{r})\sum_{l=1}^{\infty}\frac{\frac{l\pi}{d}\cos\frac{l\pi z'}{d}\sin\frac{l\pi z}{d}}{\lambda^{2}-k^{2}+\frac{l^{2}\pi^{2}}{d^{2}}}+\boldsymbol{p}(\boldsymbol{r}')\boldsymbol{p}(\boldsymbol{r})\sum_{l=0}^{\infty}\frac{\left(k^{2}-\frac{l^{2}\pi^{2}}{d^{2}}\right)\cos\frac{l\pi z'}{d}\cos\frac{l\pi z}{d}}{\left(\lambda^{2}-k^{2}+\frac{l^{2}\pi^{2}}{d^{2}}\right)(1+\delta_{0}^{l})}\right\}d\tau' \quad (2)$$

$$\delta_{0}^{l}=\begin{cases}0, \text{ for } l\neq 0\\ 1, \text{ for } l=1\end{cases}$$

In the above, $d\tau'$ represents an element of volume containing $\boldsymbol{J}$, and $\boldsymbol{r}$ is the position vector of the point of observation. The $\boldsymbol{m}$, $\boldsymbol{n}$, $\boldsymbol{p}$, δ, and λ in eq 1 and 2 have the identifying subscripts mn implied but omitted. Also, the even, odd designations $\binom{e}{o}$ are omitted for convenience, but are implied. For the case of a cavity of circular cross-section, of radius a, (fig. 1),

$$\boldsymbol{m}_{nm}^{\binom{e}{o}}=\frac{n}{r}\begin{pmatrix}-\sin n\theta\\ \cos n\theta\end{pmatrix}J_{n}(\delta r)\boldsymbol{i}_{1}-\begin{pmatrix}\cos n\theta\\ \sin n\theta\end{pmatrix}\delta J_{n}'(\delta r)\boldsymbol{i}_{2}, \quad (3)$$

where $\boldsymbol{i}_1$,$\boldsymbol{i}_2$, and $\boldsymbol{i}_3$ are unit vectors in the directions of increasing r,θ, and z, and

$$A_{nm}^{\binom{e}{o}}=\frac{\sqrt{2\beta_{n}}}{\sqrt{\pi d}\sqrt{v_{nm}^{2}-n^{2}}J_{n}(v_{nm})}\qquad \begin{matrix}\beta_{n}=1 \text{ for } n=0\\ \beta_{n}=2 \text{ for } n\neq 0.\end{matrix} \quad (4)$$

$$\delta=\delta_{nm}=\frac{v_{nm}}{a}, \text{ where } J_{n}'(v_{nm})=0. \quad (5)$$

Also,

$$\boldsymbol{n}_{nm}^{\binom{e}{o}}=-\lambda J_{n}'(\lambda r)\begin{pmatrix}\cos n\theta\\ \sin n\theta\end{pmatrix}\boldsymbol{i}_{1}+\begin{pmatrix}\sin n\theta\\ -\cos n\theta\end{pmatrix}\frac{n}{r}J_{n}(\delta r)\boldsymbol{i}_{2} \quad (6)$$

$$\boldsymbol{p}_{nm}^{\binom{e}{o}}=\begin{pmatrix}\cos n\theta\\ \sin n\theta\end{pmatrix}J_{n}(\lambda r)\boldsymbol{i}_{3}, \quad (7)$$

$$F_{nm}=\frac{\sqrt{2\beta_{n}}}{a\sqrt{\pi d}J_{n-1}(\lambda a)}, \quad (8)$$

$$\lambda=\lambda_{nm}=\frac{u_{nm}}{a}, \text{ where } J_{n}(u_{nm})=0. \quad (9)$$

To generalize eq 1 and 2 to the case of an infinite waveguide, with a conducting plug at $z=0$, we let $d\to\infty$, and evaluate the limit of the infinite summation over the index l as $d\to\infty$.

Consider the sum over l in eq 1, multiplied by the factor $1/d$.

$$S_{1}=\frac{1}{d}\sum_{l=1}^{\infty}\frac{\sin\frac{l\pi z'}{d}\sin\frac{l\pi z}{d}}{\frac{l^{2}\pi^{2}}{d^{2}}-g^{2}}=1/2d\sum_{l=-\infty}^{\infty}\frac{\sin\frac{l\pi z'}{d}\sin\frac{l\pi z}{d}}{\frac{l^{2}\pi^{2}}{d^{2}}-g^{2}} \quad (10)$$

where

$$g^{2}=k^{2}-\delta^{2}.$$

The factor $1/d$ enters because it is contained in the normalizing factor A_{nm}^{2}, (eq 4). Let $\xi=l\pi/d$. Then

$$S_{1}=1/2d\sum_{l=-\infty}^{\infty}\frac{\sin\xi z'\sin\xi z}{\xi^{2}-g^{2}}\,\Delta l=\frac{1}{2\pi}\sum_{\xi}\frac{\sin\xi z'\sin\xi z}{\xi^{2}-g^{2}}\,\Delta\xi$$

since $\Delta l=1$. As $d\to\infty$, $\Delta\xi\to 0$, and the sum becomes in the limit the integral,

$$S_{1}=\frac{1}{2\pi}\int_{-\infty}^{\infty}\frac{\sin\xi z'\sin\xi z\,d\xi}{\xi^{2}-g^{2}}=\frac{1}{4\pi}\int_{-\infty}^{\infty}\frac{\cos\xi(z-z')-\cos\xi(z+z')}{\xi^{2}-g^{2}}\,d\xi.$$

Since $\int_{-\infty}^{\infty}\frac{\sin\xi(z-z')d\xi}{\xi^{2}-g^{2}}=0$, because the sin is an odd function,

$$S_{1}=\frac{1}{4\pi}\int_{-\infty}^{\infty}\frac{e^{j\xi(z-z')}-e^{j\xi(z+z')}}{\xi^{2}-g^{2}}\,d\xi. \quad (11)$$

Let g_1 and g_2 be the two square roots of $g^2=k^2-\delta^2$.

which lie in the positive- and negative-imaginary parts of the complex plane, respectively. Then

$$g_2 = -g_1. \tag{12}$$

For frequencies above cut-off, when $\omega^2\mu\epsilon > \delta^2$,

$$g_1 = |g| e^{\frac{j\psi}{2}} \tag{13}$$

where

$$|g| = [(\omega^2\mu\epsilon - \delta^2)^2 + \omega^2\mu^2\sigma^2]^{\frac{1}{2}} \tag{14}$$

and

$$\tan \psi = \frac{\omega\mu\sigma}{|\omega^2\mu\epsilon - \delta^2|}. \tag{15}$$

For frequencies below cut-off, when $\omega^2\mu\epsilon < \delta^2$,

$$g_1 = j|g| e^{\frac{-j\psi}{2}}. \tag{16}$$

Consider

$$\int_{-\infty}^{\infty} \frac{e^{j\xi(z-z')} d\xi}{\xi^2 - g^2}.$$

Since, for $z > z'$, $\frac{e^{j\xi(z-z')}}{\xi^2 - g^2}$ vanishes over the positive-imaginary part of the plane, as $|\xi| \to \infty$, the integral can be evaluated by taking the residue around the pole g_1 (fig. 2). Thus,

$$\int_{-\infty}^{\infty} \frac{e^{j\xi(z-z')}}{(\xi+g)(\xi-g)} d\xi = \frac{2\pi j e^{jg_1(z-z')}}{2g_1}.$$

For $z < z'$, $\frac{e^{j\xi(z-z')}}{\xi^2 - g^2}$ vanishes over the negative-imaginary half-plane, as $|\xi| \to \infty$, and the integral can be evaluated by taking the residue around the pole (fig. 2) g_2. Thus, for $z < z'$,

$$\int_{-\infty}^{\infty} \frac{e^{j\xi(z-z')}}{\xi^2 - g^2} d\xi = -2\pi j \frac{e^{jg_2(z-z')}}{2g_2} = \frac{2\pi j e^{-jg_1(z-z')}}{2g_1},$$

or

$$\int_{-\infty}^{\infty} \frac{e^{j\xi(z-z')}}{\xi^2 - g^2} d\xi = \frac{\pi j}{g_1} e^{jg_1|z-z'|} \text{ for } z \gtrless z'. \tag{17}$$

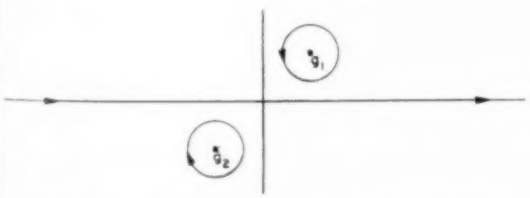

FIGURE 2. *Contour of integration path in complex plane.*

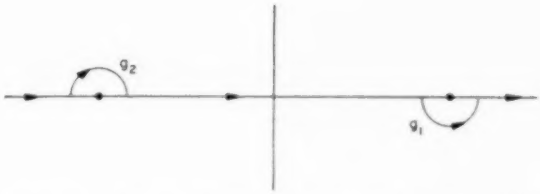

FIGURE 3. *Contour of integration path used by Sommerfeld.*

If $\sigma = 0$, instead of integrating along the real axis of the s-plane it becomes necessary to indent the path at g_1 and g_2 as shown in figure 3, obtaining the contour that Sommerfeld [4] used in the complex integral representation of the Green's function for the one-dimensional wave equation.

From eq 11, one recognizes that S_1 represents two plane waves traveling in the $+z$-direction (for $z > z'$), one having its source at $z = z'$, and the other at $z = -z'$. Also, since $\boldsymbol{m}$ is a vector lying in the plane perpendicular to the z-direction and since only transverse elements of current make a contribution to the field in eq 1, the first integral in eq 11 represents the contribution due to a current element at $z = z'$, and the second integral represents the contribution of its electrical image, situated at $z = -z'$. Both element and image are necessary to insure the vanishing of the tangential component of $\boldsymbol{E}$ at $z = 0$, which corresponds to the case of a conducting plug at $z = 0$. On the other hand, if the guide is infinitely long in the negative z-direction, then the contribution of the image at $z = -z'$ must be omitted, and the second integral in eq 11 must be neglected.

Since the case of a perfectly conducting plug at $z = 0$ may be easily derived from the case of an infinite guide by superposing the electrical image with respect to the plane $z = 0$, the following is restricted to the case of a guide extending to infinity in both directions.

Accordingly, from eq 11 and 17, neglecting the contribution from the image,

$$S_1 = \frac{j}{4g_1} e^{jg_1|z-z'|} \quad (z \gtrless z'). \tag{18}$$

Substituting eq 18 in eq 1,

$$E_{TE} = \frac{-\omega\mu}{2\pi} \sum_{n=0}^{\infty} \sum_{m=1}^{\infty} \frac{\beta_n \int \boldsymbol{J} \cdot \boldsymbol{m}(\mathbf{r}') e^{jg_1|z-z'|} \boldsymbol{m}(\mathbf{r})}{g_1(\ell_{nm}^2 - n^2) J_n^2(r_{nm})} d\tau'$$
$$(z \gtrless z'). \tag{19}$$

[4] A. Sommerfeld, Deutsche Mathematiker—Vereinigung Jahresbericht, **21**, 309 (1912).

The various summations over the index l in eq 2 may likewise be extended to the case of a guide extending to infinity in the positive z-direction, with a conducting plug at $z=0$. By omitting contributions to the field arising from the electrical image with respect to the perfectly conducting plane at $z=0$ of current elements within the guide, the boundary conditions are changed from the case of a perfectly conducting plug to the case of a guide infinite in both directions. Then, if one computes the limiting values of the summations by the method of residues and omits the contribution from the image one obtains:

$$\frac{1}{d}\sum_{l=0}^{\infty}\frac{\cos\frac{l\pi z'}{d}\cos\frac{l\pi z}{d}}{\left(1+\delta_0^l\right)\left(\frac{l^2\pi^2}{d^2}-h^2\right)}=\frac{j}{4h_1}e^{jh_1|z-z'|}\left(z\gtrless z'\right) \tag{20}$$

$$\frac{1}{d}\sum_{l=0}^{\infty}\frac{\frac{l^2\pi^2}{d^2}\cos\frac{l\pi z'}{d}\cos\frac{l\pi z}{d}}{\frac{l^2\pi^2}{d^2}-h^2}=\frac{jh_1}{4}e^{+jh_1|z-z'|}\left(z\gtrless z'\right) \tag{21}$$

$$\frac{1}{d}\sum_{l=0}^{\infty}\frac{\frac{l\pi}{d}\sin\frac{l\pi z'}{d}\cos\frac{l\pi z}{d}}{\frac{l^2\pi^2}{d^2}-h^2}=\pm\frac{1}{4}e^{+jh|z-z'|}\left(z\gtrless z'\right) \tag{22}$$

$$\frac{1}{d}\sum_{l=0}^{\infty}\frac{\frac{l\pi}{d}\cos\frac{l\pi z'}{d}\sin\frac{l\pi z}{d}}{\frac{l^2\pi^2}{d^2}-h^2}=\pm\frac{1}{4}e^{+jh_1|z-z'|}\left(z\gtrless z'\right), \tag{23}$$

where, for brevity,

$$h^2=k^2-\lambda^2. \tag{23a}$$

If eq 8, 18, 20, 21, 22, and 23, are substituted in eq 2, one finally obtains

$$E_{TM}=-\frac{\int\boldsymbol{J}(\boldsymbol{r}')}{2\pi\omega\epsilon a^2}\cdot\left\{\sum_{n=0}^{\infty}\sum_{m=1}^{\infty}\frac{\beta_n}{J_{n-1}^2(u_{nm})}\right.$$
$$\left[\frac{h_1a^2}{u_{nm}^2}\boldsymbol{n}(\boldsymbol{r}')\boldsymbol{n}(\boldsymbol{r})\pm j\boldsymbol{n}(\boldsymbol{r}')\boldsymbol{p}(\boldsymbol{r})\mp j\boldsymbol{p}(\boldsymbol{r}')\boldsymbol{n}(\boldsymbol{r})+\right.$$
$$\left.\left.\frac{u_{nm}^2}{h_1a^2}\boldsymbol{p}(\boldsymbol{r}')\boldsymbol{p}(\boldsymbol{r})\right]e^{+jh_1|z-z'|}\right\}d\tau' \text{ for } z\gtrless z'. \tag{24}$$

Here h_1 is that square root of $k^2-\lambda^2$ that lies in the positive-imaginary half-plane.

As a check on the derivation, it will be shown that waveguide eq 19 and 24 reduce to the correct value for the free space field, as the boundaries recede indefinitely.

Consider a current filament of length dl, carrying current I parallel to the axis of the guide and situated at the origin of coordinates. Then $E_{TE}=0$, and eq 24 becomes,

$$E_{TM}=\frac{-1}{2\pi\omega\epsilon a^2}\sum_{m=1}^{\infty}\frac{\int\boldsymbol{J}\cdot\boldsymbol{p}d\tau'}{J_1^2(u_{om})}\left[-j\boldsymbol{n}+\frac{u_{om}^2\boldsymbol{p}}{h_1a^2}\right]e^{jh_1z}, \tag{25}$$

since only the symmetric modes for which $n=0$ are excited, and $\boldsymbol{J}$ is normal to $\boldsymbol{n}$.

$$\int\boldsymbol{J}\cdot\boldsymbol{p}d\tau'=\int\boldsymbol{J}\cdot\boldsymbol{i}_3J_o(\lambda r')\,d\tau'=I\,dl.$$

Since $\boldsymbol{n}_{om}=-\lambda J_o'(\lambda r)\boldsymbol{i}_1=-\frac{d}{dr}J_o(\lambda r)\boldsymbol{i}_1$, from eq 6, and $\boldsymbol{p}_{om}=J_o(\lambda r)\boldsymbol{i}_3$, from eq 7, eq 25 becomes

$$E_{TM}=\frac{-Idl}{2\pi\omega\epsilon a^2}\sum_{m=1}^{\infty}$$
$$\left[j\frac{d}{dr}\left(J_o(\lambda r)\right)\boldsymbol{i}_1+\frac{u_{om}^2}{h_1a^2}\frac{J_o(\lambda r)\boldsymbol{i}_3}{J_1^2(u_{om})}\right]e^{jh_1z}. \tag{26}$$

Equation 26 may be rearranged into the following more convenient form:

$$E_{TM}=\frac{-Idl}{2\pi\epsilon\omega}\left(\text{grad div}+k^2\right)\sum_{m=1}^{\infty}\frac{J_o(\lambda r)e^{jh_1z}}{h_1a^2J_1^2(u_{om})}\boldsymbol{i}_3. \tag{27}$$

Consider the sum

$$S=\sum_{m=1}^{\infty}\frac{J_o(\lambda r)e^{jh_1z}}{h_1a^2J_1^2(u_{om})}. \tag{28}$$

There exists an integer M such that for $m>M$, u_{om} will be large enough so that $J_o(u_{om})$ may be replaced by its asymptotic value[5],

$$J_0(u_{om})\simeq\sqrt{\frac{2}{\pi u_{om}}}\cos\left(u_{om}-\frac{2n+1}{4}\pi\right). \tag{29}$$

Since u_{om} is the m^{th} root of $J_o(u_{om})=0$, eq 29 yields, for $m>M$,

$$u_{om}=\pi(m+3/4). \tag{30}$$

Accordingly,

$$J_1^2(u_{om})=2/\pi\,u_{om},\ m>M. \tag{31}$$

Equation 28 may then be separated into two sums.

[5] J. A. Stratton, Electromagnetic theory, p. 359, eq 18 (McGraw-Hill Book Co., Inc., New York, N. Y., 1941).

$$S=\sum_{m=1}^{M}\frac{J_o(\lambda r)e^{jh_1z}}{h_1a^2J_1^2(u_{om})}+\frac{1}{2}\sum_{m=M}^{\infty}\frac{\pi u_{om}J_o(\lambda r)e^{jh_1z}}{a^2h_1}\Delta m. \quad (32)$$

From eq 30, $\Delta m=\frac{\Delta u_{om}}{\pi}$, and since $\lambda=\frac{u_{om}}{a}$,

$$\Delta m=\frac{a}{\pi}\Delta\lambda. \quad (33)$$

Accordingly, eq 32 may be rewritten as follows:

$$S=\sum_{m=1}^{M}\frac{J_o(\lambda r)e^{jh_1z}}{h_1a^2J_1^2(u_{om})}+\frac{1}{2}\sum_{\lambda=\frac{\pi}{a}\ (M+3/4)}^{\infty}\frac{J_o(\lambda r)\lambda e^{jh_1z}}{h_1}\Delta\lambda. \quad (34)$$

Now let $a\to\infty$. As a increases without limit the first sum in eq 34 approaches zero, $\Delta\lambda\to 0$; the second summation becomes, by definition, an integral; and the lower limit of integration becomes zero.

Thus, as $a\to\infty$,

$$S=\frac{1}{2}\int_0^\infty\frac{J_o(\lambda r)e^{jh_1z}\lambda}{h_1}d\lambda. \quad (35)$$

Substituting from (eq 23a),

$$jh_1=-\sqrt{\lambda^2-k^2}$$

into eq 35, one obtains

$$S=\frac{1}{2j}\int_0^\infty\frac{J_o(\lambda r)e^{-\sqrt{\lambda^2-k^2}z}\lambda}{(\lambda^2-k^2)^{1/2}}d\lambda, \quad (36)$$

where that square root is to be taken whose real part is positive.

But

$$\int_0^\infty\frac{J_o(\lambda r)e^{-\sqrt{\lambda^2-k^2}z}}{(\lambda^2-k^2)^{1/2}}\lambda d\lambda$$

is the well-known[6] expansion for $\frac{e^{jkR}}{R}$ where $R=\sqrt{r^2+z^2}$. Accordingly, eq 27 becomes

$$E_{TM}=(\text{grad div}+k^2)\left(\frac{jIdl}{4\pi\omega\epsilon}\frac{e^{jkR}}{R}\boldsymbol{i}_3\right). \quad (37)$$

which is the field due to a current element $Idl\ \boldsymbol{i}_3$ in free space.[7]

[6] J. A. Stratton, Electromagnetic theory, p. 576, eq 17 (McGraw-Hill Book Co., Inc., New York, N. Y., 1941).

[7] J. A. Stratton, Electromagnetic theory, p. 431, eq 44 (McGraw-Hill Book Co., Inc., New York, N. Y., 1941).

III. Rectangular Cross Section

The same general formulas (eq 1 and 2), hold in the case of a cavity of length c, and of rectangular cross section, whose x and y dimensions are a and b, respectively, with the origin at one corner (fig. 4). Here, however, the normalizing factors and vector functions corresponding to the rectangular cross section are as follows:

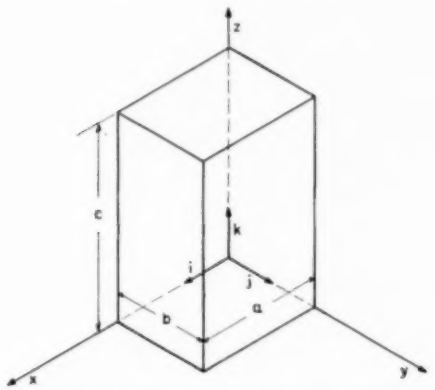

FIGURE 4. *Cavity of rectangular cross section.*

$$\boldsymbol{m}_{nm}=\left[-\frac{m\pi}{b}\sin\frac{m\pi y}{b}\cos\frac{n\pi x}{a}\boldsymbol{i}+\frac{n\pi}{a}\sin\frac{n\pi x}{a}\cos\frac{m\pi y}{b}\boldsymbol{j}\right] \quad (38)$$

$$\boldsymbol{n}_{nm}=-\left[\frac{n\pi}{a}\cos\frac{n\pi x}{a}\sin\frac{m\pi y}{b}\boldsymbol{i}+\frac{m\pi}{b}\cos\frac{m\pi y}{b}\sin\frac{n\pi x}{a}\boldsymbol{j}\right] \quad (39)$$

$$\boldsymbol{p}_{nm}=\sin\frac{n\pi x}{a}\sin\frac{m\pi y}{b}\boldsymbol{k} \quad (40)$$

$$A_{nm}=\frac{1}{\lambda_{nm}}\left(\frac{\beta_{nm}}{abc}\right)^{1/2} \quad (41)$$

where

$$\beta_{nm}=\begin{matrix}1 \text{ for } n \text{ or } m=0\\ 2 \text{ for } n \text{ and } m\neq 0\end{matrix} \quad (42)$$

$$\lambda_{nm}=\left[\frac{n^2}{a^2}+\frac{m^2}{b^2}\right]^{1/2} \quad (43)$$

$$F=\left(\frac{8}{abc}\right)^{1/2}. \quad (44)$$

Accordingly, when eq 38 through eq 44 are substituted in eq 1 and 2, and eq 18, 20 to 23 are

substituted for the infinite summations over the index l, one gets for the case of a guide infinite in both directions,

$$E_{TE}=\frac{-\omega\beta}{ab}\sum_{n=0}^{\infty}\sum_{m=0}^{\infty}\frac{\beta_{nm}}{\lambda_{nm}^2 g}\int \boldsymbol{J}(\boldsymbol{r}')\cdot\boldsymbol{m}(\boldsymbol{r}')\, e^{\mp j g(z-z')}d\tau'\,\boldsymbol{m}(\boldsymbol{r}),\ z\gtrless z' \quad (45)$$

$$E_{TM}=\frac{-1}{\omega\epsilon ab}\int \boldsymbol{J}(\boldsymbol{r}')\sum_{n=0}^{\infty}\sum_{m=0}^{\infty}\beta_{nm}\left\{\boldsymbol{n}(\boldsymbol{r}')\boldsymbol{n}(\boldsymbol{r})\frac{g}{\lambda_{nm}^2}\pm j\boldsymbol{n}(\boldsymbol{r}')\boldsymbol{p}(\boldsymbol{r})\mp j\boldsymbol{p}(\boldsymbol{r}')\boldsymbol{n}(\boldsymbol{r})+\frac{\lambda_{nm}^2}{g}\boldsymbol{p}(\boldsymbol{r}')\boldsymbol{p}(\boldsymbol{r})\right\} e^{\mp j g(z-z')}d\tau' \text{ for } z\gtrless z'.$$

Here, g is that square root of

$$g^2=k^2-\frac{n^2}{a^2}-\frac{m^2}{b^2}, \quad (46)$$

that lies in the positive-imaginary part of the complex plane.

IV. Coaxial Cross Section

Similar computations for the case of a coaxial cross-section guide of inner radius a and outer radius b yield the following formulas:

$$E_{TE}=\frac{-\omega\mu\pi}{8}\sum_{n=0}^{\infty}\sum_{m=1}^{\infty}\frac{\beta_n J_n'^2(\eta b)\int \boldsymbol{J}(\boldsymbol{r}')\cdot\boldsymbol{m}(\boldsymbol{r}')e^{\mp j g(z-z')}d\tau'\,\boldsymbol{m}(\boldsymbol{r})}{\left\{J_n'^2(\eta a)\left(1-\frac{n^2}{\eta^2 b^2}\right)-J_n'^2(\eta b)\left(1-\frac{n^2}{\eta^2 a^2}\right)\right\} g}\quad z\gtrless z' \quad (47)$$

where

$$\underset{o}{\boldsymbol{m}}_{nm}=\frac{n}{r}\begin{pmatrix}-\sin n\theta\\ \cos n\theta\end{pmatrix}\dot{Z}_n(\eta r)\boldsymbol{i}_1-\begin{pmatrix}\cos n\theta\\ \sin n\theta\end{pmatrix}\dot{Z}_n'(\eta r)\boldsymbol{i}_2, \quad (48)$$

$$\dot{Z}_n(\eta r)=J_n(\eta r)N_n'(\eta a)-N_n(\eta r)J_n'(\eta a), \quad (49)$$

and

η_{nm} is a root of $\begin{vmatrix}J_n'(\eta a) & N_n'(\eta a)\\ J_n'(\eta b) & N_n'(\eta b)\end{vmatrix}=0$, (50)

Here, g is that root of

$$g^2=k^2-\eta^2 \quad (51)$$

that lies in the positive-imaginary part of the plane.

$$E_{TM}=-\frac{\pi}{8\omega\epsilon}\sum_{n=0}^{\infty}\sum_{m=1}^{\infty}\frac{\beta_n\lambda_{nm}^2 J_n^2(\lambda b)}{J_n^2(\lambda a)-J_n^2(\lambda b)}\int \boldsymbol{J}(\boldsymbol{r}')\cdot\left\{\frac{h}{\lambda^2}nn\pm jnp\mp jpn+\frac{\lambda^2}{g}pp\right\}e^{\mp jh(z-z')}d\tau'+\frac{\sqrt{\frac{\mu}{\epsilon}}}{4\pi ln\frac{b}{a}}\int \boldsymbol{J}\cdot\frac{\boldsymbol{i}_1}{r'}\frac{\boldsymbol{i}_1}{r}e^{\mp jk(z-z')}d\tau' z\gtrless z'.$$

The unit vectors i_1, i_2, i_3 are defined in figure 1. Here

$$\underset{o}{\boldsymbol{n}}_{nm}=\left[-\alpha Z_n'(\alpha r)\begin{pmatrix}\cos n\theta\\ \sin n\theta\end{pmatrix}\boldsymbol{i}_1+\begin{pmatrix}\sin n\theta\\ -\cos n\theta\end{pmatrix}\frac{n}{r}Z_n\boldsymbol{i}_2\right] \quad (52)$$

$$\underset{o}{\boldsymbol{p}}_{nm}=\begin{pmatrix}\cos n\theta\\ \sin n\theta\end{pmatrix}Z_n(\alpha r)\boldsymbol{i}_3, \quad (53)$$

$$Z_n(\alpha r)=J_n(\alpha r)N_n(\alpha a)-N_n(\alpha r)J_n(\alpha a), \quad (54)$$

where α_{nm} is a solution of $\begin{vmatrix}J_n(\alpha a) & N_n(\alpha a)\\ J_n(\alpha b) & N_n(\alpha b)\end{vmatrix}=0$ (55)

and h is that square root of

$$h^2=k^2-\alpha^2, \quad (56)$$

which lies in the positive-imaginary part of the plane.

V. Conclusion

The fields within a waveguide excited by an arbitrary current distribution have been calculated for the cases of circular, rectangular, and coaxial cross section by taking the limit of the corresponding expressions for cylindrical cavities of corresponding cross section as the length of the cavities becomes infinitely great.

Washington, April 20, 1949.

U. S. Department of Commerce
National Bureau of Standards

Research Paper RP2071
Volume 44, February 1950

Part of the Journal of Research of the National Bureau of Standards

Back-Scatter Observations by the Central Radio Propagation Laboratory—August 1947 to March 1948

By W. L. Hartsfield, S. M. Ostrow, and R. Silberstein

A high-power pulsing transmitter and a westwardly beamed antenna system were constructed, and emissions were made from Sterling, Virginia, on 13,660 kilocycles, for reception by USNEL and USAF cooperating groups. CRPL efforts were concentrated on the study of "back scatter" received near the transmitter.

In the controversial issue as to whether back scatter comes from the ground or the E region, it was believed that both types were identified, with ground scatter usually predominating, except in the case of long skip.

Aids to data interpretation were transponder echoes, reception logs and skip distance maps drawn from concurrent ionospheric data.

I. Introduction

1. Historical Background

It has been known for many years [1, 3, 6, 9] [1] that low-quality radio signals may be received when the receiving station is within the skip zone of the transmitting station. This phenomenon has been given the name "scatter".

When electromagnetic waves impinge upon clouds of ions, energy is scattered in all directions from the clouds. The intensity of the scattered energy is strongest in the original direction of propagation (forward scatter) and weakest in the opposite direction (back scatter). If the ionic clouds are randomly distributed, and of various densities, the scattered energy is quite weak, and the scattered signals fluctuate rapidly in phase and intensity. Scatter may also occur when the radio waves strike a rough surface, such as the ground or the sea.

Signals scattered back toward the transmitter are of low and fluttering intensity, telegraph signals being almost unreadable. They have an indefinite and varying direction of arrival, when the transmitting antenna is omni-directional; when the transmitting antenna is highly directional, they appear to come from some place along the beam remote from the transmitter.

[1] Figures in brackets indicate the literature references at the end of this paper.

Observations of back scatter using pulsed emissions from highly directive antennas indicated that weak irregular scatter echoes were arriving from the region where the beam penetrated the E layer, followed by stronger and more continuous scatter echoes with retardation times roughly equal to the equivalent path for single-hop F_2-layer transmission over a distance equal to the skip distance. Eckersley [3, 9] attributed both these effects to the same phenomenon, i. e., back scatter from ionic clouds in the E layer (see fig. 1) and called the first scatter group "short scatter" or "E scatter" and the second group "long scatter" or "F_2-E scattered". It was believed that, since the beam spreads with increasing distance, the more distant echoes appeared to have greater continuity than the simultaneously observed short-distance echoes only because more scattering sources are excited at any given time.

As a result of the work done by Eckersley and by K. W. Tremellen, a hypothesis of radio transmission known as the two-control-point theory was evolved by the latter. In this hypothesis it was assumed that the limiting condition for transmission over any path greater than one hop in length was for propagation to be possible at both ends of the path at angles of arrival and departure approaching grazing incidence, it being assumed that the long-scatter sources would assist

in carrying sufficient useful energy across the intervening distance.

Other observers, including Jansky and Edwards [4] and W. R. Piggott, observed echoes that appeared to come from the ground, and concluded, contrary to Eckersley, that the ground was a major source of scatter.

In order to obtain more information on the origin and mechanism of back scatter, the Central Radio Propagation Laboratory decided to undertake oblique-incidence pulse experiments. In addition, high-power directional pulse transmissions from the CRPL Sterling, Va. field station had been requested for other experiments conducted by the U. S. Navy Electronics Laboratory, San Diego, Calif., and by a Boston University group at Alamogordo, N. Mex. Both these groups furnished valuable data for the back-scatter studies.

2. Equipment

A self-excited pulsing transmitter, figure 2, using a pair of 527 triodes in push-pull, was constructed for operation on 13,660 kc with peak pulse inputs as high as 770 kw. The operating frequency was in the middle of a "scientific, medical, and industrial" band. The pulse repetition rate was 25 per second and the pulse length 40 microseconds. The transmitting antenna was a rhombic with a calculated major lobe at an angle of 14° with the horizontal, oriented 263° from true north, as shown in figure 3.

The receiver was a commercial model modified for pulse reception. The receiving antenna, in later experiments, was a sloping vee directed toward the west.

The indicator was a conventional loran-type indicator. An Air Forces 0–15 recording camera was used to record the pulses. In operation the initial transmitter pulse was located at a convenient position on the sweep and readings taken from it as a reference. The movable pedestal was used to locate pulses for detailed observation on "fast sweep."

II. Miscellaneous Experimental Observations

1. General

The transmitter was operated during all or a portion of a selected 24-hr period on a number of days during the months covered by this report. On all runs visual observations were made of the received back-scatter as it appeared on the screen of the indicator, and the delay times were noted. Photographs of the received pulse patterns were taken at intervals. Scalings of the observed phenomena or of these photographs were made for many of the runs and the results plotted against time. Figures 4 through 9 are plots of such observations for six periods from August 1947 through March 1948, illustrating the diurnal variation of the delay times and their association with skip distance. A detailed study of the trends and anomalies illustrated on these graphs appears in section III of this report.

In the interpretation of some of the data, delay times of pulse groups were noted and, assuming reasonable virtual heights of the ionosphere layers, plausible modes of propagation were inferred, considering the radiation pattern of the transmitting antenna. The lack of precise knowledge of the ionosphere was less of a drawback than it would at first appear since usually, if one mode was chosen as reasonable, the next best would appear unreasonable in the light of probable ionospheric heights and angles of departure.

The curves of figure 10, relating delay times, distances, and virtual height of the ionosphere were used to determine distances from the observed delay times and assumed virtual heights. These curves were calculated from the geometry of a propagation path, assuming the "equivalence theorem," i. e., assuming, for oblique-incidence propagation, specular reflection from virtual heights observed at vertical incidence.

Figure 11 shows families of curves of constant angle of departure, the most nearly vertical of the two families on the figure, which were calculated using the same geometrical assumptions as were used for the curves of figure 10. These curves were used for determining probable angles of departure for given delay times and assumed virtual heights. Incidentally, the transmission curves (for different distances) of figure 11, were originally derived at this Bureau during World War II for obtaining oblique-incidence maximum usable frequencies from recorded vertical-incidence ionospheric data.

2. Usual Types of Observations

In general the echoes received along the delay-time axis were not discrete pulses, but groups of

myriads of rapidly varying echoes peaking in intensity around one or more fairly well defined delay times. Each of these echoes faded in and out so rapidly that even a single camera exposure does not do justice to the picture. Besides, even the major peaks shifted in amplitude and delay. Figure 12 shows how a return group with a delay time from 8½ to about 16 msecs changed its configuration in as little as 45 sec, the six photographs having been made between the time of 0010+58″ and 0011+43″ GCT on November 21, 1947. Figure 13 shows such a back-scatter echo seen on August 27, 1947, with the fine-grain structure changes that occur in as little as 2 sec, made evident by displaying an echo group on the 2,500-microsecond sweep of the Loran indicator at 2-sec intervals.

Recording of pulses was beset with great difficulties caused by interference from stations on channels near or directly on the transmitter frequency. Figure 12, mentioned above, also shows the change of interference conditions in the 45-sec interval.

In addition to interference, reflections from airplanes and meteors were often noted. These were in the form of discrete pulses, to the extent of the resolution of the "slow sweep," in contrast to the scatter returns.

Often under night conditions over the path, pulse return groups corresponding to as many as four long hops were noted, assuming that the delay time is a measure of the skip distance to a scatter source. This would mean that back-scatter was being received at times from as far as the middle of the Pacific Ocean. It was often noted in the evening at Sterling that the delay between a second echo and a first echo was shorter than that between the transmitted pulse and the first echo. These observations may be explained by the fact that at these times the second hop was in daylight, as well as farther to the south, both conditions contributing to a shorter skip distance. Figure 14 for Feb. 16, 1948, at 0252 GCT shows three separate back-scatter groups. These echoes appear as plots in figure 8 at the appropriate time delay.

3. Direct F_2 Reflections

When the ordinary-wave critical frequency overhead is greater than the operating frequency, as occasionally happens during winter daylight hours, as shown in figure 6 at 1536 GCT, November 26, 1947, the ordinary-wave return shows a single intense clean pulse, in this case at 2.4-msec delay. Another weaker pulse at 3.4 msec corresponds to the extraordinary wave. The 2.4-msec delay corresponds to a virtual height of 370 km. It was actually noted that the virtual heights observed in this manner were of the order of 20 km higher than those noted simultaneously for the same frequency on the vertical-incidence ionosphere recorder operating in the same building. This seemed to indicate the fact that the highest lobe on the rhombic transmitting antenna, peaked at an angle less than 90°, caused the reflections to be observed from an angle slightly off the vertical. Two groups of pulses seen on the same sweep, beginning at 4.6 and 8.2 msec were examined for the delay times of 5.2 and 9.0 msec at about the center of each group. The 5.2-msec delay may correspond to scatter from the ground 475 km away propagated via the F_2 layer at a reasonable assumed virtual height of 300 km. The angle of departure for this would be 50°, corresponding to the middle of the second lobe of the rhombic antenna. The 9.0-msec delay may correspond to scatter from the ground 1,250 km away propagated via the F_2 layer at a virtual height of 220 km. The angle of departure for this would be 16°, near the peak of the lowest lobe. The virtual height of 220 km is reasonable for this case since at oblique incidence, with frequency constant, the virtual height decreases as the distance increases and approaches the minimum virtual height, which was of that order of magnitude in this case.

4. Persistent "Short Scatter"

An odd type of phenomenon, rather difficult to explain, was noted on the night of January 21–22, 1948, between 0500 and 0700 GCT. Very strong and persistent echoes were received at delays of the order of 2.6 msec along with longer-delayed echoes of much lower intensity as shown in figure 15, and in the plots of figure 7. From the delay time the only reasonable source of these echoes would be short scatter directly from the E layer at an angle of departure of 14°, right on the main lobe of the transmitting antenna, yet a more intermittent and weaker type of echo would have been expected for this case. The alternate solution would be ground scatter propagated via E layer from a source 310 km away, but not only did the

angle of departure for this case fall in an antenna null but, in addition, E-layer ionization would probably not have been great enough to sustain a reflection at 13,660 kc/s. It is possible that the intense short distance reflections, because they were seldom seen, were associated with the sporadic-E type of ionization.

5. Sudden Increase of Skip

It was observed that at times of "fadeouts" of the scatter echoes, when the skip suddenly increased, observable in several of the plots as in figure 8, at 0650 GCT, echo groups always become indistinguishable long before the delay time, about 27.1 msec, for the theoretical 4,000-km limit of one-hop F_2 was reached. It may be concluded that the echoes became weaker than the noise and interference at the longer distances because the angles of departure were far below the maximum of the first lobe of the transmitting antenna.

A point of interest is the great speed with which the observed echoes change their delay times before and after the "fadeouts" just mentioned. Figure 9 for March 14, 1948, between 0530 GCT and 0645 GCT illustrates the point. The first echo visible after the fadeout was at 0610 GCT, and the first pulse peak of the group came at 22.3 msec delay. The delay time decreased almost uniformly to 0645 GCT, when it became 15.5 msec. The rate at which the delay time decreased was then 11.7 msec/hr, making the energy peak appear to approach the receiver at a speed of 1,750 km/hr if the velocity of propagation were assumed to remain constant at 3×10^5 km per second.

6. Sunrise Effects

Effects around sunrise over the path are rather complex, and data are very scarce because of interference and also because of a number of equipment failures that occurred around this time.

Study of the films indicated that all of the returns between 0845 and 1015 GCT shown at a delay of less than 12 msec on figure 5 for October 2, 1947, were really distant multihop echoes seen the second time around on the 40-msec sweep, since they were all weaker than the large groups plotted in the region of 22 ms. However, later short-distance groups after 1100 were strong enough to be considered as reflections from close-in sources. It is to be noted that these groups appear during the period when groups just beyond are moving closer and that they subsequently disappear. Similar effects are seen in figure 4 for August 27, 1947. The close-in groups at 1042 and 1103 appear to be from a short distance, and the single group at 1130 is ambiguous in appearance but may be a distant group moving in.

One possible source of the close-in scatter noted in the above two cases is the regular E or the E_s layers as ionization increases greatly with sunrise. Such scatter, if weak, might disappear because of increased absorption later in the day. Another possible source of close-in echoes at sunrise would be specular reflections caused by a tilted layer or a combination of a tilted F_2 layer and the start of the E layer, forming a duct with an oblique top into which waves may go and be returned specularly. Reference [2] treats of this type of mechanism, which may be responsible for certain types of echoes and also gives a plausible explanation for the variation of the relative intensities of multiple echoes at near vertical incidence on the basis of specular reflections from irregularities in the ionosphere, which have a focusing and defocusing effect as they drift by.

Occasionally, visual observations of the indicator, around sunrise, showed that groups may be received corresponding to daytime skip, with long-distance echoes from the night-time regions seen simultaneously. This condition could prevail when the presunrise minimum of F_2-layer ionization was some distance to the west of Sterling.

III. Comparison of Results with Other Concurrent Observations: Sources of Scatter

1. General

Other concurrent observations with which test data were compared were:

a, Vertical-incidence ionosphere observations.
b, Arrival time of transponder pulses from Alamogordo, N. Mex.
c, Recordings of pulses from Sterling, Va., made by U. S. Navy Electronics Laboratory at San Diego, Calif. [11].

The variations of the delay times of CRPL back-scatter observations were compared with simultaneous vertical-incidence ionospheric observations at several stations in the United States.

Since only a very small percentage of the radiated energy is scattered backward from either the assumed ground or E-region scatter source, back scatter on 13,660 kc, even with the power and beaming used, is not easily detected except for scattering areas at approximately the skip distance from the transmitter. At or near the skip distance "high" and "low" waves traversing the ionosphere converge, forming a caustic, at which the transmitted energy is concentrated and, similarly, energy scattered at different angles of elevation from a scattering area is made to converge by the ionosphere, concentrating the reflected energy so that it is sufficient for detection [1, 7]. Consequently, if back scatter is from the ground, the delay time observed between the transmitted and back-scattered pulses should correspond roughly to the skip distance for that frequency at the point of reflection. If back scatter is from the E layer the delay time is less by the travel time along the oblique path between the E-layer scatter source and the ground scatter source in figure 1.

2. Skip-Distance Maps

In order to test these assumptions, F_2-layer skip-distance maps of the United States, for the frequency 13,660 kc were prepared from ionospheric data observed at Washington, White Sands, Baton Rouge, San Francisco, Boston, and Ottawa, for a number of hours during each day on which the pulse experiments were conducted. Such skip-distance contour maps were necessarily rather rough, since the observations at these six locations must be extrapolated to cover the entire country. The F_2-layer skip distance was derived by standard methods from the observed values of $f°F_2$ and F_2-3000-muf reported by the ionosphere stations, and the map construction involved longitudinal extrapolation. Figure 16 for August 27, 1947, at 1100 GCT is typical of the F_2-layer skip-distance maps. The values of the contours are the skip distances in kilometers, for 13,660 kc, for one-hop transmission reflected at points on the contours.

It was assumed that the transmitting antenna beam width was 30°, centered on the direction of orientation, and that, in this sector, back scatter is observable for a given path length wherever the midpoint of path coincides with the skip-distance contour for that distance. Assuming the velocity of propagation to be 300 km/msec, and arbitrarily adopting an ionospheric reflection height of 300 km, the expected range of time delay between transmitted and back-scattered signal over the sector was derived from the range of values of skip distance for which back scatter was expected. The ground-scatter delay-time values derived from the skip-distance maps are plotted on figures 4 through 8, for comparison with the observed back-scatter delay-time values, solid circles being used to designate the shortest and longest delay time expected. For the shortest delay time the corresponding delay times for E-layer long-scatter from an assumed 110-km height were obtained from figure 17 and plotted as open circles. Arrows pointed vertically upward indicate skip greater than 4,000 km.

Each of the figures were examined to decide from the relative positions of the plotted returns whether or not scatter was from the ground or the E layer. Echoes from the ground over a range of skip distances would give a line of pulses on the indicator time axis, and the same could be true for the E layer but with the returns displaced by a time difference of the order of that between curves B and C of figure 17; it is obvious that if both types were present ambiguity would exist where the two lines of pulses overlapped. However, if only one or a few closely grouped peaks of ground scatter exist in a given case an analogous group for E-layer back scatter may also exist separately at the distance determined roughly by figure 17.

3. Transponder Results

The strongest supporting evidence indicating that the observed returns may often be ground scatter is presented in figure 6 of the run of November 25 to 26, 1947. In that experiment a transponder operated by Boston University personnel at Alamogordo, N. Mex., was synchronized on the strongest pulse of a group received from Sterling. It is seen on the plot between 0430 and 0607 GCT. As the skip moved out in that period the transponder arrival time changed relatively little, because it was dependent only upon the virtual height of the ionosphere. At 0445 the transponder return is seen split, apparently because of Pedersen ray effects (actually at some intervals more than two echoes were visible because of extraordinary wave). At 0607 it is last seen at

a delay time of 18.9 msec (figs. 6 and 19). It is almost on top of the nearest back-scatter energy peak, so that it seems reasonable to conclude that that peak represented ground scatter from the equivalent distance for a single F_2 hop, since a reasonable F_2-layer virtual height would give approximately the same delay time. The transponder was turned off at that time because the pulses from Sterling were too weak for synchronizing. Since the transponder was adjusted manually to emit within less than 50 microseconds after reception of the Sterling pulse at Alamogordo, and since E-layer scatter would have appeared on the sweep about 4.6 msec earlier, the assumption that the back scatter in this case was from the ground seemed justified.

The predicted minimum skip distance for the assumed 30° sector as indicated by the lower solid black dot at 0600 in figure 6 falls right at the range at which the transponder was last seen. This, however, was not the skip distance for the exact azimuth of Alamogordo on the skip-distance map for that hour, the latter being greater than 4,000 km. Therefore, the agreement of the dots and the scatter and transponder ranges is not as good as it seems on first inspection. However, considering the limited number of points from which ionospheric data were obtained, these maps could easily be in error.

Good agreement was not obtained for the times of signal failure at Sterling and at Alamogordo. The transponder signal of only a few hundred watts peak power, was still fairly strong at Sterling, as shown by figure 6 when the Sterling pulses were reported as too weak for synchronizing at Alamogordo. This fact points to possibilities of difference of antenna patterns of both transmitter and receiver at both ends, nonreciprocity in the ionosphere, and lateral deviation, all of which should be investigated further. The antennas at Alamogordo were not sharply beamed, making it possible for transponder returns to travel over a devious route after direct path failure. However, the presence of more interference at Alamogordo than at Sterling could have caused the discrepancy. It still seems to be true, in spite of discrepancies, that the peaks of the returned pulse groups particularly the one corresponding to the transponder position in figure 19 are ground scatter because no peaks were seen at the delay time which would be required for E-scatter for this path, which would be of the order of 4 or 5 msec earlier than the transponder pulses.

Subsequent transponder experiments up to a year past the period covered by this paper demonstrated that the delay time of the first major peak of the back scatter begins to exceed the delay time of the transponder as the latter fails, and that the reverse is true as the signal returns with sunrise over the path. These results indicate that the main body of the back scatter is, for the case under consideration, ground scatter. If E-layer back scatter is present under these conditions, it must be much weaker and hidden under the interference.

4. E-Layer Scatter Preceding Ground Scatter

Generalizing from the transponder results, it was assumed that returns showing only a few closely spaced pulse peaks were probably of the ground-scatter type. Similar groups with single peaks or small groups of pulse peaks falling the right amount earlier, as determined from figure 17, were judged to be ground scatter with E-region scatter ahead of them. This assumption was supported by the fact that occasionally very strong discrete pulses of a few seconds duration, which appeared to be reflections from meteor trails, came from about the expected E-scatter region. These echoes seem to appear usually when there is no persistent scatter peak at the point in question, suggesting that possibly the back scatter from the E-region is not always present. Sometimes, however, they appear in other places, suggesting the desirability of an investigation of the possible overlap of delay times of E and ground-scatter returns because of finite beam width.

The type of echo pattern in which such earlier separated echo groups appear is noted in figure 5, for October 2, 1947, an ionospherically disturbed day, between 0845 and 1015, the separate returns falling at between 16- and 20-msec delay. It will be noted that most of these fall about 4 msec ahead of the first energy peak in the succeeding groups. The independently calculated F_2 return points (solid circles), and corresponding E points (open circles) fall a few milliseconds earlier, but the agreement is fairly good.

The earlier separated echo groups, assumed to be E scatter, were quite variable in amplitude with a tendency to disappear altogether, leaving a line of low-intensity echoes extending along the time axis to the major peaks. Figure 18 illustrates this

fact when viewed in conjunction with the plotted returns in figure 5 for the period 0845 to 1015. The points concerned are on the upper trace in each frame of figure 18. The initial pulse is on the lower pedestal, and the little echo on the lower trace is probably 2-hop F_2. On the upper trace is seen a strong return preceded by a weaker echo that disappears into a line of very weak return pulses after a few seconds. Several echo groups at other hours on figure 5 seem to exhibit similar characteristics, notably those at 0545 and 0807.

Weak fleeting pulses at about the E-layer distance ahead of second multiple F_2 were sometimes noted on winter days when the ionosphere could sustain vertical-incidence F_2 reflections, suggesting the weak echoes shown by Eckersley in figure 21 of reference [3].

5. Agreement of San Diego Reception Results

Referring again to the October 2 observations, at 0530 on this day the Sterling emissions under observation at San Diego failed for several minutes. Reception then recovered and failed again at 0548, being intermittent to 0558. During this period, figure 5 shows a pulse peak in the neighborhood of 25.0 msec, which is the delay time for the 3,650-km path for ground scatter propagated via the F_2 layer at a height of 300 km. At 0545 there appears to be an F_2 echo after an E-echo group. At 0530 there is a first strong peak with echoes coming in for about 5 msec preceding. At this time the return is shown as one group, but the peaks at 22.3 and 22.9 msec could be associated with E-layer back scatter by comparison with the 0545 return. In fact the pictures taken in this period resemble those of figure 18, and the peaks at 22.3 and 22.9 msec are weak compared to the return at 25.0 msec. The calculated skip-distance chart for 0600 for the azimuth of San Diego was in exact agreement with the results at San Diego. This chart was one with regular contour lines, which seem to be more accurate than those for an irregular distribution of ionization where interpolation is difficult.

6. E-Layer Scatter Exclusive of Ground Scatter

A case that appears to exhibit E-layer scatter exclusive of ground scatter is that for January 21 to 22, between about 0400 and 0830, as seen on figure 7. In section II it was noted that the close-in returns appeared to be short scatter. The returns around 15 msec fall near the expected E-layer long-scatter delays. It is to be noted that the calculated F_2 skip for that period as shown by the position of the solid dots on figure 7 was long. This was corroborated by the record of reception of the Sterling pulses at San Diego, which reported reception weak between 0630 and 0730 and out completely between 0730 and 0946 with a "fade" commencing again at 1002. At the long distance, the E-scatter region is considerably closer than the ground-scatter region, and it would appear that the energy going to and from the ground is attenuated greatly by passing twice through the D and E layers so that one may conclude that the echoes seen at about 15 msec between 0400 and 0830 are solely E-layer returns. The assumption agrees with the observed loss of long distance returns as the F_2 skip moved out, as noted under section II, 5. There was a fair amount of sporadic-E ioni ation observed at Washington and some at Alamogordo during this period.

Echoes of the type discussed above are seen in figure 15, beginning at 2.4 msec for the E-layer short-scatter case and beginning at 13.0 msec for the E-layer long-scatter case.

7. Additional Considerations

It appears that often the strongest peaks may be due to back scatter from the ground, but that a continuous group of weak echoes preceding it in time may come from the E layer. The whole problem of just what the individual peaks are due to may be ambiguous in almost all cases where no concurrent supporting data are available, and in many cases where such data are obtainable. Among the many things that may cause these peaks are E-layer back scatter and scatter from ordinary ground, as well as from the sea and from large irregularities in the terrain. For a single hop in one direction, the low ray, ordinary wave, will always appear. There is also the possibility of ordinary-wave high ray (Pedersen ray), and low and high wave extraordinary. All four modes for one hop could conceivably, in the limiting case, become 4^{2^n} modes for n hops of back scatter, although in practice conditions would never arise whereby all control points would propagate all modes. Besides, echoes returned by more than one hop become weaker as the number of reflec-

tions increases, so that many modes probably would not be visible.

Another source of ambiguity is the antenna radiation pattern. The transmitter beam width is only approximately allowed for in the analysis and minor lobes may cause reception of scattered energy from other sectors.

IV. Conclusions

As a result of the study of back-scatter echoes from a high-power pulse transmitter on a westward path from Sterling, Va., on a frequency of 13,660 kc between August 1947 and March 1948, certain conclusions were reached for the case studied.

Echo groups may often be seen containing peaks of energy scattered from the ground, which are stronger than peaks due to other sources. Echoes also appear, however, which are identifiable with E-layer long scatter. These are sometimes seen as weak, intermittent pips ahead of what appear to be ground-scatter pips and sometimes as a continuous line of weak pulses ahead of the main ground-scatter pulse. On occasions of long-distance F_2 skip, E-layer long scatter may appear without ground scatter being visible above the interference.

What is usually termed E-layer short scatter can be said with some certainty to be echoes from meteor trails. However, on rare occasions very strong clean and steady echoes have appeared at night at a distance which would indicate that they were direct reflections from intense clouds of sporadic E.

At sunrise, peculiar conditions arise that may in part be explained by the presence of long- and short-distance echoes when the pre-sunrise minimum of F_2-layer ionization is over the path and in part by back-scatter from the regular E or the E_2 layer before ionospheric absorption becomes large. Another possibility is a specular type of reflection from tilted layers.

Many ambiguous echoes are to be seen whose interpretation will require further study and experiment, considering ionospheric phenomena and antenna patterns.

The authors are indebted to G. F. Montgomery, who was responsible for the calculations of the rhombic antenna radiation pattern and the chart of sky-wave transmission delays. They are also grateful to W. Cullen Moore, of Boston University, through whose efforts the original transponder emissions were made from Alamogordo and to H. P. Gates of the U. S. Navy Electronics Laboratory, who furnished reception data from San Diego.

V. References

[1] T. L. Eckersley, Studies in radio transmission, J. Inst. Elec. Engrs. **71,** 434 to 443 (1932).

[2] J. A. Pierce and H. R. Mimno, Reception of radio echoes from distant ionospheric irregularities, Phys. Rev. **57,** 95 to 105 (Jan. 1940).

[3] T. L. Eckersley, Analysis of the effect of scattering in radio transmission, J. Inst. Elec. Engrs. **86,** 548, discussion, p. 563 (1940).

[4] C. F. Edwards and Karl G. Jansky, Measurements of the delay and direction of arrival of echoes from nearby shortwave transmitters, Proc. IRE **29,** 322 (June 1941).

[5] An automatic instantaneous indicator of skip distances and muf, Report IRPL-R9, Interservice Radio Propagation Laboratory, National Bureau of Standards (Washington, D. C., Feb. 1945).

[6] T. L. Eckersley and F. T. Farmer Short-period fluctuations in characteristics of wireless echoes from the ionosphere, Proc. Roy. Soc. [A], **184,** 196 (Aug. 21, 1945).

[7] Sir E. Appleton and W. J. G. Beynon, The application of ionospheric data to radio communication problems, Part II, Proc. Phys. Soc. **59,** 58 (1947).

[8] Instructions for use of basic radio propagation predictions, NBS Circular C465 (1947).

[9] T. L. Eckersley, Observations of scatter clouds, Nature **162,** 24 to 25 (July 3, 1948).

[10] Arthur H. Benner, Predicting maximum usable frequency from long-distance scatter, Proc. IRE **37,** 44 (Jan. 1949).

[11] H. P. Gates, Observations of long-distance pulse propagation, interim report (Aug. 1947 to July 1948), U. S. Navy Electronics Laboratory Report No. 116 (April 5, 1949).

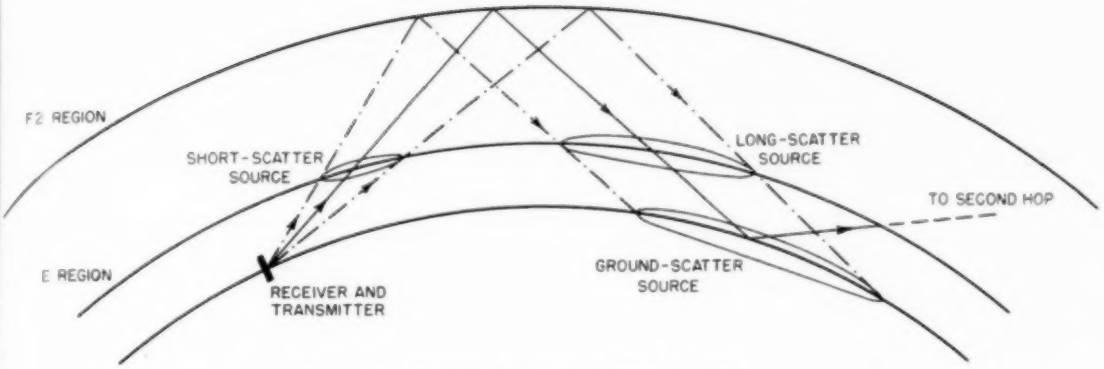

FIGURE 1. *Probable sources of scatter phenomena.*

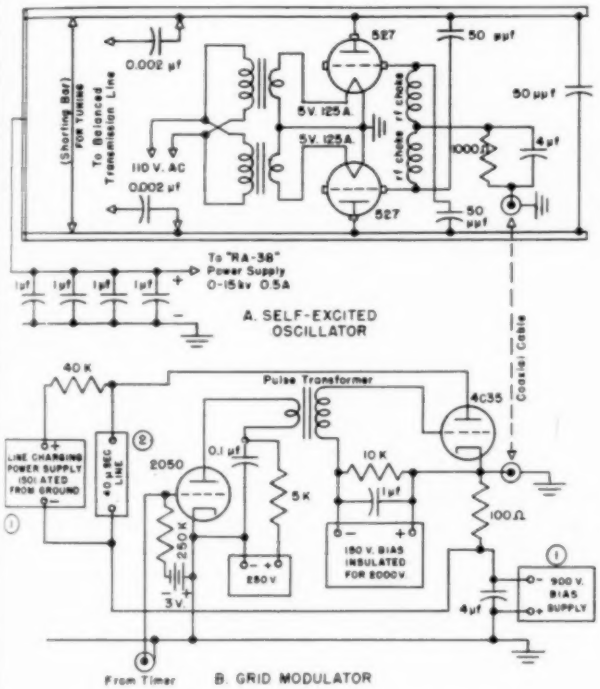

FIGURE 2. *High-power pulse transmitter used for back-scatter experiments.*

Bias-supply and line charging-supply voltages are varied for proper operating conditions. Line has 100-ohm characteristic impedance. A, Self-excited oscillator; B, grid modulator.

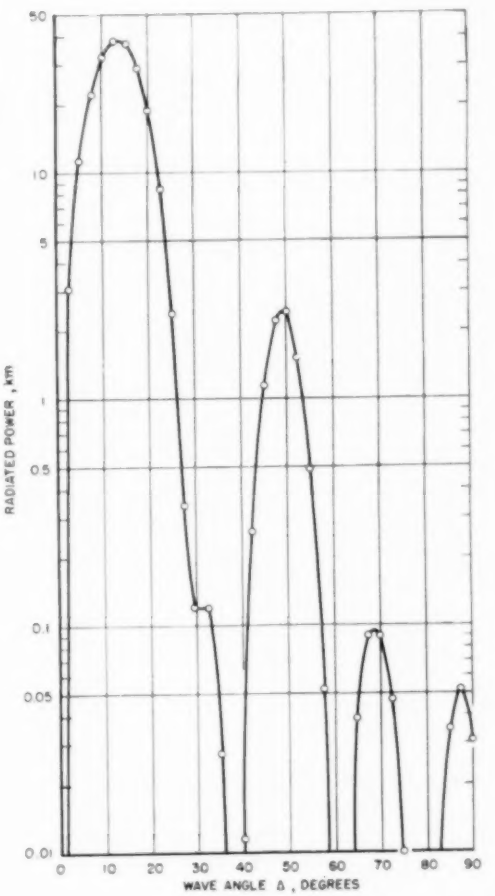

FIGURE 3. *Calculated vertical radiation pattern of rhombic antenna used in back-scatter experiments at zero azimuth.*

Data assumed in calculations: leg length, 262.5 ft; height, 75 ft; angle of tilt, 57°; frequency, 13.66 Mc/s. Ground constants: $\epsilon=10$; $\sigma=2\times10^{-14}$ emu. Radiated power at a particular wave angle is the power input to a lossless short vertical antenna over perfect ground, which will produce a zero elevation field intensity equal to the field intensity at the given angle produced by 1-kw input to the rhombic. The field intensity produced by 1-kw input to this reference vertical antenna is 186.3 millivolts/meter at 1 mile.

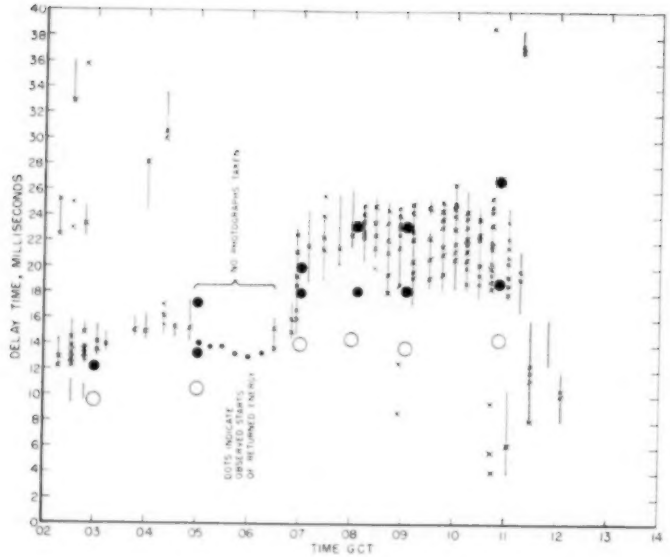

FIGURE 4. *Back-scatter observations on 13,660 kc at Sterling, Va.; 0200 GCT August 27, 1947 to 1200 GCT August 27, 1947.*

Crosses indicate amplitude peaks. Solid circles indicate shortest and longest of ground-scatter delay times derived at any time from F^2 skip-distance maps. Open circles indicate E-layer long scatter corresponding to shortest derived ground scatter delay time.

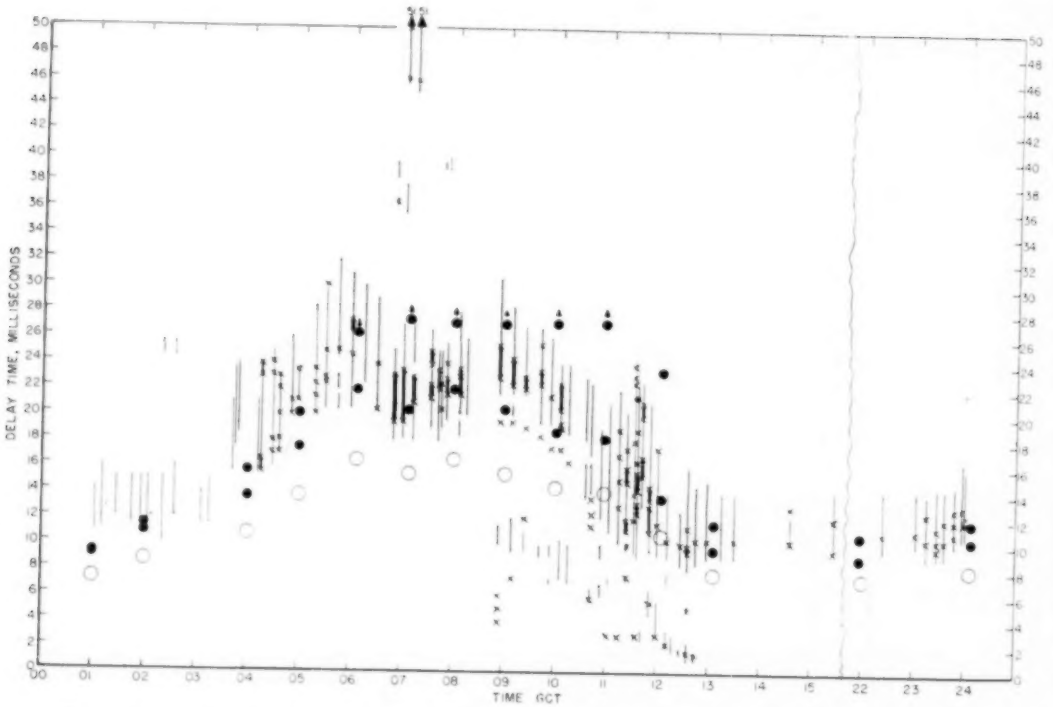

FIGURE 5. *Back-scatter observations on 13,660 kc at Sterling, Va.; 0100 to 2400 GCT, October 2, 1947.*

Crosses indicate amplitude peaks. Heavy line between crosses indicates high amplitude between peaks. Solid circles indicate shortest and longest of ground-scatter delay times derived at any time from F^2 skip-distance maps. Arrows pointed vertically upward indicate skip greater than 4,000 km. Open circles indicate E-layer long scatter corresponding to shortest derived ground-scatter delay time.

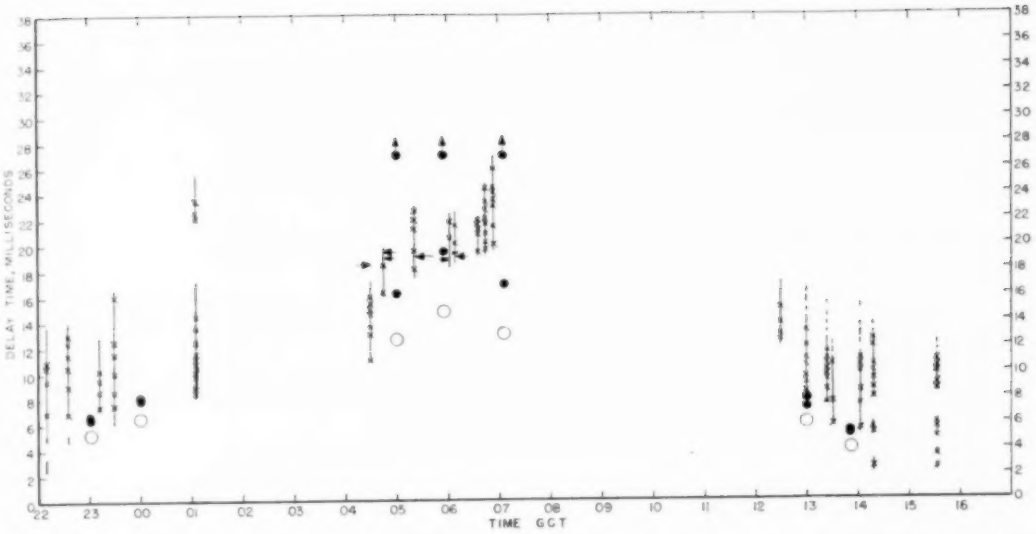

FIGURE 6. *Back-scatter observations on 13,660 kc at Sterling, Va., including reception of transponder located at Alamogordo, N. Mex.; 2200 GCT November 25, 1947 to 1500 GCT November 26, 1947.*

Crosses indicate amplitude peaks. Horizontal arrows indicate Alamogordo transponder returns. Solid circles indicate shortest and longest of ground-scatter delay times derived at any time from F^2 skip-distance maps. Arrows pointed vertically upward indicate skip greater than 4,000 km. Open circles indicate *E*-layer long scatter corresponding to shortest derived ground-scatter delay time.

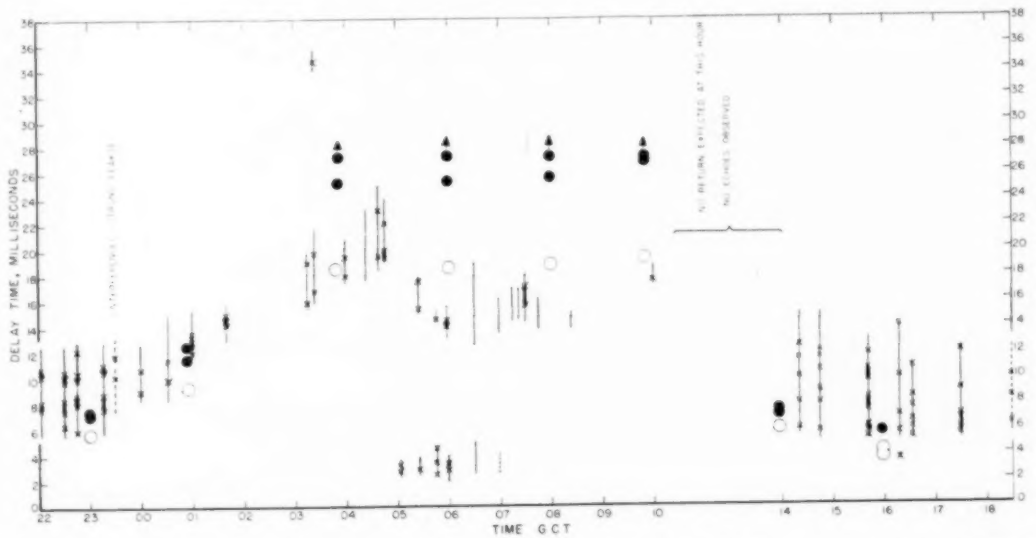

FIGURE 7. *Back-scatter observations on 13,660 kc at Sterling, Va.; 2200 GCT January 21, 1948 to 1830 GCT January 22, 1948.*

Crosses indicate amplitude peaks. Heavy line between crosses indicate high amplitude between peaks. Solid circles indicate shortest and longest of ground-scatter delay times derived at any time from F^2 skip-distance maps. Arrows pointed vertically upward indicate skip greater than 4,000 km. Open circles indicate *E*-layer long scatter corresponding to shortest derived ground scatter delay time.

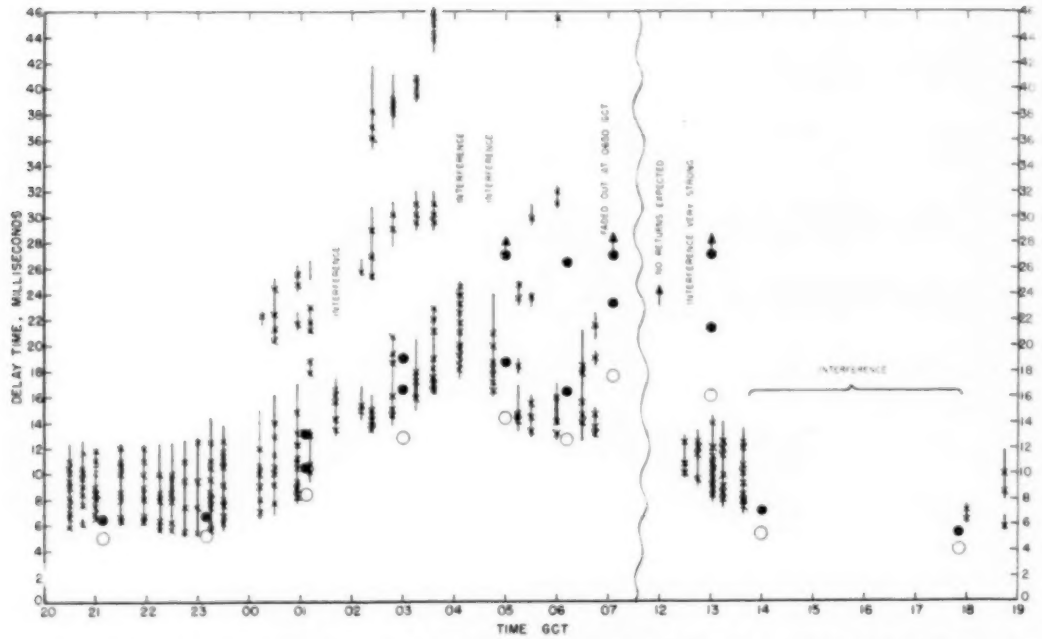

FIGURE 8. *Back-scatter observations on 13,660 kc at Sterling, Va.; 2000 GCT February 15, 1948 to 1900 GCT February 16, 1948.*

Crosses indicate amplitude peaks. Solid circles indicate shortest and longest of ground-scatter delay times derived at any time from F^2 skip-distance maps. Arrows pointed vertically upward indicate skip greater than 4,000 km. Open circles indicate E-layer long scatter corresponding to shortest derived ground scatter delay time.

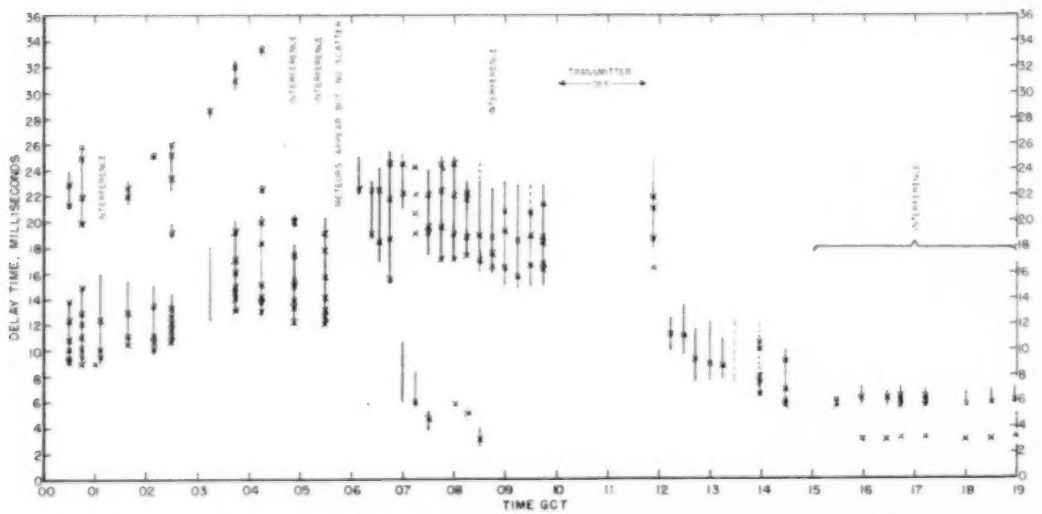

FIGURE 9. *Back-scatter observations on 13,660 kc at Sterling, Va.; 0000 GCT March 14, 1948 to 1900 GCT March 14, 1948.*

Crosses indicate amplitude peaks.

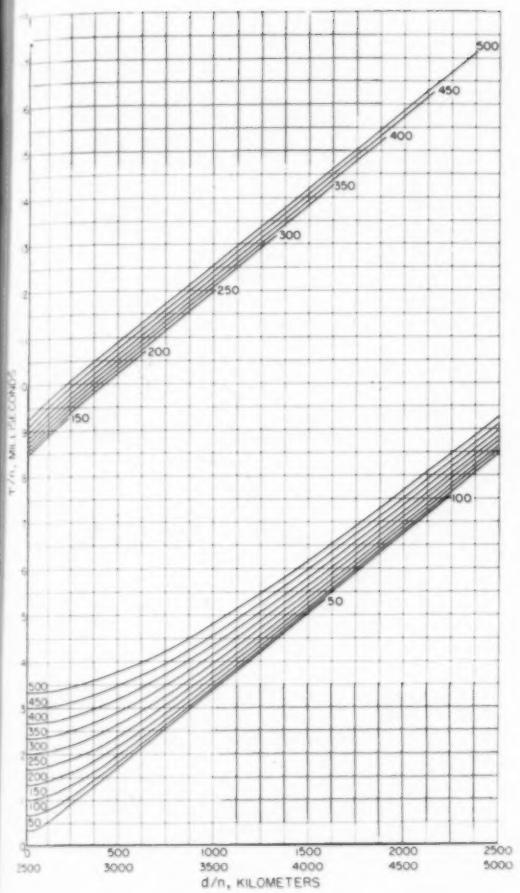

FIGURE 10. *Sky-wave transmission delays (geometrically calculated).*

t is the total sky-wave delay; d is the total great circle range, n is the number of hops. Values on curves denote virtual heights in kilometers. Curves terminate at maximum range, zero wave angle. Assumed earth radius is 6370 km.

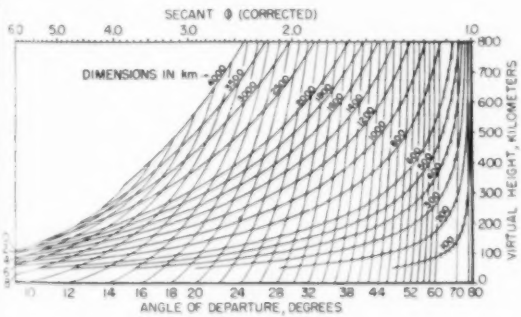

FIGURE 11. *Transmission curves showing vertical angles.*

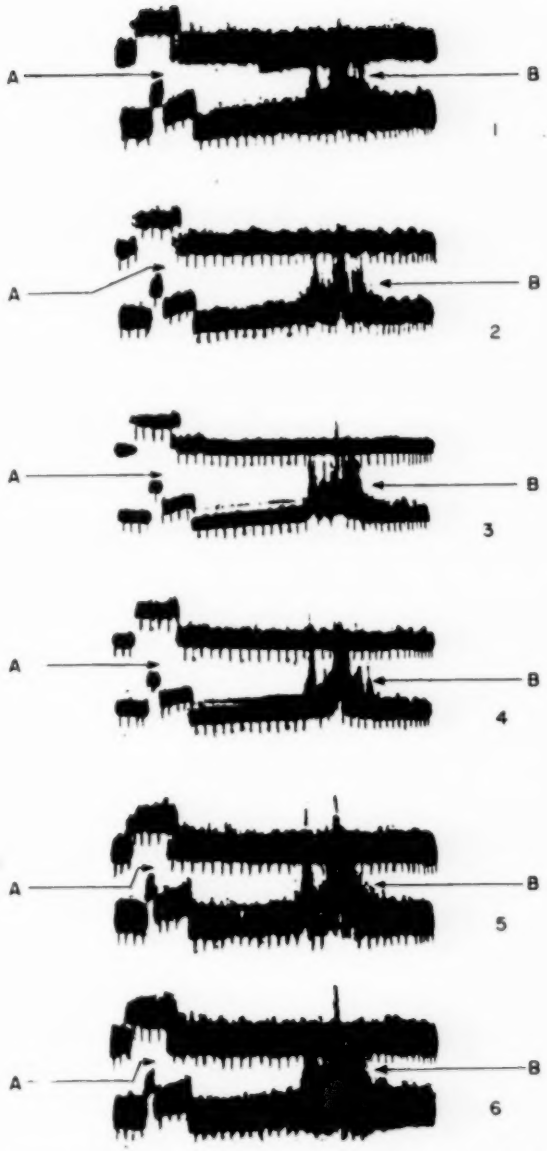

FIGURE 12. *Back-scatter echoes November 21, 1947 at 0010 GCT showing changes over a 45-sec interval.*

Initial pulse starts on pedestal on lower left. Time proceeds to extreme right, then to upper left and across to right, then down to lower left, total sweep being 40 msec. Each marker represents ½ msec, and every fifth marker is shorter than the rest. Frames 1 through 6 in time sequence. A, Transmitter pulse; B, first echo group.

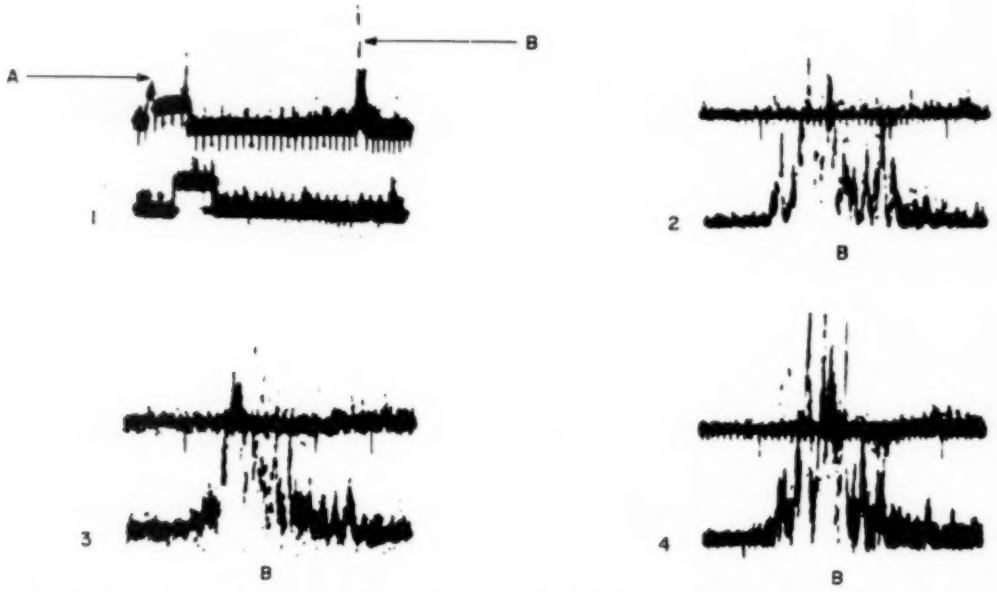

FIGURE 13. *Back-scatter echoes August 27, 1947. 1, slow sweep taken at 0314 GCT; frames 2, 3, and 4 taken a few minutes earlier at intervals of 2 sec on 2,500-μsec sweep.*

A, Transmitter pulse; B, first echo group.

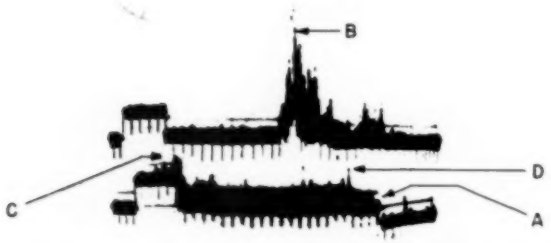

FIGURE 14. *Back-scatter echoes February 16, 1948, 0252 GCT, demonstrating presence of at least three echo groups.*

Initial pulse starts at lower right at break in base line. Time proceeds to extreme right, then to upper left and across to right, then down to lower left. First group is large double group on upper trace, second is partially on top of lower pedestal, third is just ahead of initial pulse. Pip to right of main pulse is probably a meteor. A, Transmitter pulse; B, first echo group; C, second echo group; D, third echo group.

FIGURE 15. *Returns on January 22, 1948, at 0617 GCT showing close-in strong reflections beginning at 2.4 msec in addition to weaker long-distance reflections beginning at 13.0 msec.*

A, Transmitter pulse; B, close-in strong reflections; C, long-distance reflections.

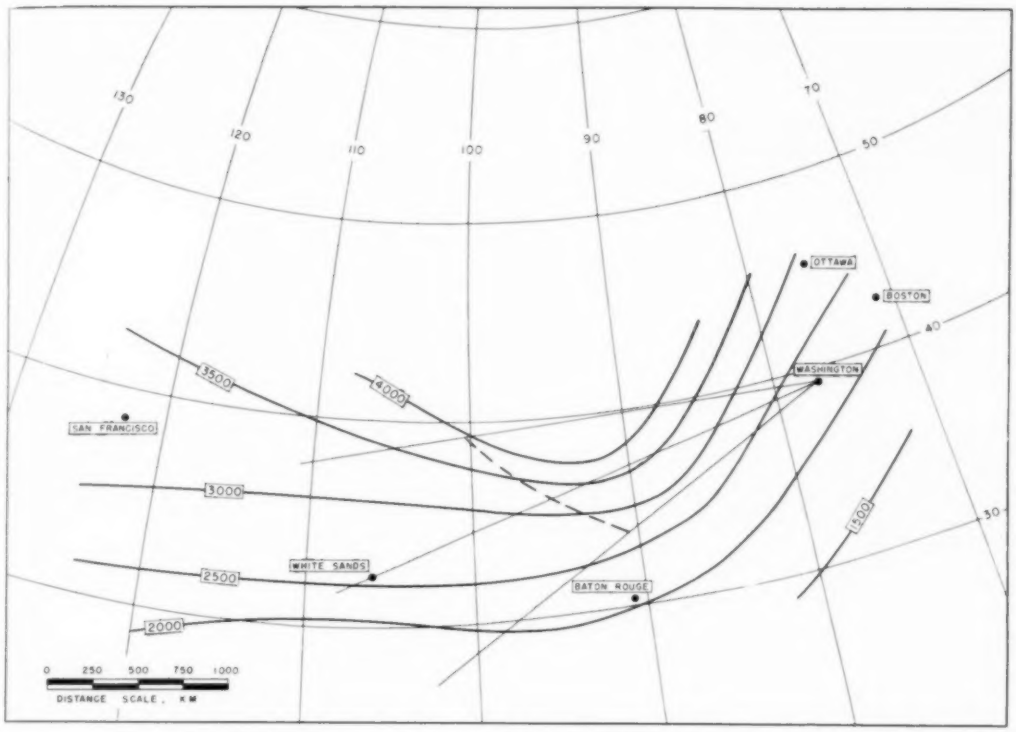

FIGURE 16. *Skip-distance contour map for 13,660 kc, 1100 GCT August 27, 1947.*

– – – –, Expected control points for back-scatter propagation via *F*2 layer.

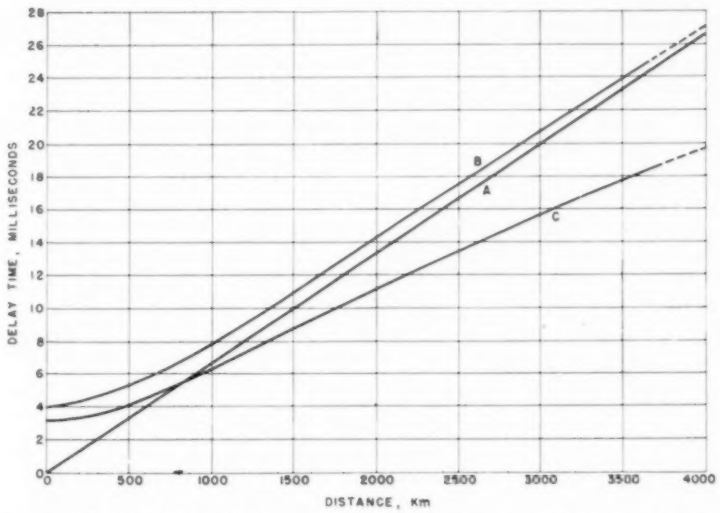

FIGURE 17. *Calculated echo delays assuming ground scatter and E-layer back scatter.*

A, Echo delay time, assuming ground-scatter and propagation along the earth's surface; B, echo delay time, assuming ground-scatter and 300-km virtual height of reflection; C, echo delay time, assuming back-scatter from *E* layer at 110-km virtual height and 300-km virtual height of reflection.

FIGURE 18. *Echoes on October 2, 1947 apparently showing E-layer back scatter ahead of ground scatter.*

Pulse and time sequence as in figure 4. Echoes under discussion are on upper trace. Small pip to right of lower trace is 2-hop. 1, "*E*-layer long scatter" ahead of assumed first-hop ground scatter at 0855+35 sec GCT. 2, "*E*-layer long scatter" weak, ahead of assumed first-hop ground scatter at 0923+17 sec GCT. 3, "*E*-layer long scatter" almost disappearing 2 sec later. A, Transmitter pulse.

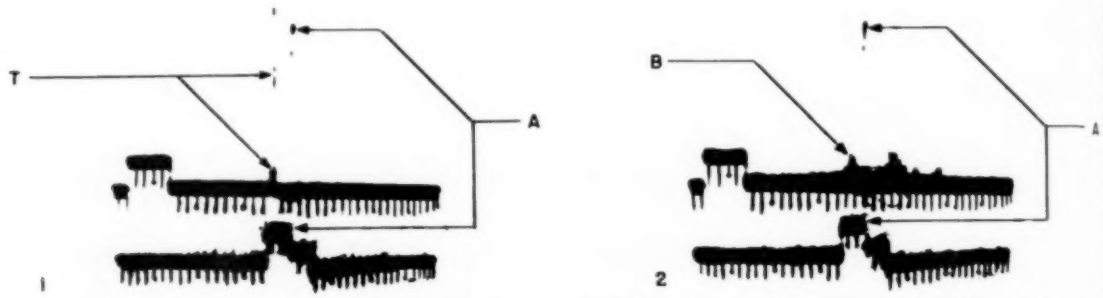

FIGURE 19. *Relative positions of transponder and back scatter when Sterling, Va., signal failed at Alamogordo.*

Initial pulse starts in middle of lower pedestal. Time proceeds as in figure 4. Point where initial pulse crosses top trace is approximately 20 msec. 1, Position of transponder last time definitely seen 0607 GCT (back scatter detuned). 2, Position of scatter group as seen 2 min later. A, transmitter pulse. B, first echo group; T, transponder.

WASHINGTON, July 25, 1949.